Norges miljø- og biovitenskapelige universitet

Master's Thesis 2019 30 ECT
Faculty of Science and Technology

Performance Analysis and Heat Transfer Modelling of a Floating Photovoltaic System

Philip De Paoli
MSc. Industrial Economics and Technology Management
Faculaty of Science and Technology

Preface

This thesis was a part of a project for Ocean Sun, by the Institute for Energy Technology (IFE). It was carried out to investigate the effect of Ocean Sun's technology on the performance of solar modules.

The people at IFE provided me with great support throughout this semester so I could complete my master's degree. I specifically want to thank Josefine Helene Selj, my supervisor at IFE, for academic feedback and Ida Hugem Lereng for everything regarding the project and for valuable feedback on my master. You have been a great resource throughout the semester. I must also thank Dag Lindholm for his time and help regarding the heat transfer part. Additionally, I would like to thank my supervisor at NMBU, Espen Olsen, for introducing me to IFE and providing me with information throughout the semester.

From Ocean Sun has Sigmund Bragstad helped me a lot in the logistics of traveling to Skaftå, setting up the sensors, lifting the modules and providing me with information about the system. I thank you for that.

Furthermore, I would like to thank my friends and classmates, whom I've had the pleasure of sparring with throughout the semester. Our discussions have been valuable and of great motivation.

Lastly, I must thank my mother and my father for constant support throughout these five years. Your advice, guidance and voice of reason has been and will continue to be an invaluable part in my life.

Philip De Paoli

Oslo, 13.05.2019

Abstract

As a result of an increase in demand for electricity and requirements for renewable resources, solar cells have emerged as a major contributor to worldwide electricity generation. The production of solar cells on a utility-scale basis require large areas with even terrain. The performance of solar cells is also largely dependent on cell temperature. Consequently, to meet the requirements of large areas while at the same time keep the cell temperature down, floating photovoltaic systems has emerged as a promising technology.

The main purpose of this study is to examine the performance of a floating photovoltaic (FPV) system by Ocean Sun and analyze the difference in performance between two strings. One of the strings is in thermal contact with a canvas that is placed on top of the water, and the other string is lifted 32 mm above the membrane using 32 mm PP-pipes. Additionally, the thesis will test fluid-dynamic models for modulating cell temperature in floating PV and compare the floating PV-system to hypothetical tilted strings in the same location.

The system is first analyzed with data from 01.06.2018 to 31.12.2018. The strings are then analyzed with data in the period from 14.03.2019 to 18.04.2019. In this period, the string in thermal contact with the canvas will perform 5.24% better than the string with a 32 mm air gap between the canvas and the modules. The relative difference between the strings seems to increase with increasing radiation, and extrapolated results indicate a difference of 6.66% at 1000 W/m^2. The back-surface module temperature is also evaluated, and a mean difference of just above 12 $°C$ is found for solar irradiance levels in the range of 600 to 750 W/m^2.

The results from the module and cell temperature modulation indicate that the steady-state models with a time-dependent boundary condition are too simple to simulate the cell temperature accurately. Regression models were also tested and found to perform somewhat better but performs poorly when it is used outside the intervals on which it is trained.

When considering a floating PV system against a tilted system, it is found that a tilted system at higher angles (50 – 60 degrees) will match the floating PV at low irradiance. At irradiance from 650 W/m^2, only systems with tilts at $50°$and $60°$ will match the production from the floating PV system. However, this demands that the systems operate at efficiencies close to 16%.

Sammendrag

Med et økende behov for elektrisitet på verdensbasis og høyere krav til kilder for elektrisitet, har solceller vokst frem som en viktig bidragsyter til å dekke verdens behov. For å produsere elektrisitet av solceller på stor-skala basis, kreves store områder og ofte ulent terreng. Solcellers ytelse er også i stor grad styrt av temperaturen i solcellen. Som et svar på det økende behovet for store land-areal og med muligheter for lavere celletemperaturer har flytende sol vokst frem som en lovende teknologi.

Hovedformålet med denne oppgaven er å undersøke ytelsen til et flytende solcelleanlegg av Ocean Sun og analysere forskjellen i ytelse mellom en streng som er i termisk kontakt med en membran som ligger på vannet og en streng som er løftet opp fra membranen med polypropylen rør med 32 mm i diameter. Oppgaven vil i tillegg undersøke muligheter for å modellere celletemperaturen i flytende sol med enkle fluid-dynamiske modeller og sammenligner det flytende anlegget med hypotetiske tiltede anlegg.

Strengene analyseres med data fra perioden 14.03.2019 – 18.04.2019. I denne perioden vil den strengen som er i kontakt med membranen yte 5.24% bedre enn strengen som har 322 mm luft gap mellom modulene og membranen. Den relative forskjellen mellom strengene virker å øke med økende innstråling, og ekstrapolerte resultater indikerer en differanse på 6.66% ved $1000 W/m^2$. Det observeres også en bakside-modultemperature differanse mellom strengene på rett over 12 grader ved innstråling mellom 600 og 750 W/m^2.

Resultater fra celletemperatur modelleringer indikerer at enkle steady-state modeller med tidsavhengig randbetingelse ikke vil klare å modellere celle eller modultemperaturen stabilt med høy presisjon. Regresjonsmodeller blir testet som alternativ, og gjør det noe bedre. Regresjonsmodellen lider derimot av lav generaliserbarhet.

Ved vurdering av flytende horisontalt system mot tiltet system viser resultatene at ved høy tilt (50-60 grader) vil de tiltede systemene produsere like mye, med krav om virkningsgrader opp mot 16%. Dette kravet virker å øke for høyere innstråling.

Nomenclature

Symbols

A	Surface area	m^2
A_m	The azimuth angle of the sun	°
$A_{m_{array}}$	The azimuth angle of modules	°
C_p	Specific heat capacity	$J/(g℃)$
e	Emissivity	-
E	Energy	W
F	Fuel expenditures	$
f	Frequency	Hz
G	Irradiance	W/m^2
h	Convection coefficient	$W/(m^2K)$
I	Current	A
k	Thermal conductivity	$W/(mK)$
L_c	Critical length	m
n_1, n_2	Diode ideality factor	-
P	Power	W
Q	Heat	W
Q_1	Median, the lower half	-
Q_3	Median, the upper half	-
r	Discount rate	-
R	Resistance (electric and thermal)	Ω or K/W
R_1	Regression score string 1	-
R_2	Regression score string 2	-
T	Temperature	℃
T_{cell}	Cell temperature	℃
v	Velocity	m/s
V	Voltage	V
$\boldsymbol{y}$	Observation vector	-
X	Design/feature vector	-

Δx	Thickness of layer	m
α	Solar altitude angle	°
β	Volumetric thermal expansion	$1/K$
$\boldsymbol{\beta}$	Parameter vector	-
ϵ	Residual vector	-
η	Efficiency	-
θ	Module tilt angle	°
θ_z	Zenith angle	°
λ	Penalty term	-
μ	Dynamic viscosity	$kg/(m \times s)$
ν	Kinematic viscosity	m^2/s
∞	Ambient state	-

Abbreviations

AC	Alternating current
AM	Air mass
DC	Direct current
DF	Diffuse fraction
Gr	Grashof's number
IN	Investment expenditure
Nu	Nusselt number
OM	Operation and maintenance
Pr	Prandtl's number
PR	Performance ratio
PV	Photovoltaic
Ra	Rayleigh's number
Re	Reynold's number
Ri	Richardson's number
AOI	Angle of incidence
DHI	Diffuse horizontal irradiance
DNI	Direct normal irradiance

FPV	Floating photovoltaic
GHI	Global horizontal irradiance
MAE	Mean absolute error
MPP	Maximum power point
POA	Plane of array
STC	Standard test conditions
MPPT	Maximum power point tracking
LCOE	Levelized cost of energy

Superscript

t	Time-variable
$diff$	Diffuse component
$direct$	Direct component
$ground$	Ground component

Subscripts

D	Diffuse
g	Band Gap
L	Light generated
m	module
P	Shunt
s	Surface
S	Series
t	Time variable
ac	Alternating current
dc	Direct current
OC	Open circuit
SC	Short circuit current
in	Input
cb	Conduction band
vb	Valence band
ph	photon

air	Property belonging to the air
max	Maximum power
rad	Radiation
ref	Reference value
sky	Properties belonging to the sky
STC	Standard test conditions
$back$	Back part of the module
$cell$	Solar cell
$cond$	Conduction
$conv$	Convection
$front$	The front side of the module
$water$	Property belonging to the water
T_{ref}	Reference temperature
$i \rightarrow j$	Surface i to surface j
01	Saturation diode 1
02	Saturation diode 2

Constants

g	Gravitational constant	$9.80665\ m/s^2$
h	Planck's constant	$6.626\ 069\ \times 10^{-34}\ Js$
k_B	Boltzmann's constant	$1.380\ 649\ \times 10^{-23}\ J/K$
q	Elementary charge	$1.602\ \times 10^{-19}\ C$
σ	Stefan-Boltzmann constant	$5.670\ 367(13) \times 10^{-8}$ $W/(m^2K^4)$

Contents

1 Introduction

1.1 Background/Motivation

Global electricity demands increased by 4 percent in 2018. Renewables and nuclear power contributed to most of the growth in demand, but coal- and gas power plants increased so that CO2 emissions rose by 2.5 percent from the sector [2]. With an increase in global demand for electricity, the global electricity generation must increase to meet the demands. However, national and international climate goals add guidelines to how this increase should happen.

There has been a substantial growth in the contribution of photovoltaic systems to meet global demands for energy consumption. Solar PV has experienced a large increase in installed capacity, and the Renewable Energy Policy Network reports that it was added more capacity from solar PV than from any other type of power generating technology in 2017 [3].

The most common use of solar energy is through photovoltaic (PV) systems. The development of PV-systems has primarily been focused around land-based systems that are mounted either on the ground or rooftops. For a large-scale plant, this will require a vast area with multiple land requirements. A large-scale PV plant of capacity in the range of 1 – 20 MW could need around 0.00166 m^2/kwh/year [4]. It can be challenging to meet these requirements in many regions where there is large potential for solar power. However, these requirements are often met on large water bodies, either in-land, near or off-shore.

When placing PV-systems on the water, water-bodies can be exploited in several ways. Floating PV can make electricity more available by allowing densely populated areas near shore and island communities, access to energy. Floating PV will also generate more electricity than ground-mount and rooftop systems, under the same conditions, because of the cooling effect of water [5].

1.2 Objective

The main objective of this thesis is to study the performance of a specific floating PV technology developed by Ocean Sun. A study of the performance of the entire system, as well as a study on the differences between strings which operate under different conditions, is done. The thesis also investigates simple fluid-dynamic solutions to model the cell

temperature and a regression model for cell temperature modulating and feature evaluation. The floating PV system is also compared to a mock system which has been tilted. This is done to analyze whether a tilt could outperform the effect of thermal cooling from water.

The thesis will do the following:

- ✓ Analysis of Ocean Sun's system at Skaftå
- ✓ Analyze the differences in the strings when one of the strings is air-cooled, and the other is water-cooled.
- ✓ Evaluate different fluid-dynamic models for cell temperature modulating
- ✓ Evaluate a regression-based model on predicting module temperature
- ✓ Compare Ocean Sun's floating PV-technology with tilted modules

2 Theory

Most of the theory is derived from the books *Solar Energy: The physics and engineering of photovoltaic conversion, technologies and system.* 1 ed. 2016 by Arno Smets, Isabella K.J. Olindo, Rene Van Swaaij and Miro Zeman and *Renewable Energy Resources*. 2 ed. 2006 by John Twidell & Tony Weir. Theory collected from other sources is referenced in the text. The theory that is relevant for heat transfer is mainly collected from the book "*Heat and Mass Transfer: Fundamentals and Application*", fifth edition, by Yunus A. Çengel and Afshin J. Ghajar.

2.1 Solar irradiation

The amount of power produced by a photovoltaic (PV) system is mostly dependent on how much solar radiation the photovoltaic system receives. This makes solar irradiance of great importance when a PV-system is designed and when choosing a location.

The total irradiance of the solar radiation outside the Earth's atmosphere is estimated to be an average of 1361 W/m^2, known as the solar constant. This average is based on a mean Earth-Sun distance, on a plane perpendicular to the direction of the sun.

When solar radiation passes through the atmosphere of the Earth, it is attenuated. This is due to scattering and absorption by air molecules and dust particles. Under clear sky conditions, the distance through the atmosphere is the most important parameter for solar irradiance. This distance is at its shortest when the sun is directly overhead, i.e., at zenith. The solar irradiation incident on the Earth's surface is at its largest when the sun is at zenith under clear sky conditions.

To quantify the effect of the distance on the solar irradiation going through the atmosphere, the air mass (AM) is used. The air mass is given by:

$$AM = \frac{1}{\cos(\theta_z)} \tag{1}$$

As shown in figure 1, when the sun is directly overhead, the θ_z is zero. As the sun moves away from the zenith the value of θ_z increases. The angle θ_z is the angle between the sun's position and zenith.

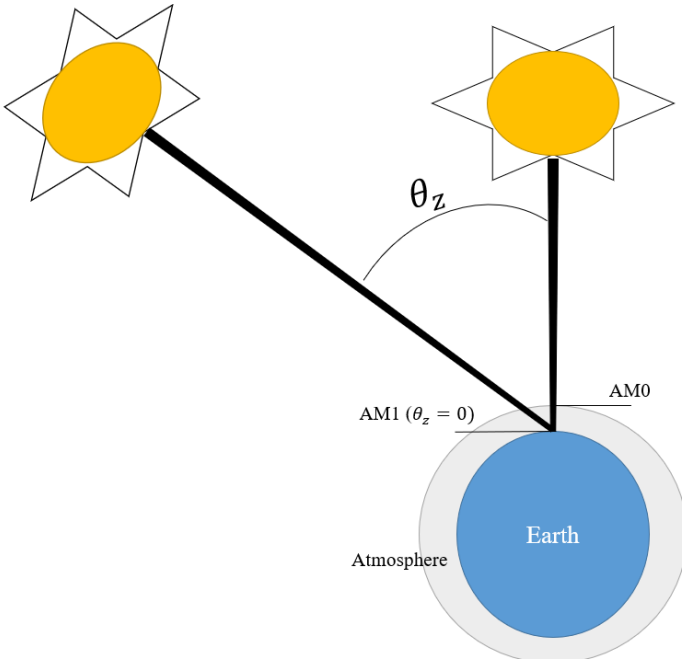

Figure 1: Distance between the sun and the earth, measured by air mass.

The actual amount of solar radiation that reaches a specific place on earth depends on multiple factors. Regular daily and annual variation such as the motion of the sun and local weather conditions will affect local amounts of irradiation. It is particularly the different components of solar irradiation that will be affected. The direct component of solar irradiation is the component that directly reaches the surface, while the diffuse component is created through scattering of the sunlight in the atmosphere.

On average, about 30 percent of the extraterrestrial solar intensity is reflected into space [6]. Most of it is reflected by clouds, while a small portion is reflected from the Earth's surface. The reflective ability of a surface is called the albedo effect and varies with atmospheric conditions among other things.

2.2 Photovoltaic theory

Solar cells are made of semiconducting materials and will, under the right conditions, produce electricity because of the underlying photovoltaic effect.

The most widely used semiconducting material is silicon (Si). Silicon, with fourteen electrons orbiting the nucleus, have four electrons in the outermost shell. These are called valence electrons and can interact with other atoms by forming chemical bonds. This is the case for the crystalline silicon where each Si atom is covalently bonded to four neighboring Si atoms. At temperatures higher than 0 K these bonds start to break because of the absorption of thermal energy [7]. The result of these broken bonds is the liberation of valence electrons,

which makes them mobile. The position of the missing electron is regarded as a positive charged hole. The situation described is presented visually in Figure 2.

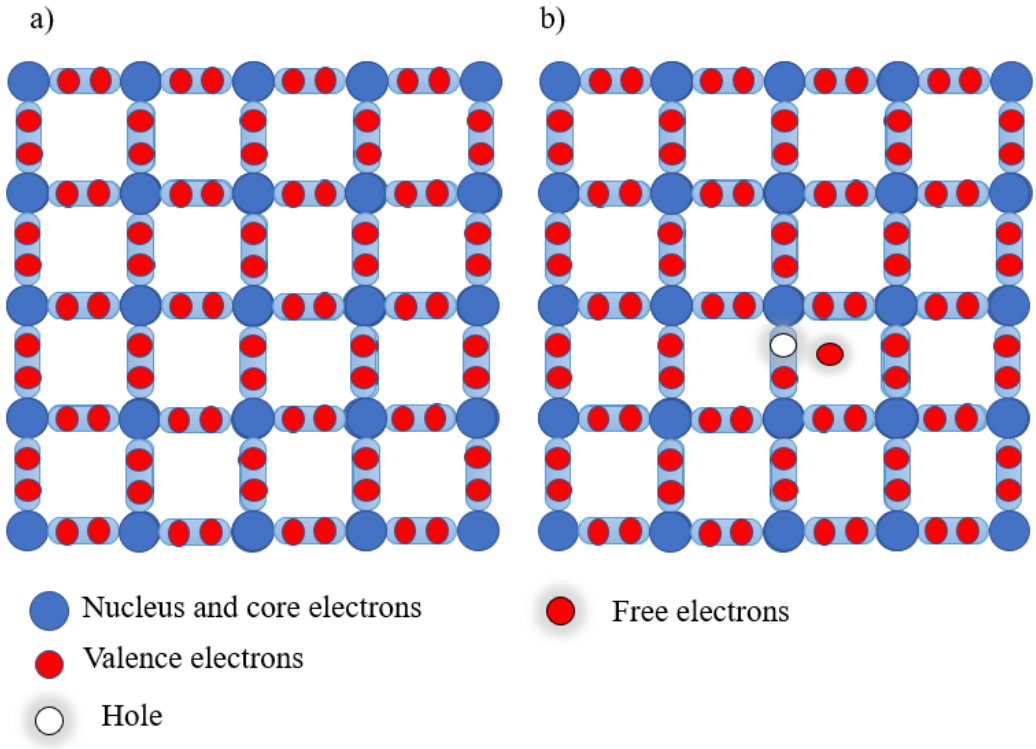

Figure 2: Bonding model for Si with an example of a free electron and hole in b [8].

The electrons can exist in allowed energy states, called energy bands. Valence electrons have their allowed energies in the valence band (VB), while the allowed electrons liberated from the covalent bonds form the conduction band (CB) [7].

The energy difference between these two bands is called the band gap energy, E_G, where:

$$E_g = E_{cb} - E_{vb} \tag{2}$$

E_{cb} is the minimum attainable conduction-band energy and E_{vb} is the maximum attainable valence-band energy.

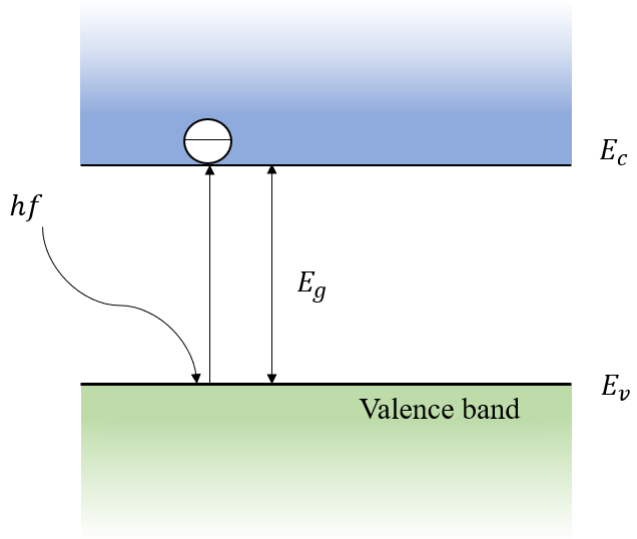

Figure 3: Band gap between conduction and valence band [9].

If the material is exposed to solar irradiance, it can excite electrons from the valence band to the conduction band. If the energy of the photon. E_{ph}, absorbed by the electron meets the criteria of:

$$E_{ph} \geq E_g \Leftrightarrow hf \geq E_g \tag{3}$$

it will be excited to the conduction band. The excess energy, energy above E_G, will be converted to heat. The energy of a photon is here given as $E_{ph} = hv$, where h is Planck's constant and f is the frequency.

A semiconductors ability to create electrical currents depends on the concentration of carriers that can transport charge. This concentration can be manipulated through doping. When a material is doped to form an n-type region and a p-type region, we get a junction between the two regions. Because of diffusion of electrons from the n-type side to the p-type side and holes from the p-type side to the n-type side, an electric field is formed, and a depletion region is created.

For a solar cell to generate power, both voltage and current must be present. When a solar cell is exposed to irradiation and the photon energy is higher than the band gap energy, electron-hole pairs are generated. These pairs are kept separated from each other by the pn-junction and the electric field. If the cell is short-circuited, emitter and base are connected, an electrical current will flow, known as the short-circuit current, I_{SC} [10].

If the light-generated carriers are prohibited from leaving the cell, they will build up. An increase in the number of electrons in the n-type side and an increase in holes at the p-type side creates an electric field opposite to the already existing electric field. This reduces the net electrical field and increases the diffusion current, I_D, across the junction. As a result, a voltage across the pn-junction occur. The open-circuited voltage, V_{OC}, is the voltage that creates a balance between the light-generated current, I_L, and the diffusion current.

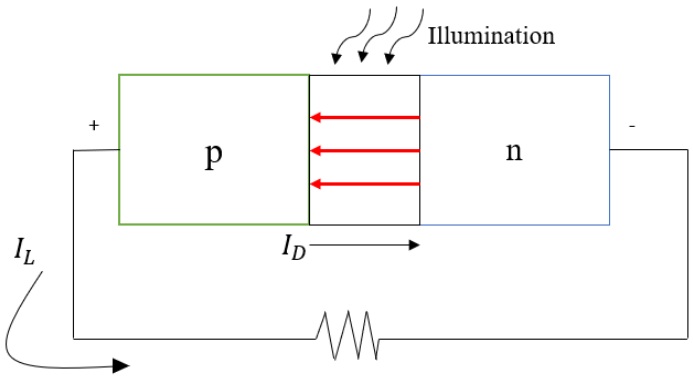

Figure 4: Solar cell under illumination. The red arrows indicate the electric field in the pn-junction. The diffuse current I_D travels over the pn-junction, while the light-generated current travels over the outer circuit.

Figure 4 shows an example of a solar cell under illumination where the net current is given by $I = I_D - I_L$.

2.2.1 Two-diode model

The solar cell can also be understood by the equivalent circuit; the two-diode model. The equivalent circuit of a solar cell based on the two-diode model is shown in figure 6. The two-diode model describes the solar cell by two diodes, one ideal and one non-ideal, shunt resistance and series resistance. The ideality of the diodes is given by their ideality factors, n_1 and n_2. An ideality factor equal to one represents an ideal diode, while a factor higher than one represents a non-ideal diode. Therefore, the two-diode model tries to explain the solar cell as non-ideal with internal losses.

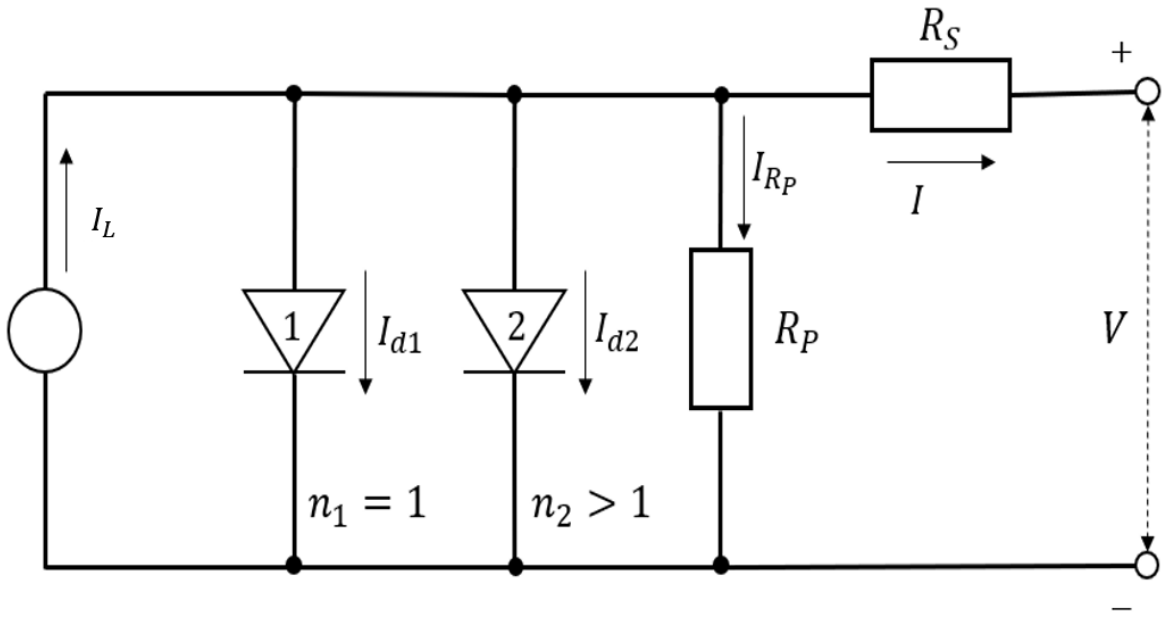

Figure 5: The two-diode model [11].

The second diode represents losses in the cell due to recombination of electron-hole pairs in the pn-junction. I_L represents the light generated current in the solar cell. The shunt resistance, R_p, reduces the current in the pn-junction and mimics manufacturing defects. The series resistance, R_s, represents the resistance of the top and rear metal contacts as well as the contact resistance between the semiconductor and the metal and the internal resistance in the semiconductor.

The I-V characteristics of the equivalent circuit of the two-diode model is given by:

$$I = I_{ph} - I_{01}\left\{exp\left[\frac{q(V - IR_s)}{n_1 k_B T_{cell}}\right] - 1\right\} - I_{02}\left\{exp\left[\frac{q(V - IR_s)}{n_2 k_B T_{cell}}\right] - 1\right\} + \frac{V - IR_s}{R_p} \quad (4)$$

Where I is the net current in the model, V is the voltage in the model, T_{cell} is the cell temperature in Kelvin, k_B is Boltzmann's constant and q is the elementary charge. I_{01} and I_{02} represents the saturation current in the diodes and n_1 and n_2 is the ideality of the diodes.

2.3 Solar cell parameters

To characterize the performance of solar cells and modules the main parameters that are used are:

P_{max}: Maximum power point

I_{SC}: Short-circuit current

V_{OC}: Open-circuit voltage

μ: Conversion efficiency (reference)

The maximum power is given by:

$$P_{max} = I_{MPP}V_{MPP} \tag{5}$$

I_{MPP} and V_{MPP} represents the current and voltage at the maximum power points of operation.

The P_{max} is the point on the solar cells IV-characteristics, which the solar cell has maximal power output. Figure 6 display's this characteristic and highlights the point in which the maximum power point is.

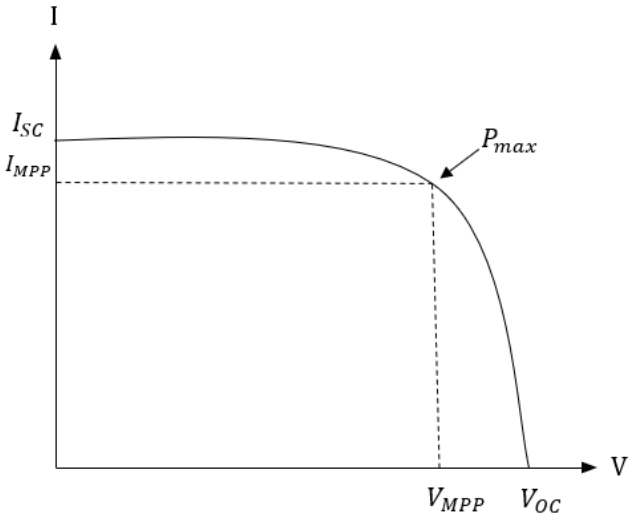

Figure 6: I-V curve displaying the characteristics of a solar cell.

P_{max} is the maximum power the PV-module can deliver while illuminated with standardized AM1.5 spectrum and irradiance of 1000 $\frac{\mathrm{W}}{\mathrm{m}^2}$. The modules conversion efficiency is then calculated as the ratio of P_{AC}, the power generated by the module, and the irradiance onto the module, G_m, times the surface area, A.

$$\mu = \frac{P_{AC}}{G_m A} \tag{6}$$

For a horizontal module will G_m be equal to the global horizontal irradiance (GHI). The efficiency provides information on how well the module or system converts solar energy to electrical energy but does not say anything about the performance of the system compared to the installed capacity. The efficiency from equation eight is the efficiency of the entire system and includes losses in the cables and the inverter.

2.4 Factors that affect power production

Many factors affect the amount of power produced by a PV-system. Those of most importance to the work done in this thesis is mentioned below.

2.4.1 Shading

Shading can affect the performance of a PV system to a large extent. Shading of one module will affect the power output of the entire string.

Partially shading from a nearby object, like a tree or objects that have fallen onto the module, like bird feces or a leaf, can cause the specific cell that is shaded to overheat. High temperatures in the solar cell can cause the encapsulation material to crack or other material to wear out. Solar modules are therefore constructed with bypass-diodes which allows the current to pass through the diode when cells are shaded.

2.4.2 Orientation and tilt

The power received by a PV module is largely dependent on the angle between the module and the sun. When the module surface and the sunlight are perpendiculars, the power density will equal that of the sunlight [12].

The solar irradiance that is incident on a tilted surface is the sum of the different components in play.

$$G_m = G_m^{diff} + G_m^{direct} + G_m^{ground} \tag{7}$$

Where G_m is the total in-plane irradiance, G_m^{diff} is the diffuse irradiance from the sky, G_m^{direct} is the direct component of the irradiance and G_m^{ground} is the irradiance reflected from the ground. This is illustrated in Figure 7.

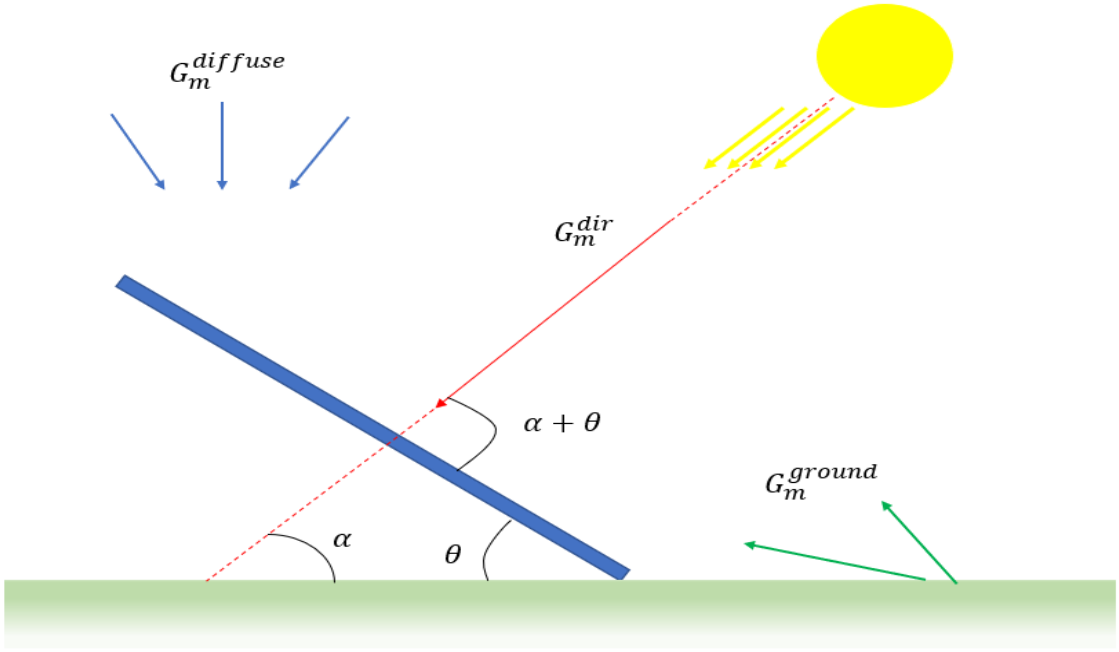

Figure 7: Illustration of different components of irradiance and important angles for calculating irradiance in a specific plane [9].

The angle θ is the tilt angle of the module and α is the angle between the direct irradiance and the horizontal. The components of irradiance are also dependent on the location of the sun.

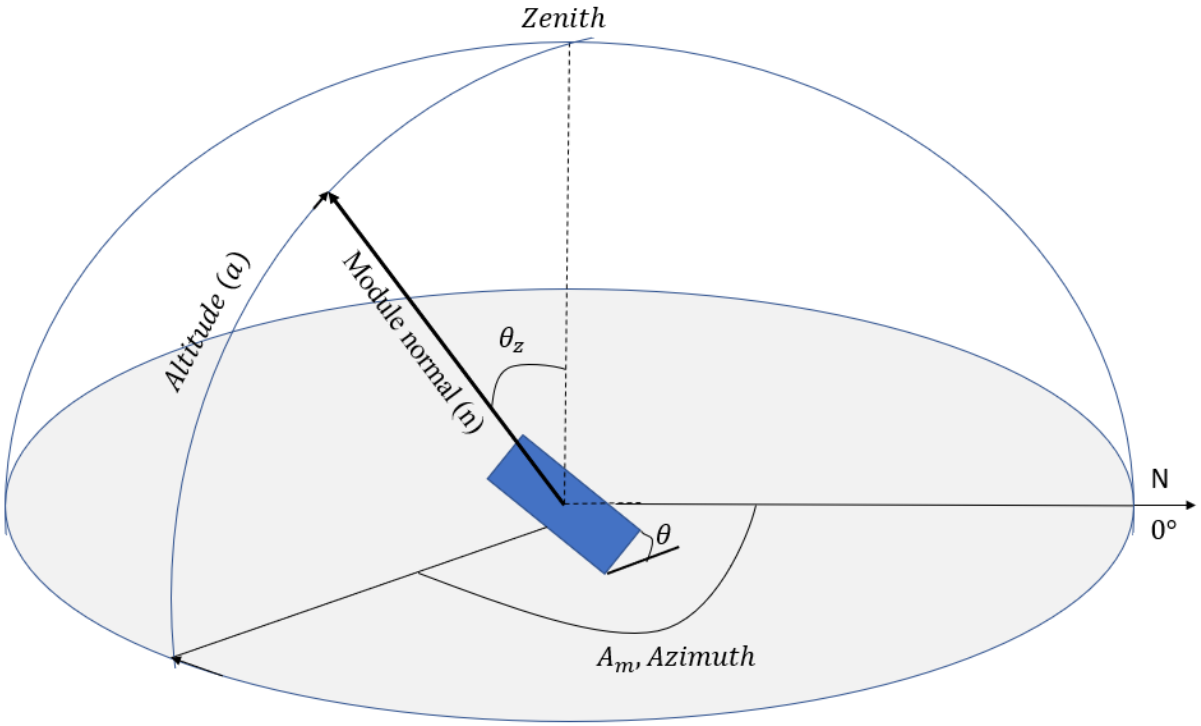

Figure 8: The necessary angles used to describe the orientation of the PV-module installed on a horizontal plane[9]. The blue object in the middle represents a PV-module.

Where θ_z is the zenith angle and A_m is the azimuth angle. The standard convention is defined as degrees from north, where 180° is south.

The component contributed by the reflection of the ground, G_m^{ground} is calculated with the equation [13]:

$$G_m^{ground} = GHI \times \rho \times \left(\frac{1 + cos(\theta)}{2}\right) \tag{8}$$

Where GHI is the global horizontal irradiance, ρ is the ground albedo, and θ is the module tilt.

To calculate the diffuse irradiance from the sky onto the tilted surface, the isotropic sky model is used [14]. The model treats the sky as a uniform source of diffuse irradiance, and the diffuse irradiance is then determined by:

$$G_m^{diff} = DHI \times \left(\frac{1 + cos(\theta)}{2}\right) \tag{9}$$

DHI is the diffuse horizontal irradiance.

To calculate the diffuse horizontal irradiance, the Erbs model is used. The Erbs model estimates the diffuse horizontal irradiance from global horizontal irradiance *(GHI)* and the *diffuse fraction (DF)* [15]. This gives the equation for DHI:

$$DHI = DF \times GHI \tag{10}$$

The Erbs model is also used to calculate the direct normal irradiance (*DNI*) by:

$$DNI = \frac{GHI - DHI}{cos(\theta_z)} \tag{11}$$

The direct component on the plane of array (POA), G_m^{direct} is calculated with the equation [7]:

$$G_m^{direct} = DNI \times cos(AOI) \tag{12}$$

Where AOI is the array angle of incidence. This is the angle between the solar vector and the surface normal [15]. The AOI is given as [16]:

$$AOI = cos^{-1}\left(cos(\theta_z)\,cos(\theta) + sin(\theta_z)\,sin(\theta)\,cos\left(A_m - A_{m_{array}}\right)\right) \qquad (13)$$

Where $A_{m_{array}}$ is the azimuth angle of the module. A module facing south has an azimuth of 180 degrees.

2.4.3 Cell temperature

When the cell temperature increase, the energy of the electrons in the semiconductor also increase. This will reduce the band-gap size and lower the energy that is needed to break the bonds [17]. This ultimately leads to higher short-circuit currents, I_{SC}, and a lower open-circuit voltage, V_{OC}.

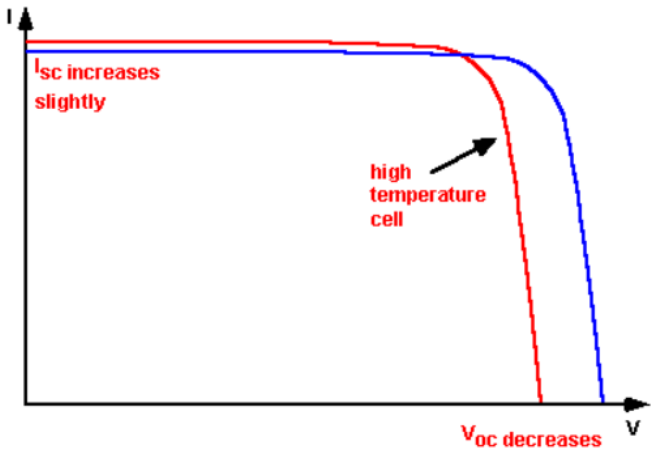

Figure 9: IV - curve for to solar cells, one with a higher temperature [6]

Figure 9 displays the effect of panel temperature on the performance of a PV panel. The results are gathered using PVsyst [18]. Increase in cell temperature will give IV-curves with lower maximum power readings. Figure 10 displays the relationship between efficiency and solar irradiance at different cell temperatures. It is evident from the figure that higher cell temperature gives a lower efficiency.

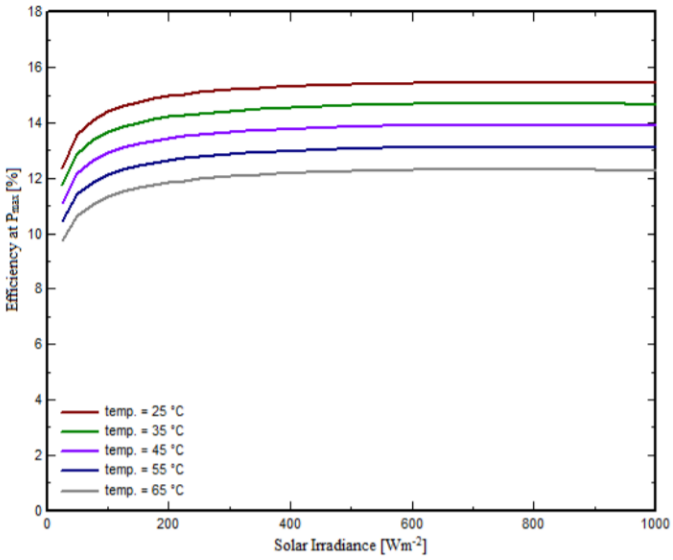

Figure 10: Efficiency of the solar panel at different panel temperatures and solar irradiances [7].

The relationship between cell temperature and efficiency can be modulated with the equation [19]:

$$\eta = \eta_{T_{ref}}\left[1 - \beta_{ref}\left(T_{cell} - T_{ref}\right)\right] \tag{14}$$

Where, $\eta_{T_{ref}}$ is the module efficiency at standard test conditions (STC). More specifically at the reference temperature, T_{ref}, and solar irradiance at $1000\ W/m^2$. T_{cell} is the cell temperature and β_{ref} is the temperature coefficient provided by the manufacturer. The definition of STC is:

- Cell temperature of 25 ℃
- Irradiance 1000 W/m^2
- Air mass (AM) at 1.5

The module efficiency, η, is not a constant value and will change when the operation conditions deviate from STC.

The cell temperature, T_c, can be derived from measured back-surface temperature with equation [20]:

$$T_{cell} = T_m + \frac{G_m}{G_{STC}}\Delta T \tag{15}$$

T_m is the module back-surface temperature, while G_m is the solar irradiance measured and G_{STC} is the reference solar irradiance on the module, 1000 W/m^2. ΔT is the temperature difference between the cell and the module back-surface at an irradiance of 1000 W/m^2.

Temperature differences in solar cells can be observed by using thermography. Thermography or thermal imaging uses a small range of the infrared spectrum to detect and visualize thermal radiation. Every object with a temperature above 0 K will emit thermal radiation. The temperature of the object will affect the amount of radiation and the distribution as a function of wavelength [21].

2.5 Heat transfer

The efficiency of solar modules is reliant on the operational cell temperature. The cell temperature is dependent on the effects of heat transfer, through convection, radiation, and conduction.

2.5.1 Conduction

Conduction is the process of energy transfer from more energetic particles in one substance to less energetic particles in another substance because of interactions between particles. Conduction through a plane layer, as shown in figure 9, follows the equation:

$$\dot{Q}_{cond} = \frac{kA(T_1 - T_2)}{\Delta x} = -kA\frac{\Delta T}{\Delta x} \tag{16}$$

Where k is the thermal conductivity of the material, which is the materials ability to conduct heat. A represent the surface area of heat transfer, ΔT the temperature difference across the area and Δx is the thickness of the layer.

Equation 12 can also be written like this:

$$\dot{Q}_{cond} = \frac{(T_2 - T_1)}{R_{cond}} \tag{17}$$

Where

$$R_{cond} = \frac{\Delta x}{-kA} \tag{18}$$

is the thermal resistance of the plane layer. It describes the layer's resistance to conduct heat.

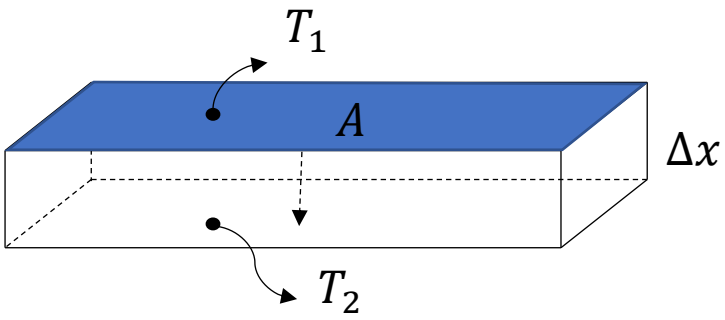

Figure 11: Plane layer with a temperature difference.

2.5.2 Convection

Convection is energy transfer between a solid surface and the liquid or gas in motion, adjacent to the solid. The rate of heat transfer is dependent on the velocity of the fluid and the motion type. Convection is categorized either as forced or natural. It is called forced convection if the fluid motion is forced to flow over a surface by an external force, set up by a device, like a pump or a fan. Natural convection, also called free convection, means that the forces behind the fluid flow are caused by variations in density, which is typically temperature-dependent.

The rate of convection heat transfer follows the equation:

$$Q_{conv} = hA(T_s - T_\infty) \tag{19}$$

Where h is the convection heat transfer coefficient, T_s is the surface temperature and T_∞ is the temperature of the fluid sufficiently far away from the surface.

The equation for heat transfer in the form of convection can also be written in the form:

$$Q_{conv} = \frac{T_s - T_\infty}{R_{conv}} \tag{20}$$

Where,

$$R_{conv} = \frac{1}{hA} \tag{21}$$

At the solid surface, the velocity of the fluid is zero. This is due to viscous effects and is known in modeling terms as a no-slip condition. Figure 12 shows the velocity of the fluid and how it changes in distances from the plate.

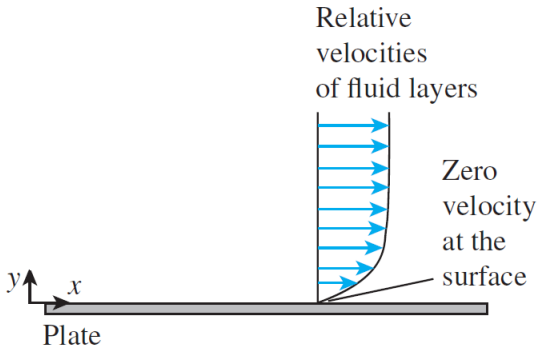

Figure 12: Velocity of a fluid over a flat plate [1].

This condition implies that the heat transfer from the surface to the fluid layer adjacent to the surface is by pure conduction since the fluid layer is motionless. The layer that sticks to the surface will then slow down the adjacent fluid layer and so forth. This gives rise to the velocity boundary layer and the velocity profile exhibited in Figure 12. Heat is transported away from the surface through conduction and the velocity of the fluid. The Nusselt number is used to describe the enhancement of heat transfer through a fluid layer because of convection relative to conduction across the same fluid layer. The larger the Nusselt number, the more effective the convection. The Nusselt number follows the equation:

$$Nu = \frac{hL_c}{k} \tag{22}$$

Where k is the thermal conductivity and L_c is a characteristic length. Equation 24 can be rearranged to:

$$h = \frac{Nuk}{L_c} \tag{23}$$

Like the velocity boundary layer, a thermal boundary layer will develop when a fluid flows over a surface with a different temperature. When a liquid or a gas flow over a heated surface, both the velocity and the thermal boundary layer develop simultaneously. Prandtl's number, Pr describe the relative thickness of these layers:

$$Pr = \frac{\mu C_p}{k} \tag{24}$$

Where μ is the dynamic viscosity, C_p is the specific heat capacity and k is the thermal conductivity.

The type of flow will also affect heat convection. Laminar flow is ordered and characterized by smooth layers of fluid. Highly disordered fluid motion that often occurs at high velocities

and is characterized by fluctuations in velocity is called turbulent. An alternating form of fluid motion between laminar and turbulent is called transitional.

The transition between laminar and turbulent flow depends on multiple factors, like surface geometry, surface roughness, flow velocity, fluid temperature, and fluid viscosity. The Reynolds number determines the flow profile, either laminar or turbulent, based on the ratio of inertia forces to viscous forces in the fluid

$$Re = \frac{vL_c}{\nu} = \frac{\rho v L_c}{\mu} \tag{25}$$

Where v is the upstream velocity, L_c is a characteristic length and ν is the kinematic viscosity. The kinematic viscosity is the ratio of dynamic viscosity to density of the fluid. High Reynolds numbers indicate turbulent flow, while a low number suggests laminar flow.

The average Nusselt number over a flat plate will rely on the value of Re and Pr. It is given by the equations [1]:

$$Nu = \begin{cases} 0.664Re^{0.5}Pr^{\frac{1}{3}}, & Re < 5 \times 10^5 \; and \; Pr > 0.6 \\ 0.037Re^{0.8}Pr^{\frac{1}{3}}, & 5 \times 10^5 \leq Re \leq 10^7 \; and \; 0.6 \leq Pr \leq 60 \end{cases} \tag{26}$$

For natural convection, the ratio between the buoyancy force and viscous force acting on the fluid is of most interest. This parameter is called the Grashof number, Gr:

$$Gr = \frac{g\beta(T_s - T_\infty)L_c^3}{\nu^2} \tag{27}$$

Where g is the gravitational acceleration, β is the coefficient of volumetric thermal expansion, T_s and T_∞ are the surface and ambient temperature, L_c is a characteristic length and ν is the kinematic viscosity. The product of Grashof's number and Prandtl's number is the Rayleigh number, Ra.

$$Ra = Gr\,Pr = \frac{g\beta(T_s - T_\infty)L_c^3}{\nu^2} Pr \tag{28}$$

The average Nusselt number in natural convection are typically derived from the Rayleigh number:

$$Nu = CRa_L^n \tag{29}$$

The factor C is a constant coefficient that is dependent on the geometry of the surface and type of flow, characterized by the size of the Rayleigh number. For a horizontal plate with a hot upper surface the Nusselt number is given by the equations [1]:

$$Nu = \begin{cases} 0.59Ra^{\frac{1}{4}}, & 10^4 < Ra < 10^7 \\ 0.1Ra^{\frac{1}{3}}, & 10^7 < Ra < 10^{11} \end{cases} \quad (30)$$

In the case of a hot lower surface the Nusselt number follows the equation [1]:

$$Nu = 0.27Ra^{\frac{1}{4}}, 10^5 < Ra < 10^{11} \quad (31)$$

When a surface interacts with a liquid or a gas at a different temperature, a temperature gradient will always be present. This gives rise to buoyancy-driven flow, which means that forced convection is always accompanied by natural convection. Heat transfer through forced convection is usually much higher than that of natural convection, and it is therefore often ignored. To evaluate whether natural convection can be ignored, the ratio of the Grashof number to the squared Reynolds number is used. This represents the ratio of the importance of natural convection relative to forced convection. The ratio is called the Richardson number, Ri:

$$Ri = \frac{Gr}{Re^2} \quad (32)$$

$Ri < 0.1$ indicates that natural convection is negligible,

$Ri > 10$ indicates that forced convection is negligible and

$0.1 < Ri < 10$ indicates that both natural and forced convection must be considered.

In the case of combined heat transfer through natural and forced convection, experimental data indicate that the Nusselt number can be calculated as:

$$Nu_{combined} = \left(Nu_{forced}^n \pm Nu_{natural}^n\right)^{\frac{1}{n}} \quad (33)$$

Where the direction of flow determines whether the Nusselt numbers are added or subtracted. For transverse and assisting, a plus sign will be used, while a minus sign for opposing flows. The value of n is dependent on the geometry used and is determined experimentally.

2.5.3 Radiation

The net rate at which radiation leaves a surface of object i to an object j is given as:

$$Q_{i\to j} = A_i e_i \sigma\left(T_i^4 - T_j^4\right) \quad (34)$$

Where A_i is the area of object i, e is the emissivity and σ is the Stefan-Boltzmann constant.

2.6 Components and Performance of a grid-connected PV system

2.6.1 Solar cells, modules, and strings

Solar cells lay the foundation for PV systems. They are responsible for the conversion of sunlight to electrical currents. The operating voltage of one single cell is low, and the cells are therefore connected in series, creating a PV module. The voltage over several cells in series is the sum of the voltage from each cell. The current is determined by the cell that delivers the smallest current in the series. Multiple PV modules connected in series form a PV string. This string or multiple strings can then be connected to an inverter.

2.6.2 Inverter

The main function of the inverter is to turn DC power from the PV string into alternating current (AC) power that is compatible with the requirements of the grid. Another essential feature of the inverter is maximum power point tracking (MPPT) to ensure maximum power. To achieve maximum power output from a module, it must be forced to operate at the maximum power point (MPP), which means to force the voltage of the PV module to be that of the MPP [7]. The MPP will differ, depending on the ambient conditions, like irradiance and temperature. Therefore, the inverter must track these changes of the ambient conditions, a process called MPP tracking.

The inverter will also impose some losses on the system. Even though some of the losses can be avoided by sizing the inverter correctly, the efficiency of the inverter will vary under different operational conditions and contribute with some loss. The loss in the inverter can be defined as the ratio of P_{Dc} to P_{AC} given as:

$$\mu_{inverter} = \frac{P_{DC}}{P_{AC}} \quad (35)$$

The cables will also impose losses on the system. These losses are dependent on the diameter, length, and resistance of the cable. The losses in the system due to cables will usually not amount to more than 2 percent of the system losses

2.6.3 Performance of a grid-connected PV system

The performance ratio is an important metric in the PV industry and can be used for contractual conditions and as a comparability metric between facilities.

The performance ratio (PR) is the ratio of the actual to the theoretically possible energy outputs [22]. The theoretically possible energy output is calculated as the product of the rated efficiency of the PV modules, η_{ref}, and the radiated power onto the module. This is the energy produced if the system was continuously working under STC conditions, with STC efficiency. The actual energy output is the actual reading from PV-plant production. The formula used in this thesis is given as:

$$PR = \frac{P_{AC}}{\eta_{ref} G_m A} \tag{36}$$

Where P_{out} is the plant output from the inverter and G_m is the irradiance energy measured for the system. The *PR*-value can be calculated for momentarily values, using plant output and irradiance, or as a *PR*-value over a set time frame. The *PR*-value for a month will then be based on the solar irradiation for that month and the produced energy from the plant.

The PR includes all the losses in the system, within the period of data used to calculate the metric. It includes optical losses, losses associated with the array, such as PV conversion, module quality and aging, and losses from system components, like inverter efficiency and cable losses.

PR is not directly dependent on irradiation or orientation, and therefore allows a comparison between facilities. PR is, however, dependent on which periods that are used for calculation. If shorter time-periods are used can this affect the interpretation and comparability of the PR metric. PR is also dependent on the cell temperature, in such that, factor contributing to lower cell temperature will have a positive impact on the PR.

2.6.4 Costs

Levelized cost of energy (LCOE) gives a measurement of lifetime costs divided by energy production. The LCOE includes a calculation of the present value of the total cost of building and operating a power plant over an assumed lifetime [23]. This will allow for comparisons

between different technologies of unequal life spans, project sizes, capacity, capital costs, and risk. The LCOE can be calculated from the equation [24]:

$$LCOE = \frac{\sum_{t=1}^{n} \frac{IN_t + OM_t + F_t}{(1+r)^t})}{\sum_{t=1}^{n} \frac{E_t}{(1+r)^t})} \quad (37)$$

Where IN_t is the investment expenditure in year t, OM_t is the operations and maintenance costs in year t and F_t is the fuel expenditures in year t. E_t represents the electricity generation in year t, r is the discount rate, and n is the assumed lifetime of the system.

3 Floating PV

Accompanied by the market growth in solar PV has new technologies to better utilize solar irradiation through PV technology emerged. Floating PV presents an exciting and relatively new way of harnessing energy with solar modules. Floating PV is based on system installation over water bodies. The Floating PV systems include multiple components for floating, like moorings and pontoons, depending on the technology deployed. Multiple floating PV systems exist to this day, both on water bodies in-land and off-/near-coast. They differ broadly in the technology used and how it capitalizes on the benefits of floating PV.

As reported in the report "*Where Sun Meets Water: Floating Solar Market Report*" there has been a substantial increase in floating PV systems since the first system was installed in 2007 in Japan [25].

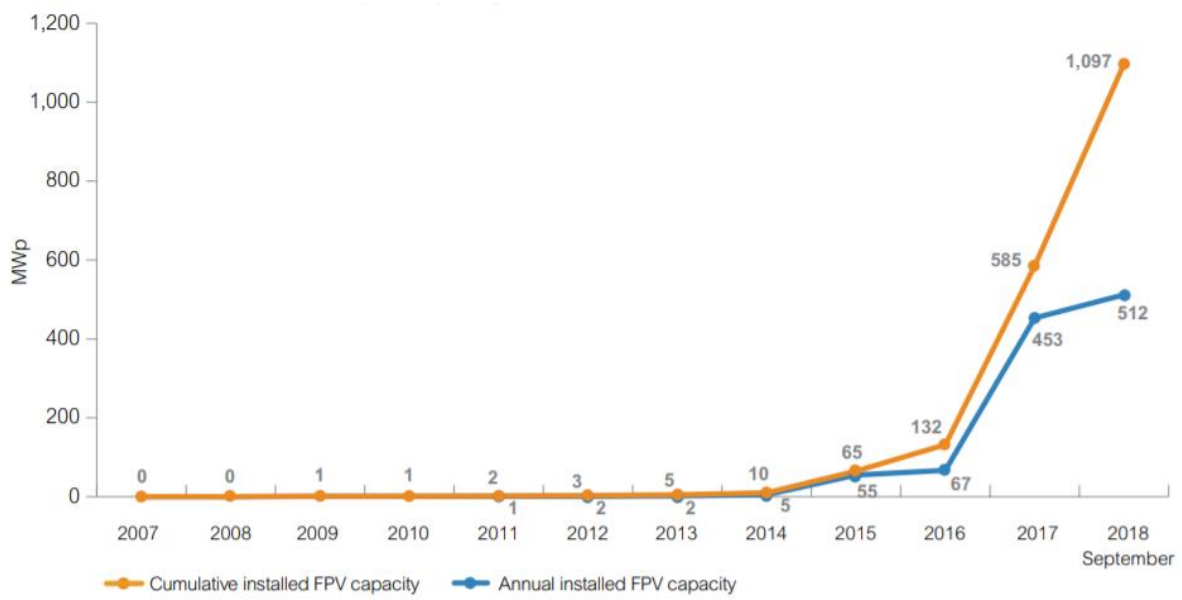

Figure 13: Development of installed capacity worldwide for FPV [25].

Figure 17 shows the strong growth in installed capacity. Japan and China constitute most of the installed capacity for floating PV. Japan has the largest distribution of floating PV plants while the current largest floating PV plant is in China.

3.1 Benefits of Floating PV

3.1.1 Land management

Drop in prices, rise in energy demand and national and international governmental policies attracts new players to the PV industry. The significant growth previously seen can ultimately

be hindered if the land is not effectively managed. In densely populated countries or cities can the need for renewable energy create land-use conflicts. Water bodies provide an alternative for PV systems, which will relieve space for settlements or agriculture.

3.1.2 Improved efficiency

As evident in equation 15, the efficiency of a solar cell is dependent on the operational temperature. The operational temperature is affected by the environment in such a way that it can act as a coolant for the solar module which gives a lower operational temperature. For floating PV modules this will give an environment with greater cooling ability. From the work of Liu et al. it is found that a floating and a land-based system will have a 3.5℃ difference in operating temperature and an increase of 1.58-2.00% in efficiency for a floating system compared to a terrestrial based system [26]. Majid et al. reports of temperature differences ranging from 10℃ to about 15℃ from their off-grid experiment [27]. The effects and results of tests conducted on floating PV will rely on multiple factors, such as the floating PV system that is used, how it is mounted on the water and the environment in which the experiment is conducted.

3.1.3 Other benefits

Floating PV includes a range of other potential advantages, such as [25]:

- Reduced power loss due to the elimination of shading from the surroundings.
- Reduction in water evaporation from water reservoirs.
- Better water quality, through decreased algae growth.

3.2 Challenges with Floating PV

Depending on the installation site, near-shore, off-shore or inland water-bodies, will the requirements for the floating structure to withstand different forces be greater than structures on the land. Land-based PV systems may require that land areas are developed to meet the specifications and requirements of the ground, and this comes at a substantial cost. Floating PV does not have this cost but does have costs associated with mooring systems and maintenance of the system. Depending on the system setup, floating PV will also require an assessment of the seafloor to anchor the system safely.

As floating PV is a relatively new technology, without the benefit of having been tested over time, it is difficult to assess the long-time effect of corrosion due to water or high moisture air. The harsh environments near- and off-shore will also pose challenges. This can affect both the solar modules and the components for floating, leading to low module efficiencies and high maintenance costs.

3.2.1 Other challenges

- The effects on the environment based on covering water reservoirs with large floating PV systems is unknown.
- Large-scale floating PV systems can interrupt either trafficking of boats or recreational use of water-bodies.

3.3 Costs of Floating PV

The total project cost used for floating, mooring and electrical equipment needed for floating PV vary depending on the conditions at the specific location and the floating PV technology used. The cost related to the support structures can account for up to 25% of the total project costs [5, 28]. Moreover, the cost associated with operation and maintenance (O&M) is uncertain. The effects of natural cleaning by wind or water combined could reduce the costs, while corrosion from water or other environmental factors could increase them.

Floating PV does have a higher cost than ground-mounted PV [25]. Furthermore, it is reported that the total capital expenditures for turnkey floating PV installations in 2018 ranged between USD 0.8-1.2 per Wp [25]. These values are dependent on the location of the project and other conditions such as system size and the environment. There are large discrepancies and uncertainties relating to the cost of floating PV, mainly because of the lack of robust track records.

World Bank Group has done calculations of the Levelized Cost of Electricity (LCOE) for a generic 50 MW floating PV system and found that it does not substantially differ from that of a ground-mounted system for a range of discount rates. The LCOE calculations represent the break-even analysis at 5 percent higher expected energy yield. The results are rendered in table 1.

Table 1: LCOE (US cents/kWh) for different discount rates [25].The payback period is set to 20 years.

DISCOUNT RATE	GROUND-MOUNTED PV (FIXED TILT)	FLOATING PV (FIXED TILT)
7%	5	5.6
8%	5.2	5.7
10%	5.4	6

The governmental incentives for floating PV are the same as for ground-mounted in most of the countries, except for China and Taiwan who operates with higher feed-in tariffs for floating PV.

3.4 Ocean Suns system

The most common technology deployed in large floating PV plants is floaters on top of the water-body and modules fixed to these floaters. These systems do not draw on the full benefits of water cooling on module efficiency. Ocean sun has developed a floating system setup that aims to benefit fully from the cooling effect from the water. Ocean sun's system is comprised of a thin polymer membrane that carries the PV modules. This allows for thermal contact with water for the PV modules. Figure 14 shows the technology of Ocean sun with the polymer membrane and PV modules.

Figure 14: Ocean suns floating PV technology [29].

4 Method

The primary goal of this thesis is to study the performance of a specific floating PV technology developed by Ocean Sun. Production data and climatic data collected from the first Ocean Sun pilot at Skaftå will be analyzed and used to assess the performance. This chapter will present the floating PV system; it's site and setup. The chapter will then present three models for estimating module temperature throughout a day, based on different input parameters. Finally, a short analysis of differences between a horizontal floating PV-system and a system with tilted modules will be presented.

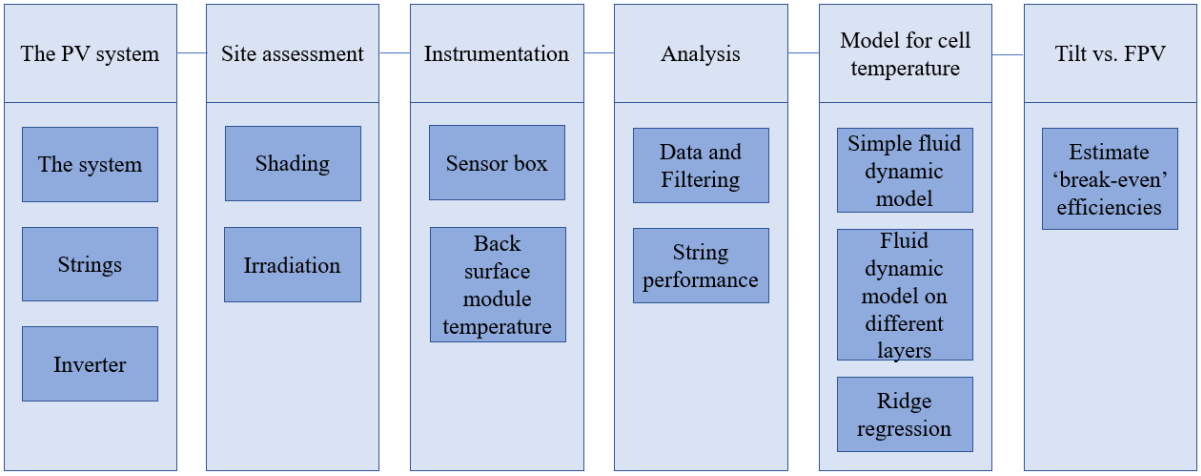

Figure 15: Flow chart of chapter structure.

4.1 The floating PV-system

Figure 16: a) The PV-system is located near the shore. b) Shows the shores proximity and the shelter of the dock. [30]

The PV system is in a fjord at Osteroy in Hordaland, with latitude 60.454 and longitude 5.622. The system is near-shore, as illustrated in Figure 16.

4.1.1 The system

The floating PV system is comprised of both the floating structure, the PV-modules, cables, and inverter. The modules are situated on a canvas which is floating directly on the water. Figure 17 and Figure 18 displays the solar modules on the canvas.

Figure 17: The solar modules on the canvas.

.

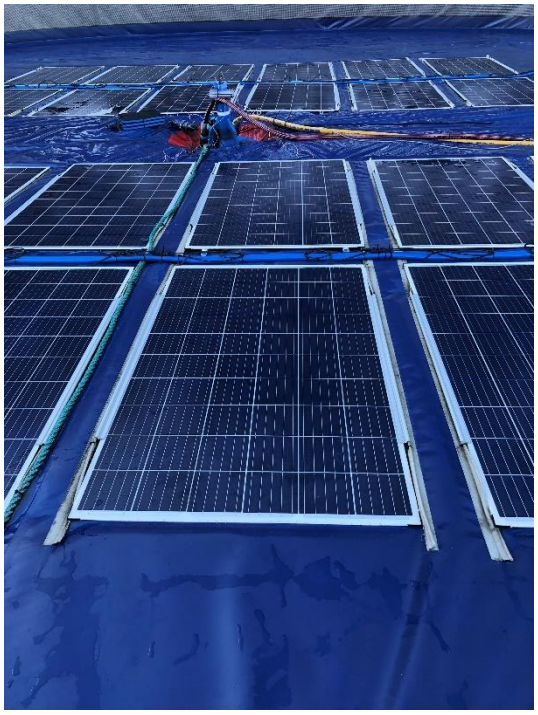

Figure 18: Solar modules on the floating canvas with a pump located between the strings.

The modules at this facility are of type 60 cells multicrystalline DUOMAX modules from Trina Solar. The modules have a rated power of 270 Wp, and the data sheet can be found in Appendix A. The modules are frameless glass-glass modules to ensure full contact with the canvas. The modules are placed in two strings with twelve modules each, connected to a 6-kW Fronius Primo 6.0-1 inverter. This gives the total system a rated power of 6.48 kWp.

The modules have junction boxes and cables on the backside which will reduce the area of thermal contact with the canvas. This creates local air gaps, which will affect the cooling from the water. In the middle of the canvas, there is a water pump, which pumps water out from the canvas and into the ocean again. The water is primarily freshwater from rain.

The system was installed in May 2017, but the PV modules were changed on the 23rd and 24th of May in 2018.

4.1.2 Strings

The system consists of two strings with 12 modules in each string connected to the inverter. The inverter tracks the power produced from both strings separately. To investigate the effect of Ocean Sun's system on the efficiency of the modules, one of the strings were lifted to create an air gap between the modules and the canvas. This can then be compared to the string which is in thermal contact with the canvas/water. After the string is lifted, the

production data, along with other parameters, will be investigated and the two strings will be compared. Figure 19 illustrates string 2 and string 1, where string 2 is the one that is lifted, and string 1 is in contact with the canvas.

Figure 19: Picture of the system at Skaftå as seen from above. The number one and two marks the string numbers [30].

The first trip to Skaftå and the floating PV-system was done the 5th of February 2019. During this visit, different methods for lifting the modules were tested, specifically different diameters on polypropylene (PP)-pipes placed between the modules and the canvas. Both 32 mm and 40 mm pipes were tested. To make sure that the canvas would not touch the modules between the pipes, it was decided that three 32 mm pipes were to be used. To test the effect of lifting the modules, two 40 mm pipes were left under two of the modules until the next site visit. Figure 20 displays the system 08:30 the morning after the modules were lifted. It is evident from the figure that modules that were lifted from the canvas are colder compared to the modules that are in contact with the canvas. They had frost on the surface and appear as white in the figure below.

Figure 20: Picture of the system 08:30 the day after the modules were lifted. The two white modules are the ones that were lifted and display signs of frost on their surface.

At the 26th of February, the rest of the modules of string 2 were lifted. As evident in Figure 21, there is an air gap between the modules and the canvas.

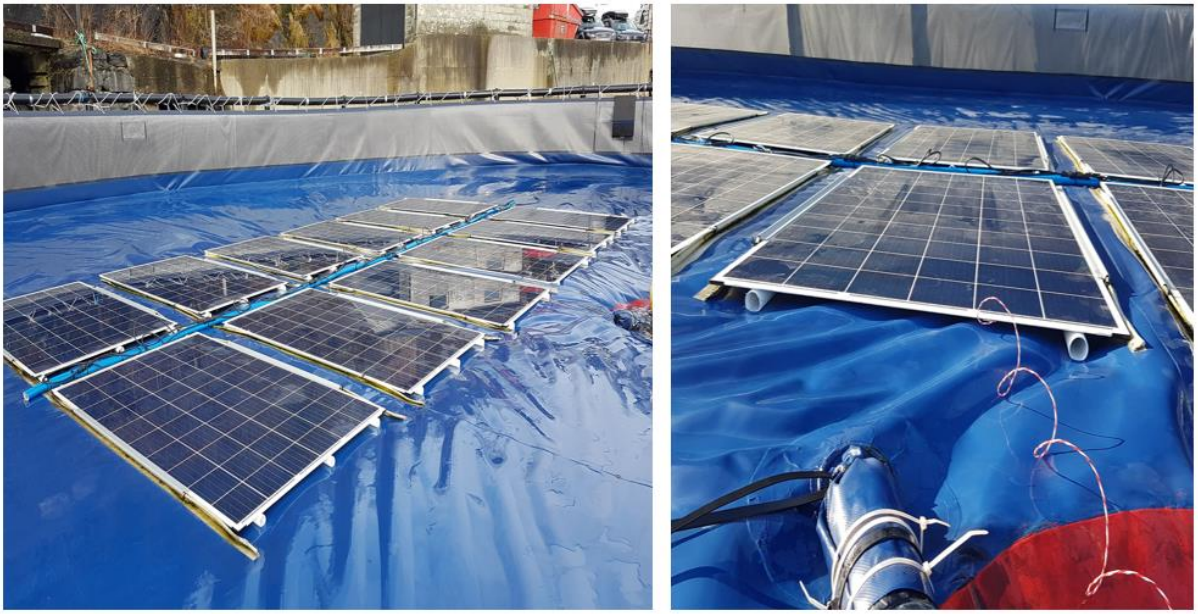

Figure 21: Figure shows how the modules are lifted. The one with the back-surface module temperature sensor has only two pipes between the module and canvas.

The picture to the right in the figure shows how the back-surface module temperature sensor is connected. The cable of the module temperature sensor is also reinforced using duct tape. This can affect the transfer of heat through the module but was necessary to ensure that the sensors did not fall of. This module is lifted with two pipes to allow room for the sensor. The pipes are fixed to their position using strips.

IV-measurements of both strings were done on three different occasions, two of which was done under too low irradiance. The result from these two measurements can be found in Appendix B. The last measurement was done on 24.04.2019. The apparatus used was a Tri-ka 0802201. The measurements are done with an uncertainty of ±1%

The data sheet for the apparatus is available in appendix A.

4.1.3 Inverter

The inverter used in this system is the Primo 6.0-1 string inverter delivered by Fronius. The data sheet is available in appendix A. The inverter is a 6-kW inverter with a maximum efficiency of 98.1%. The efficiency curve of the inverter is provided in Figure 22.

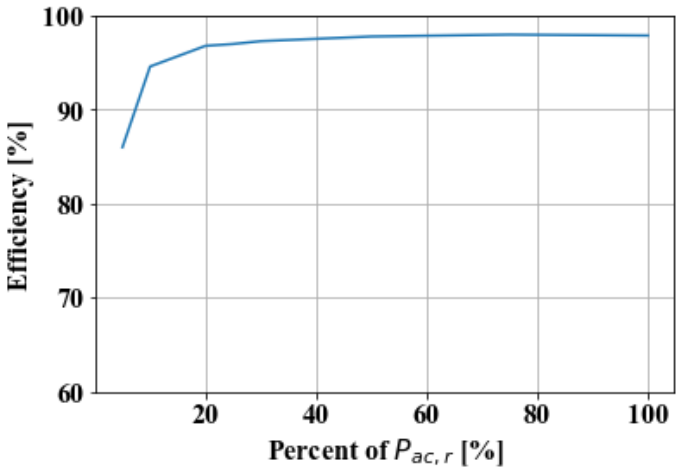

Figure 22: Efficiency curve of the Primo 6.0-1. The x-axis is the percent of rated output efficiency. The values are collected from the technical specifications of the inverter on the manufacturer's web page [31].

Fronius reports of an inverter accuracy of ±5%. This accuracy was provided over e-mail by Fronius technical support. The power is transported from the PV system to the onshore inverter by an approximately 20-meter-long cable.

4.2 Site assessment

4.2.1 Shading

The system is in a fjord with mountains on both sides. These mountains will shade for the sun in large parts of the day. This gives the system an unshaded operational time up until between 15:00 and 15:30. The average hourly production from the system is provided in the figure below. It illustrates how the production varies during a day and when shade affects the

produced power from the system. It is evident that the system on average start being shaded around 15:30. These values are averages of production every fifth minute for every day in the period 01.06.2018 to 31.12.2018.

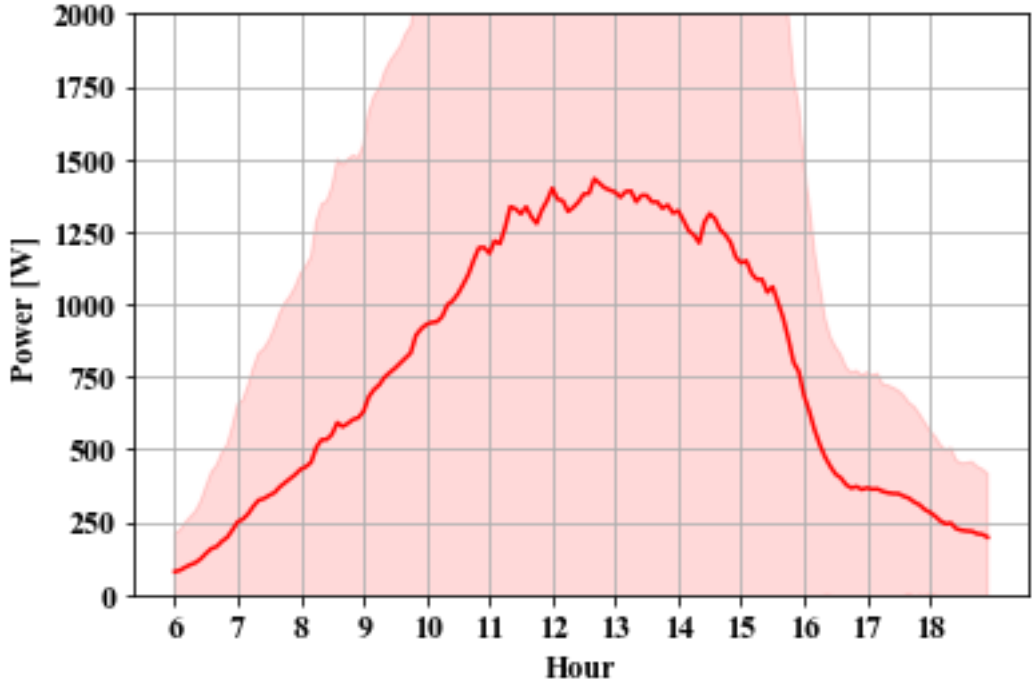

Figure 23: Average produced power with data from 01.06.2018 to 31.12.2018. The shaded area represents one standard deviation in both directions.

Apart from the mountains surrounding the system, the system should be free from partly shading from nearby objects. The movement of the sun changes over the year and these values will therefore also depend on the time of the year. Figure 24 displays how the production varies each month and points out how one filter for the entire period will affect the results.

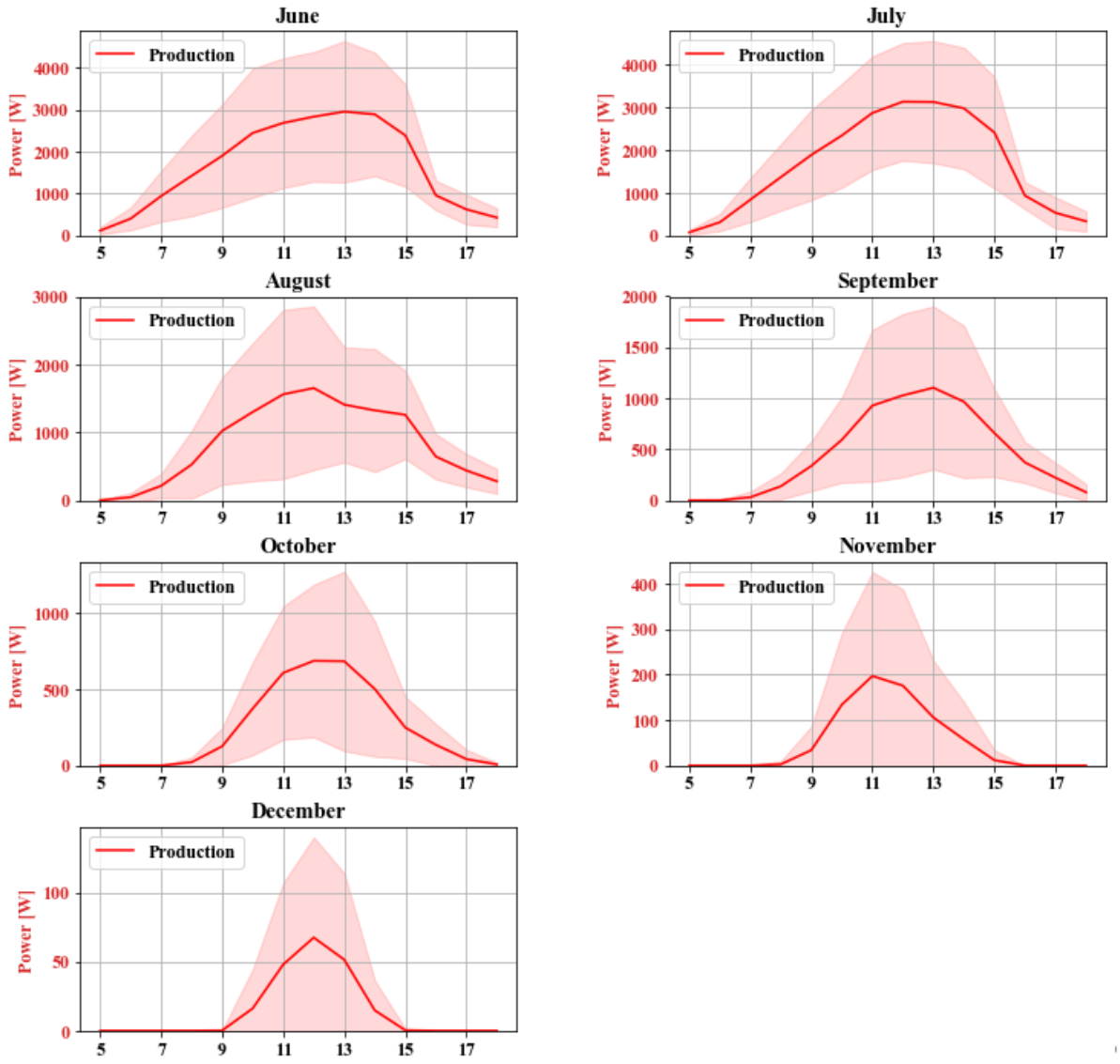

Figure 24: Power production averages every five minutes. The shaded area represents the standard deviation. Data from 01.06.2018 to 31.12.2018. The x-axis is hours throughout the day.

There are also some differences between the strings. The string closest to the shore, string 2, will be shaded earlier than string 1 in the afternoon. This will change throughout the year, but not much, as evident in Figure 25.

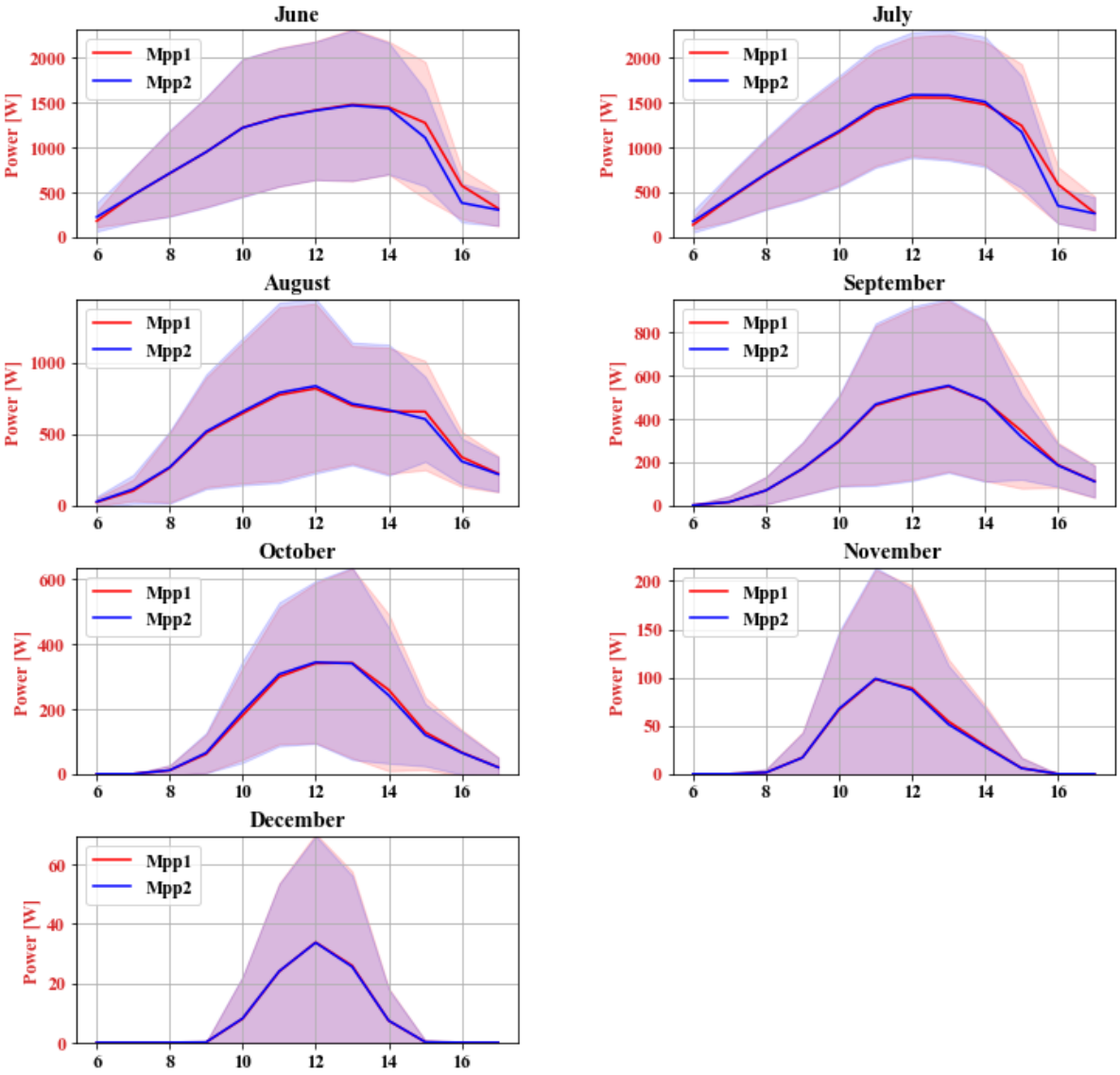

Figure 25: Line plot of both strings and the difference. The plot is produced by averaging the power from each string for every logged hour each day in the given month. The x-axis is hours throughout the day, from 06:00 to 17:00.

To avoid noise due to this difference when comparing the two strings the analysis will focus on a time-period up until this effect. When this effect occurs will vary with the months that are being analyzed. However, the effect is smaller in the fall than during the summer months.

4.2.2 Irradiation

The system was initially not equipped with a reference cell. This was installed 5th February 2019 and was operational from 13th of March 2019. In the analysis of the power production from 01.06.2018 to 31.12.2018, the data for the global horizontal irradiation (GHI) is collected from the Norwegian Meteorological Institute weather and climate database [32].

4.2.2.1 Irradiance from 01.06.2018-31.12.2018

The data is gathered at a weather station in Florida, Bergen, with latitude 60.3837 and longitude 5.331. The data is averaged over the last hour and provided on an hourly basis.

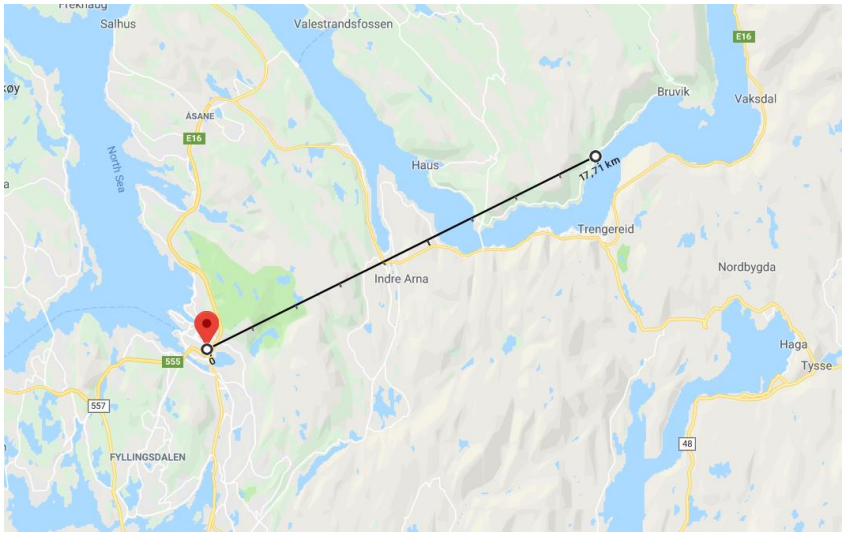

Figure 26: Distance between the weather station and the solar FPV system.

The weather station is located near the city center of Bergen, approximately 17.7 km from the PV facility. Figure 27 presents the irradiation received at this station as average irradiance per day throughout the month.

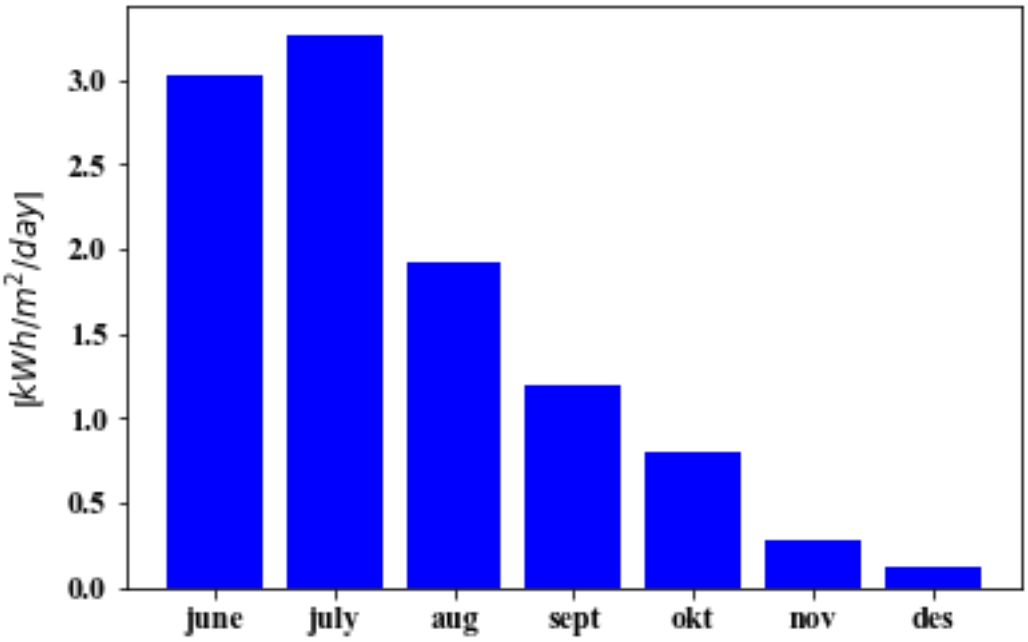

Figure 27: Average irradiation per day received at the weather station in Bergen.

Relative to the measured irradiance, the system at Skaftå will be shaded in the afternoon and get a rapid decrease in power produced. The standard deviation for these values is substantial, which indicates that there is a broad variation in both irradiation and power produced at both locations.

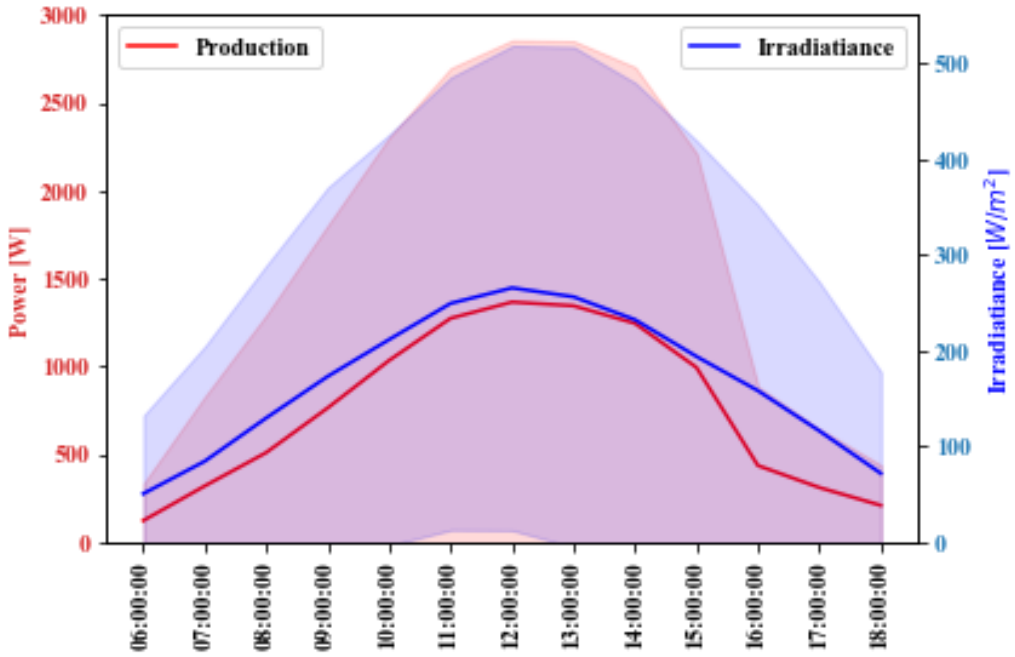

Figure 28: Irradiation and produced power (red) plotted. This is mean values every five minutes in the period from 01.06.2018 to 31.09.2018. The shadowed area is one standard deviation from the mean.

The suns path over the floating PV-system and the measured irradiance will change for six months. This will create a difference in when the shading starts. There was also some difference related to when the peak measured production and peak measured irradiance occur. This is evident in Figure 29, where irradiance and power production are plotted together. Bear in mind that the fluctuations in both registered irradiance and produced power are substantial.

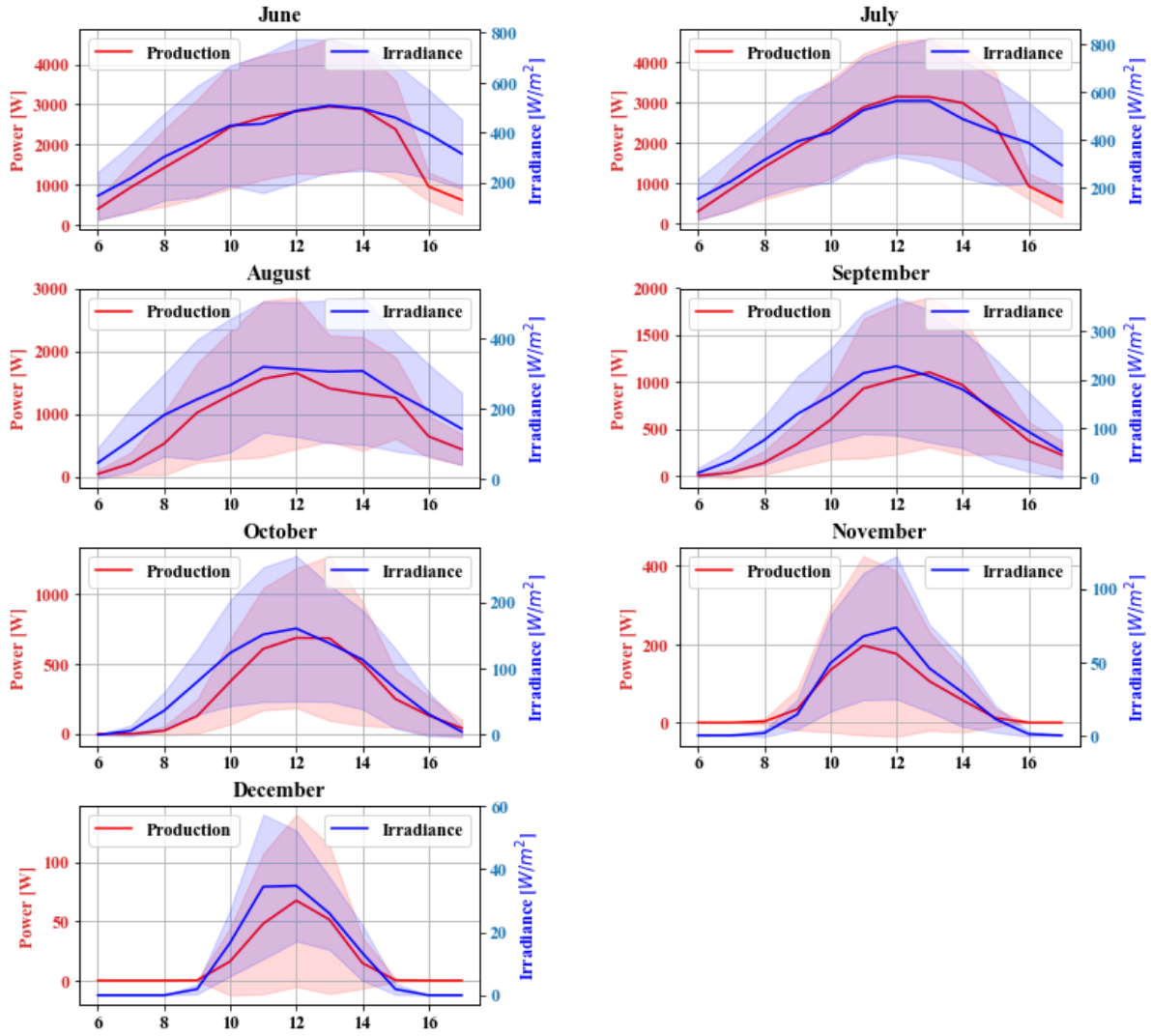

Figure 29: Average irradiance every hour and average power production every hour for each month. The shaded area represents the area in which one standard deviation in both directions resides.

4.3 Instrumentation

The system is logging data for wind speed, water temperature, air temperature, irradiance, and string production. All data is logged with five-minute intervals.

4.3.1 Fronius sensor box

To measure air temperature, water temperature, irradiation, and wind speed, a Fronius sensor box was used. The technical specifications for the sensor box are found at Fronius web page [33].

4.3.1.1 Temperature measurements

To measure the air and water temperature, two PT1000 sensors were used. These sensors have a measuring range from -25 to 75 degrees Celsius, a resolution of 1 degree and accuracy of 0.5 degrees, measured at the sensor box [34].

The air temperature was measured along the edge of the system, just below the sensor for wind speed. The water temperature was also measured at the edge of the system, with the PT1000 sensor hanging down from the side of the system rail approximately 1 meter submerged into the water.

4.3.1.2 Irradiance

Irradiance is measured by the Fronius monocrystalline Si sensor. The z-shaped sensor is placed on the rail approximately two meters from the sensor box. The Fronius sensor box has a channel for the insolation with a 3% accuracy. The irradiation sensor has a tolerance level of $\pm$ 5% of the annual average. All technical information about the reference cell is collected at Fronius web page [35].

Figure 30: Left: The irradiation sensor mounted on the rail. Right: The Fronius sensor box, wind speed instrument and irradiation sensor to the left.

4.3.1.3 Wind speed

The wind speed is measured with a cup anemometer with reed contact. It has a threshold at 2.5 m/s and a resolution of 1 m/s. The tolerance level is $\pm$5% from 5 m/s upwards. The cup anemometer is mounted on a 3-meter rod, approximately 4 meters above the solar cells and

directly above the Fronius sensor box. The sensor is displayed to the right in Figure 30. Technical data for the wind speed sensor is found at Fronius web page [36].

4.3.2 Module back-surface temperature

The temperature sensors for the module back-surface is through a separate system; a resistance temperature detector (RTD) with four channels is used, delivered by Madgetech. The data sheet for this data logger is available in appendix A. The sensors used are PT100 4-wire with a resolution of 0.01 degrees Celsius and accuracy of $\pm$ 0.1 degrees Celsius.

The sensors were mounted on the modules located close to the center of the canvas, as shown in figure 26.

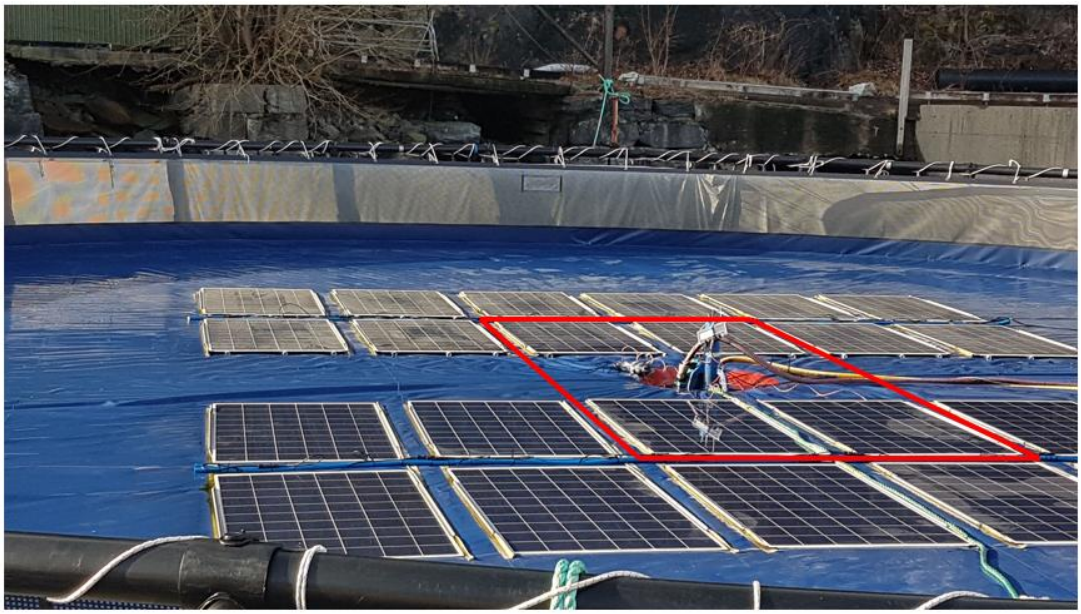

Figure 26: The modules inside the red square has a temperature sensor mounted on the back surface.

More specifically were the sensors mounted on the cells in the second row from the bottom and on one of the two cells in the middle. The sensor mounting was also reinforced with duct tape. On the second visit, the temperature sensors on the modules that were lifted (modules farthest away in the picture) had fallen off. This was attributed due to the movement of the pipes that lifted the modules. A new sensor was mounted on the module to the left of the lifted modules. The pipes on this module were fixed to its position using strips. The initial sensors were mounted 05.02.2019, and the new sensor was mounted 26.02.2019.

4.4 Analysis

All data is analyzed using python, either through Spyder or with Jupyter notebook.

4.4.1 Data and Filtering

4.4.1.1 Initial analysis 01.06.2018-31.12.2018

As described in chapter 3.2.1 and 3.2.2 the initial analysis needs to discriminate for shaded hours. To accurately remove all effects due to shading the data will in the period 01.06.2018 to 31.12.2018 be analyzed from 0800 to 15 for June, July, and August, and 0800 to 1400 for September, October, November, and December. The production data are logged every fifth minute, and the irradiance is collected on an hourly basis. To evaluate the production data with the irradiance the mean power produced every hour is used.

4.4.1.2 Analysis of the strings after setup modifications

The data used to assess the effect of a 32 mm air gap between the canvas and the modules is collected from 14.03.2019 to 19.04.2019. This sample is based on when the sensors started to log and which day the module back-surface temperature is collected. The temperatures of the modules are collected by traveling to the floating PV plant and connecting the logger to a computer which then downloads the data. As the data used in the preliminary analysis, this data also suffers from shading. The effects due to shading primarily affect the analysis in the afternoon, from 15:00-16:00.

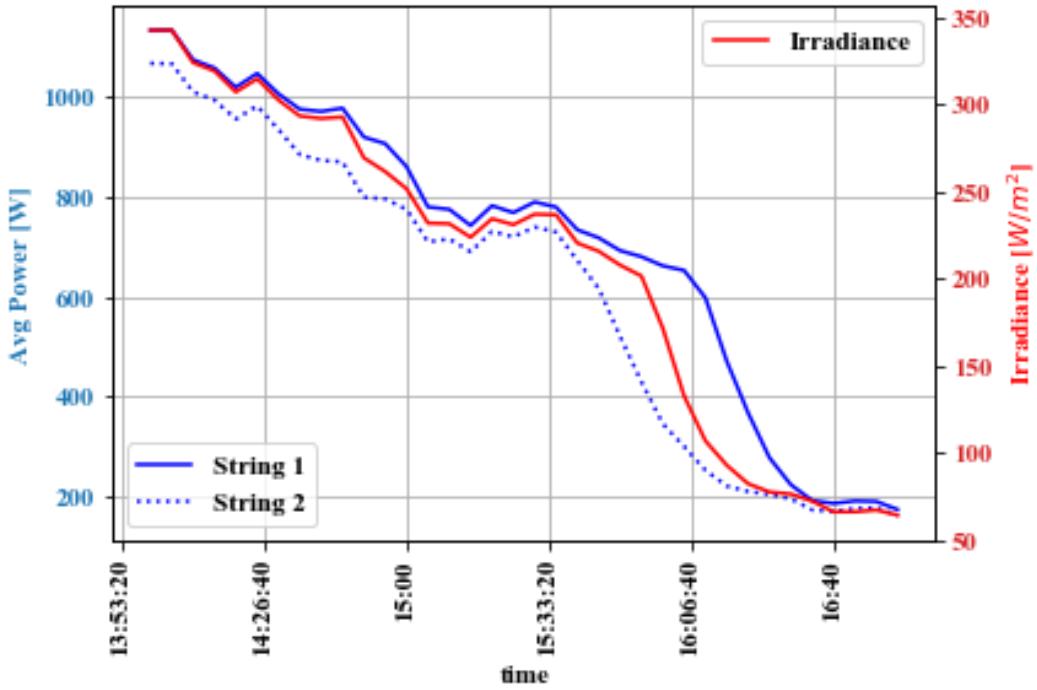

Figure 31: Average power every fifth minute for both strings and irradiance plotted from 1400 to 1655.

As evident in Figure 31, string 2 will be shaded first, at approximately 15:30, then will the reference cell be shaded and string 1 becomes shaded last. To exclude bias in the analysis due to shading, the data will be analyzed from 08:00 to 15:30 unless stated otherwise.

The data is logged every fifth minute for every sensor which is active at the system.

4.5 Model for cell temperature in floating PV

The module or cell temperature is an essential feature in the efficiency of the panel. With a rise in the cell temperature, follows a reduction in the efficiency of the panel. One of the key supportive arguments for floating PV-system opposed to land-based systems is the cooling effect from water, on the cell temperature. This is especially the case for Ocean Sun's technology. A model which can accurately simulate the module or cell temperature will, therefore, be of value in estimating the gain from floating PV in different locations and under different conditions. Three different models are tested, two of which is based on simple fluid dynamic theory and the third is a regression-based model. The regression-based model will also be used to evaluate key drivers in explaining the variance in cell temperature and extrapolate the results to higher irradiance and temperatures.

4.5.1 Simple fluid-dynamic model for a single mass with uniform temperature

In the simple fluid-dynamic model the solar module is treated as a single lump of mass with uniform temperature, T_m. The temperature of the object is affected by the irradiance from the sun, the convective forces from water and air and radiated energy from the object to the sky. The model is a modification and simplification of a model proposed by Martin K. Fuentes in his report from 1987 [37].

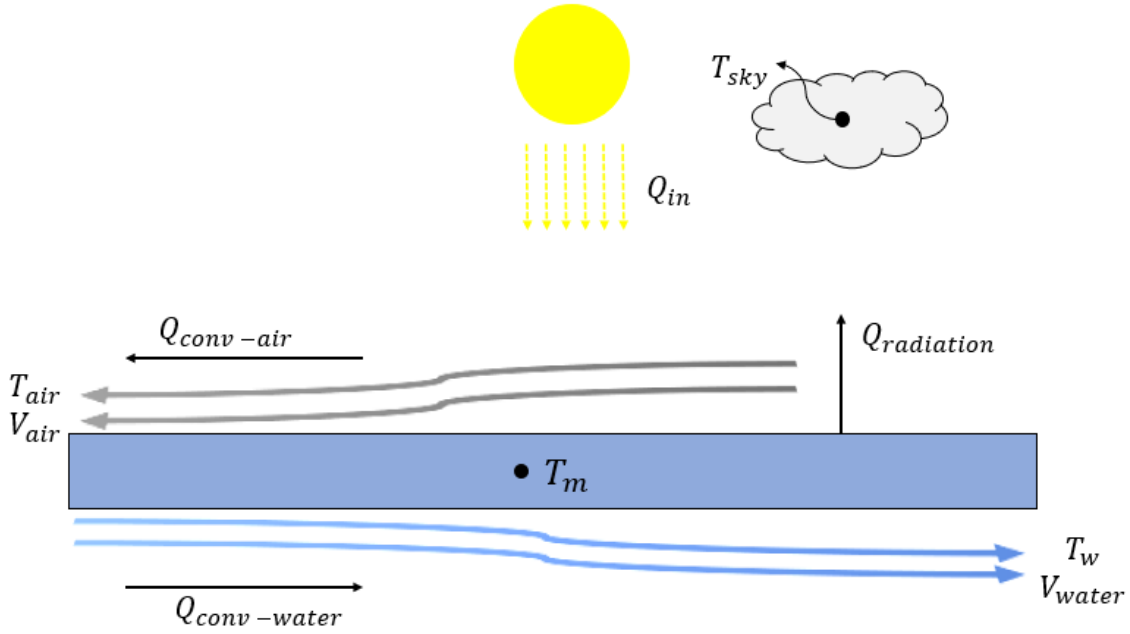

Figure 32: Sketch of the different forces in the fluid-dynamic model. The lumped mass involves both the module and the canvas.

The key parameters for calculating the module temperature are:

- Q_{in}, which is the irradiance from the sun onto the module. This value is used as input in the model.
- η, which is the efficiency of the module.
- T_{air} and T_{water} which is the measured air and water temperature. This is also input to the model.
- V_{air} and V_{water} which is the velocity of the water and air. These parameters are also inputted to the model.

The model is created to simulate the cell temperature over a day, based on the input values. All these values are measured at Skaftå, except the velocity of the water. It is, therefore, necessary to simulate with different velocities.

To get an equation for the module temperature, an energy equation for a control volume is used. For this case the following equation is used:

$$Q_{in}(1-\eta) = (Q_{rad} + Q_{conv-air} + Q_{conv-water}) \tag{38}$$

The left side represents the energy which is not transferred to electricity in the module. This will be calculated as: $Q_{in} = G_m A$. From equation 17 can an expression for the convective process between the solid and the air, and the solid and the water, be derived:

$$Q_{conv-air} = h_{air} A(T_m - T_{air}) \tag{39}$$

$$Q_{conv-water} = h_{water} A(T_m - T_{water}) \tag{40}$$

Where A is the area of the module. h_{air} and h_{water} are the convective heat transfer coefficients for air and water. The contribution to heat transfer through radiation is expressed using equation 31:

$$Q_{rad} = Ae\sigma\left(T_m^4 - T_{sky}^4\right) \tag{41}$$

Where the emissivity for the front glass is 0.84. The contribution from radiative heat exchange can be changed to:

$$Q_{rad} = h_{rad}\left(T_m - T_{sky}\right) \tag{42}$$

Where $h_{rad} = Ae\sigma(T_m^2 + T_{sky}^2)(T_m + T_{sky})$.

This gives a function for T_m derived from equation 36 and the separate equations from each contribution:

$$T_m = \frac{Q_{in}(1-\eta) + h_{water}T_{water} + h_{air}T_{air} + h_{rad}T_{sky}}{h_{water} + h_{air} + h_{rad}} \tag{43}$$

The values for the convection coefficients and the efficiency is dependent on T_m, which means that the equation must be solved iteratively. This is done through a Python script which updates the efficiency and the convection coefficients after each calculation of T_m. This explicit iterative approach gives the following equation:

$$T_m^{t+1} = \frac{(Q_{in}^t(1-\eta^t) + h_{water}^t T_{water}^t + h_{air}^t T_{air}^t + h_{rad}^t T_{sky}^t}{h_{water}^t + h_{rad}^t + h_{air}^t} \quad (44)$$

Where *t* is the timestep. The values for the convection coefficients h_{rad}^t, h_{water}^t and h_{air}^t are calculated with T_m^t. This is a steady-state model, with time-dependent thermal boundary conditions.

The python script is coded as a class which also take the timestep size as an input. This allows for higher resolution than the logged data. Linear interpolations are done to calculate the parameter values at each iteration.

4.5.1.1 Calculation of convection coefficients

To calculate h_{water} and h_{air} the equations in chapter 2.5.2 are used. The fluid properties for air and water are provided for different temperatures. Fluid properties for water is also provided at different salinities, but ten percent is used in all simulations in this thesis. The salinity will differ over the year but can be approximated to ten percent close to the surface [38]. The fluid properties used for air and water are kinematic viscosity, Prandtl's number, thermal conductivity, and thermal expansion coefficient. The fluid properties are evaluated at atmospheric pressure and at the temperature that coincides with the measured temperature for air and water at every time step.

The model will interpolate with respect to the temperature to find the correct values for the fluid property. This is done at each iteration. The properties are evaluated at their film-temperature which is the reference temperature for the fluid properties and is defined as the arithmetic mean between the surface temperature and the adjacent fluid or gas temperature. The film-temperature are used to ensure that the correlations for forced and natural convection holds. The fluid properties for air are collected, while all the properties for water are collected at MIT's library for thermophysical properties for seawater [39-41].

The convection profile is evaluated for both air and water. In the case of mixed natural and forced convection, equation 35 is used, and the value of n is chosen as 7/2. This is a value chosen as it should yield a good approximation for transverse flow and horizontal plates [42].

4.5.1.2 Other parameters

The temperature of the sky is calculated with equation [7]:

$$T_{sky} = 0.0552 T_{air}^{\frac{3}{2}} \quad (45)$$

This is an estimation that holds best for clear sky days, and not so good for cloudy days.

The efficiency will not be constant throughout the day and must, therefore, be updated at each iteration in response to changes in module temperature. Equation 15 is used to update the module efficiency at each iteration. From the datasheet of the module the values for η_{Tref} and β_{ref} are collected. These are:

$$\eta_{ref} = 0.164$$

$$\beta_{ref} = \frac{0.41}{100}[1\backslash K]$$

4.5.2 Simple fluid-dynamic model for layered geometry with different temperatures

In contrast to the simple model with uniform temperature across a single mass, this model will provide an iterative approach to model the cell temperature with all the layers considered. This model is an extension of the model used by Lereng I. H [43]. The geometrical setup and the involved heat transfer are displayed below.

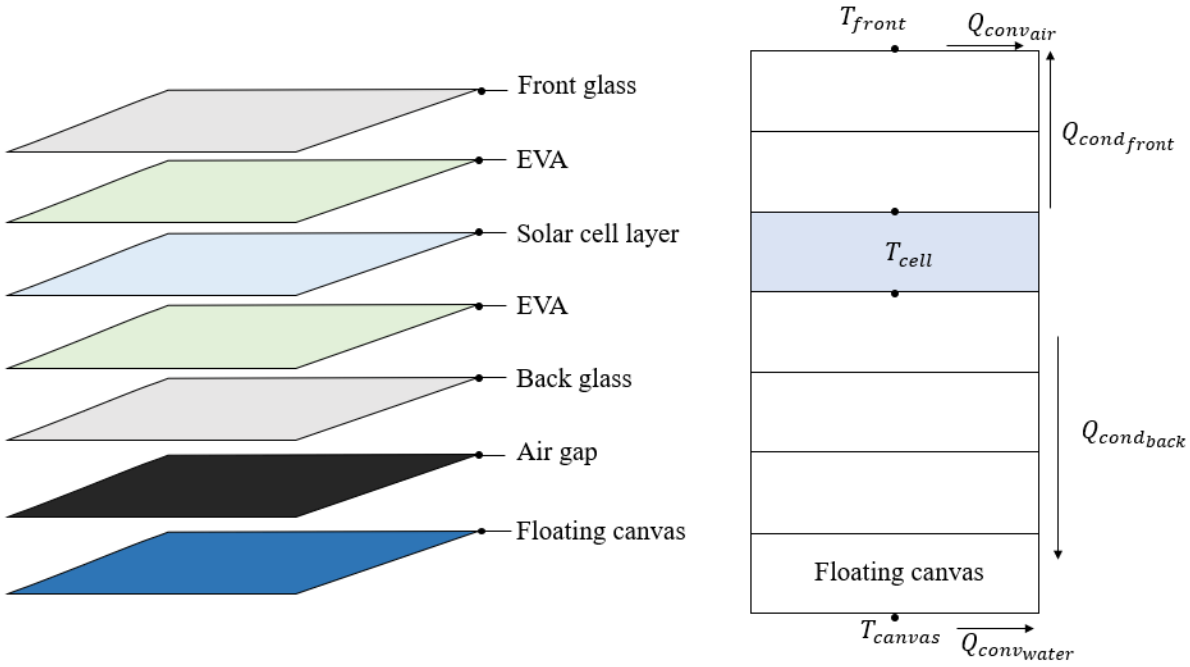

Figure 33: The geometry, heat transfer processes and layers included in this model.

The module receives heat through solar irradiance. The heat is generated in the band-gap in the solar cell layer. The heat will then be transferred by conduction in two parallel processes, up towards the top and down towards the water. This gives rise to the equation:

$$Q_{in}(1-\eta)A = \frac{T_{cell} - T_{air}}{R_{front}} + \frac{T_{cell} - T_{water}}{R_{back}} \tag{46}$$

R_{front} is the front thermal resistance, R_{back} is the back thermal resistance, T_c is the solar cell temperature, Q_{in} is the solar irradiance horizontal onto the module, η is the conversion efficiency, and A is the surface area.

Both the front and back resistance is calculated as series resistances with the formulas:

$$R_{back} = \frac{\Delta x_{eva}}{k_{EVA}A} + \frac{\Delta x_{glass}}{k_{glass}A} + \frac{\Delta x_{air}}{k_{air}A} + \frac{\Delta x_{canvas}}{k_{canvas}A} + \frac{1}{h_{waterA}} \tag{47}$$

$$R_{front} = \frac{\Delta x_{eva}}{k_{EVA}A} + \frac{\Delta x_{glass}}{k_{glass}A} + \frac{1}{h_{airA}} \tag{48}$$

Where Δx is the thickness of the layer, k is the thermal conductivity of the material and h is the convection coefficient. Solving equation 46 for the cell temperature gives the equation:

$$T_{cell} = \frac{(Q_{in}(1-\eta) \times A \times R_{back}R_{front} + T_{air}R_{back} + T_{water}R_{front})}{R_{front} + R_{back}} \quad (49)$$

This, as with the previous model, is a steady-state model, with time-dependent thermal boundary layers. To accurately calculate T_{cell}, η, R_{back} and R_{front} must be updated every timestep according to the calculated cell temperature. Equation 49 must, therefore, be solved iteratively and T_{cell}^{t+1} is approximated by:

$$T_{cell}^{t+1} = \frac{Q_{in}^{t}(1-\eta^{t}) \times A \times R_{back}^{t}R_{front}^{t} + T_{air}^{t}R_{back}^{t} + T_{water}^{t}R_{front}^{t}}{R_{front}^{t} + R_{back}^{t}} \quad (50)$$

The model is scripted in python and adapted to be able to set the step size for Δt. To calculate the measured parameters outside the data points are linear interpolation used. Heat transfer due to radiation is omitted in this model because of the difficulties of estimating the surface temperature of the glass front and because of the relatively small contribution it makes on the total heat transfer.

To be able to compare the iterated cell temperatures to the measured back-surface module temperatures, equation 16 is used with a ΔT of 1, which are the best estimate for a glass-glass module with an enclosed backside [20].

4.5.2.1 Calculation of convection coefficients

The convection coefficients are reliant on the surface temperature of the object to be calculated. It is, however, possible to make assumptions on the coefficient based on temperature differences between the surface and the adjacent fluid and the velocity of the fluid.

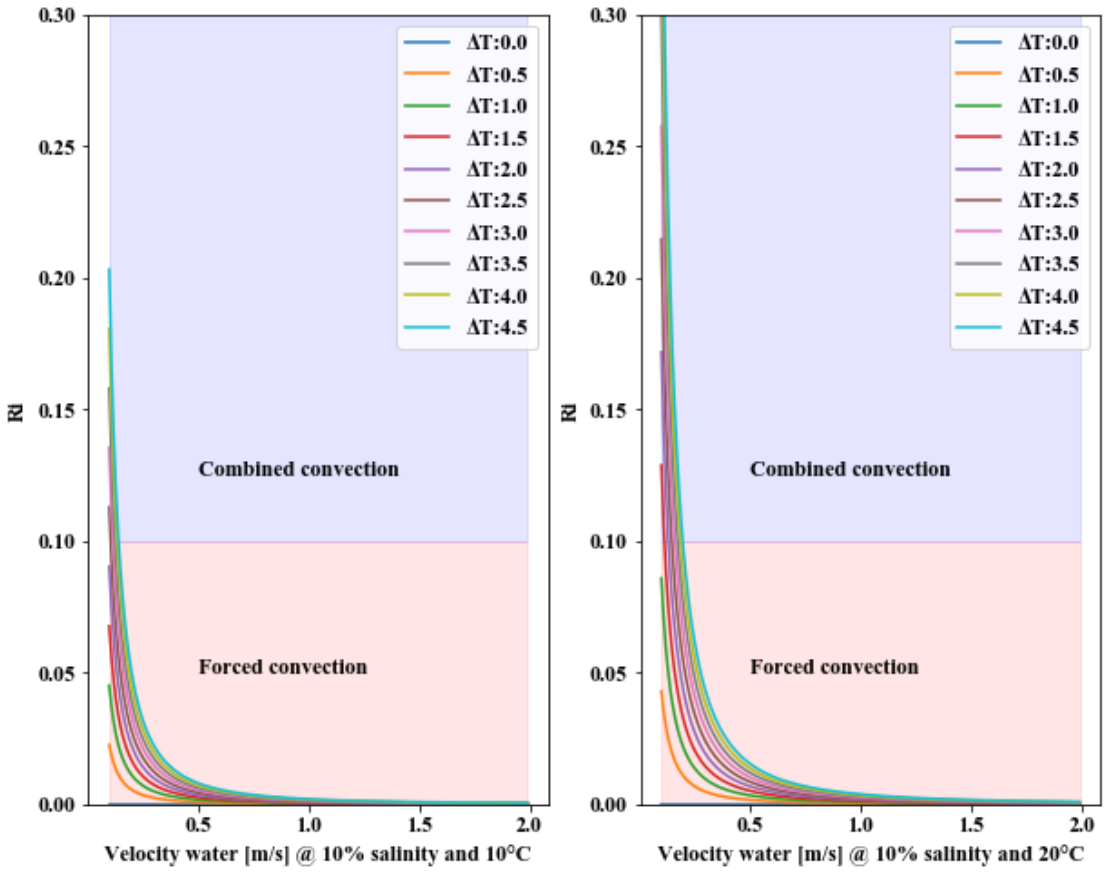

Figure 34: Ri value for different velocities and temperature differences. The Ri is evaluated at 10% salinity and 20℃

Figure 34 indicates that a forced convection profile is present even at low velocities. This is also the case for air, as can be seen below.

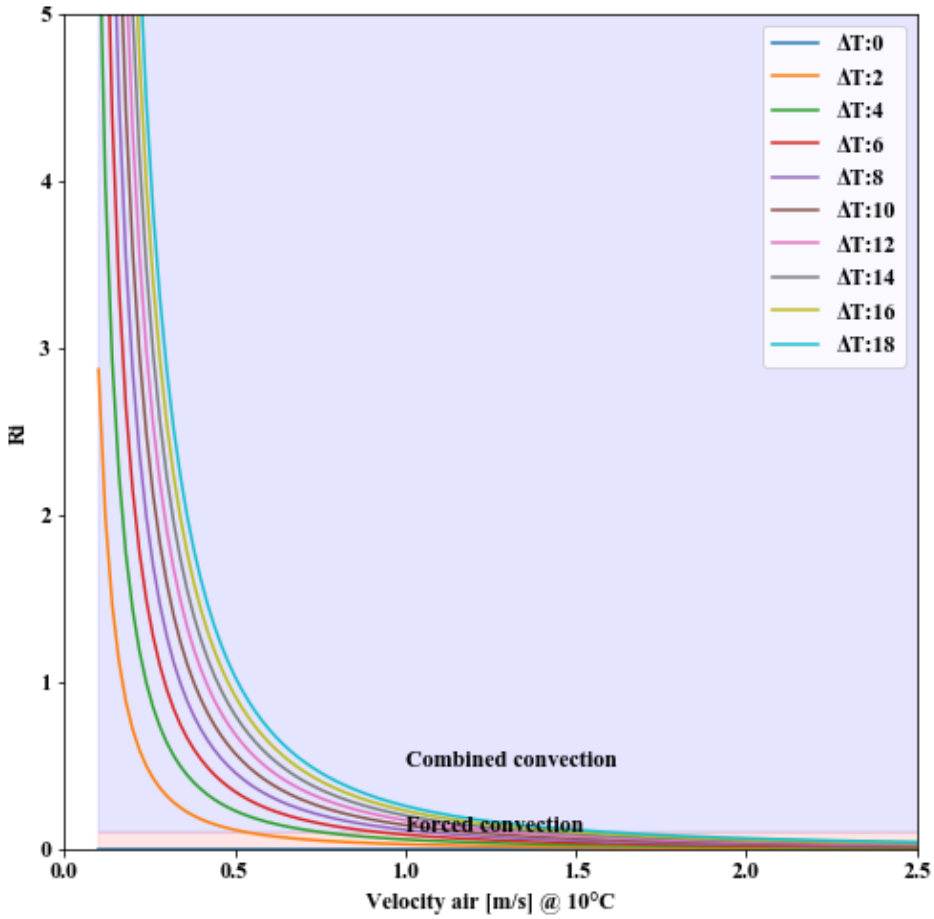

Figure 35: Ri-profile for air at different velocities and temperature differences. The beige shaded area is are for forced convection.

When evaluating the convection coefficient, it is evident that the temperature difference only matters for small velocities. This can be seen in the figures below. These figures are used to approximate the convection coefficient for both air and water at different velocities.

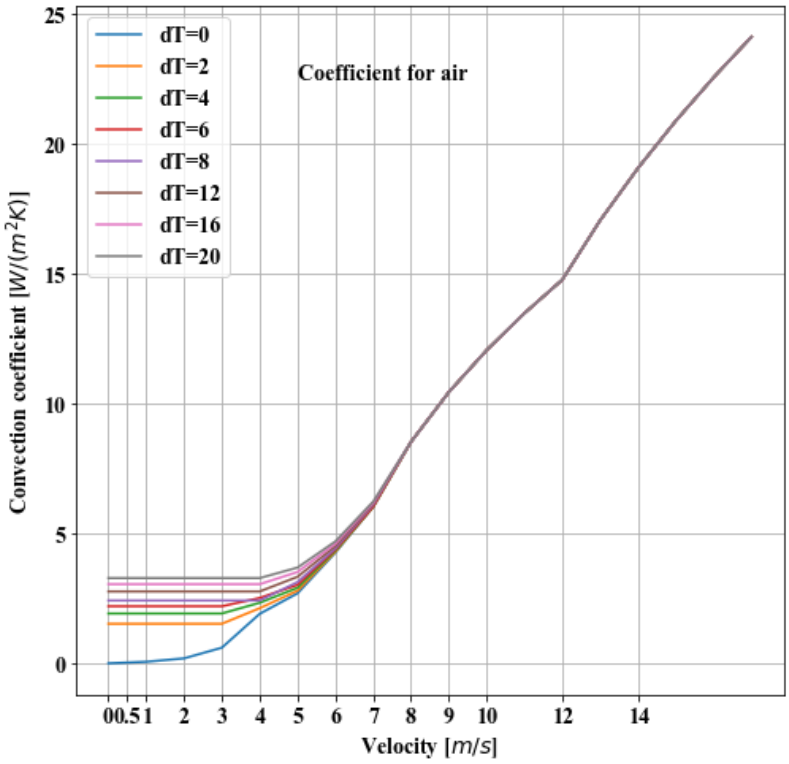

Figure 36: Convection coefficient for air at different temperature differences between the object surface and the adjacent liquid and different velocities.

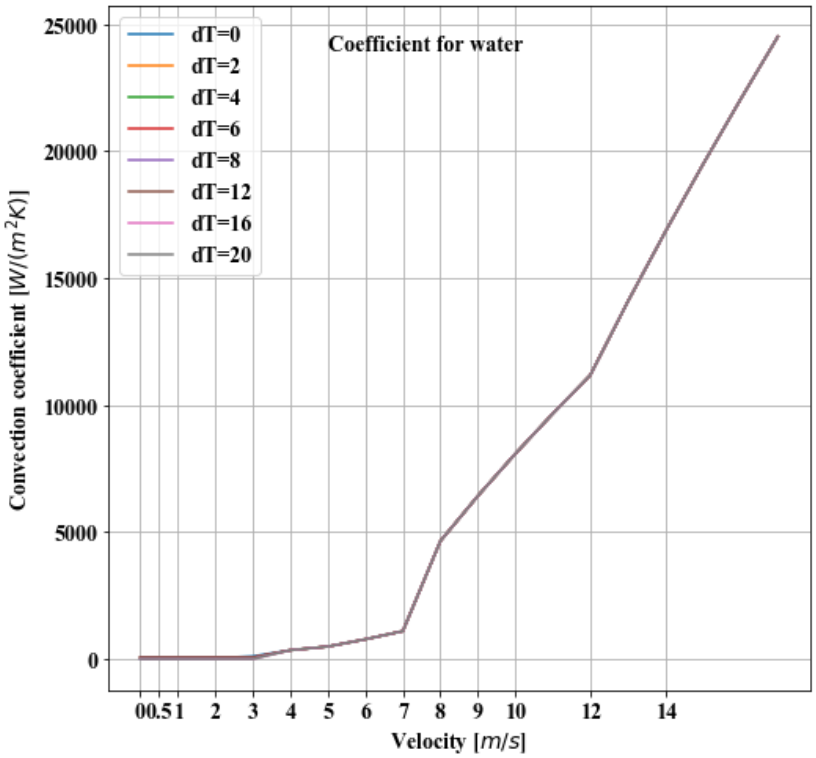

Figure 37: Convection coefficient for air at different temperature differences between the object surface and the adjacent liquid and different velocities.

4.5.3 Multiple linear regression and ridge regression

Kamuyu, Lim, Won, and Ahn have in their article used linear regression to predict the module temperature for a floating PV-system [44]. The model used in this thesis will be based on the same methodology. The goal of the multiple linear regression is to model the relationship between two or more features and a continuous target variable. The linear model is given as [45]:

$$\boldsymbol{y} = X\boldsymbol{\beta} + \boldsymbol{\epsilon} \tag{51}$$

Where $\boldsymbol{y}$ is the observation vector, X is the design matrix, $\boldsymbol{\beta}$ is the parameter vector, and $\boldsymbol{\epsilon}$ is the residual vector.

In this model, the explanatory variables used are irradiance, water temperature, air temperature, and wind speed. These are all parameters that are measured at the location. This gives a design matrix comprised of four features:

$$X = \begin{bmatrix} 1 & Q_{inn_1} & T_{water_1} & T_{air_1} & V_{wind_1} \\ \vdots & \vdots & \vdots & \vdots & \vdots \\ 1 & Q_{inn_m} & T_{water_m} & T_{air_m} & V_{wind_m} \end{bmatrix} \tag{52}$$

moreover, a parameter vectoris given as:

$$\boldsymbol{\beta} = \begin{bmatrix} \boldsymbol{\beta_1} \\ \vdots \\ \boldsymbol{\beta_m} \end{bmatrix} \tag{53}$$

The standard least-squares minimization is used to determine the parameters, which is based on minimizing the sum of squares of residuals, $SS_{R\epsilon}$ [44]:

$$SS_{R\epsilon} = \sum_{i=1}^{n} \epsilon_i^2 \tag{54}$$

Where $\epsilon_i = (y_i - \overline{y_i})$, is the difference between the real target value (y_i) and the predicted target value ($\overline{y_i}$).

Least square regression can be sensitive to collinearity between features. A set of points is collinear if they are lying on a single line. Ridge regression, on the other hand, is more robust. Ridge regression is a method that involves shrinkage of the regressions coefficients by imposing a penalty on their size [46]. Ridge regression uses L2 regularization. L2

regularization reduces the complexity of a model by penalizing large individual weights [47]. This involves adding a penalty term, given as the λ times the square of the magnitude of the coefficients. The strength of the penalty term is controlled by a tuning parameter, λ. When $\lambda = 0$ will ridge regression be equal to least square regression.

The ridge regression is implemented through the built-in python package, sci-kit-learn. The feature space is normalized before it is used to train a model. To tune the penalty term another built-in function is used, *GridsearchCV [48]*. *GridsearchCV* will search for the best possible solution with the pre-determined tuning parameters and validate the results by cross-validation. Cross-validation involves splitting the training data into *k* smaller sets and then train the model using *k-1* of the data as training data. The model is then validated on the remaining part of the data. This is done *k* times so that each subset is tested. The score of the cross-validation is the average of all the scores from each fold.

Ridge regression model is trained and tested by fitting the data while omitting one day and then testing on that day. This is done for every day. The primary motivation behind the regression model in this thesis is to compare the predicational power of a regression method on module temperature compared to other models and to evaluate the key drivers for the module temperature on a floating PV-plant.

To evaluate the results, the mean absolute error (MAE) score metric is used. In the Scikit-learn-package it is this defined as [49]:

$$MAE = \frac{1}{n_{samples}} \sum_{i=0}^{n_{samples}-1} \left| y_i - y_{pred_i} \right| \tag{55}$$

Where y_i is the observed back-surface module temperatures and y_{pred_i} is the predicted back-surface module temperatures.

The R^2 is also used to evaluate the result of univariate linear regression. R^2 indicate the amount of variation in the target variable that is explained by the feature.

4.6 Comparing the tilted system with floating PV at Skaftå

To assess the gain from a floating PV-system one cannot only compare it to modules with zero tilt. By tilting the modules, it is possible to increase the in-plane irradiance. Based on the theory described in chapter 2.4.2, an analysis has been done. The built-in package *pvlib* has

been used to calculate the in-plane irradiance based on the global horizontal irradiance at Skaftå. The albedo for the area was set to a default value of 0.25, and a south-faced system was assumed.

The analysis has been done with different tilt options and explores the "break-even" efficiency in which the tilted system will provide the same power output as the floating PV-system. The comparisons are being made based on "mock" strings with 12 modules each, at the same location as the floating system only tilted with a predetermined angle. The needed "break-even" efficiencies can then be evaluated to see if they are realistic for land-based PV-system. The "break-even" efficiencies are calculated with the equation:

$$\eta_{breakeven} = \frac{P_{AC}}{G_m A} \tag{56}$$

Where, G_m is the irradiance in the plane of the array, A is the surface area and P_{AC} is the measured produced electricity. The analysis is based on that the tilted system has the same surface area as the floating PV system used in this thesis.

5 Results and discussion

In the first part of this chapter, the results gathered from the analysis of the floating PV-system in the period 01.06.2018 to 31.12.2019 will be presented. This part will mainly try to estimate the performance of the system in that period and if there are any differences between the strings. To do this the system PR and efficiency are presented along with differences in production.

The second part of the results will focus on what effect an air gap of 32 mm will have on the performance of a string. This is done by analyzing the data from a period where one string is modified by being lifted with 32 mm PP-pipes. Performance of both strings and power production will be presented. The results will be evaluated along with the back-surface module temperatures.

The third part of this thesis is based on the models for estimating the back-surface module temperature. Simple fluid-dynamic models to simulate the back-surface temperature through a day is tested and a ridge regression prediction model is used. These will also be used to extrapolate the results for higher irradiance.

Lastly, a short comparison between floating PV and tilted options in the same location are done.

5.1 Initial analysis of the PV-system

This section includes the results from the analysis of the plant in the period 01.06.2018 to 31.12.2018. The values for efficiency and PR provided is on a system level, which includes all system losses.

5.1.1 Instantaneous observations

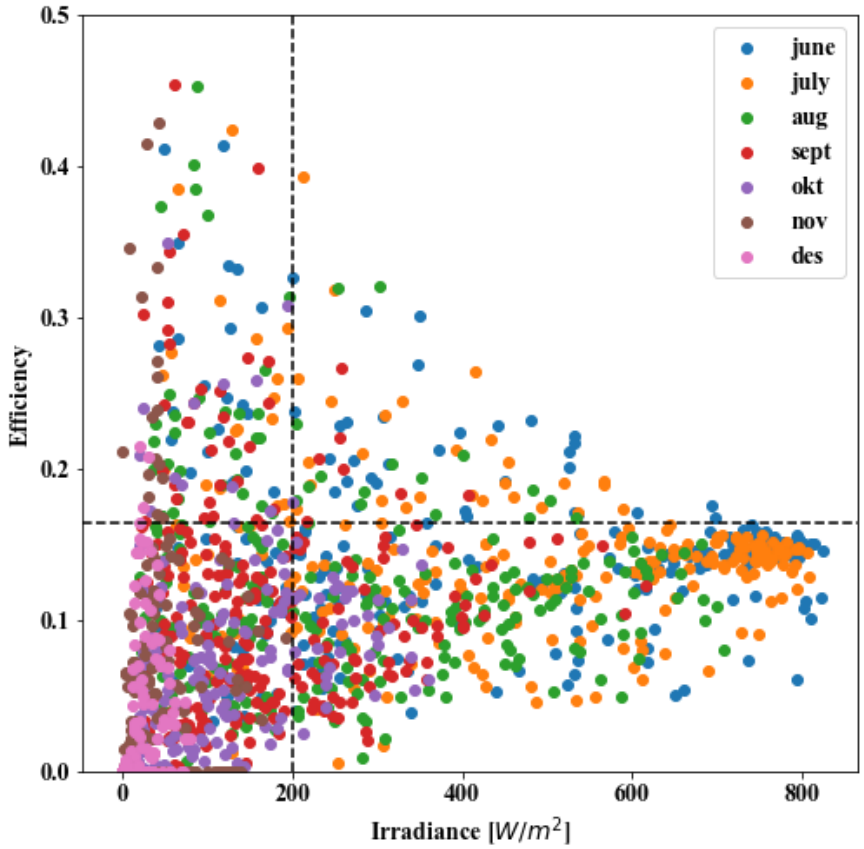

Figure 38: Scatter plot of hourly observations on system efficiency for the entire period color coded by month. The interval used is from 08:00 to 14:00. The dotted horizontal black line is the rated efficiency of the modules. At this time there were no irradiance measurements locally at Skaftå, and irradiance measurements from Bergen were used in the calculations.

The mark for 200 W/m^2 in Figure 38 is there to indicate which observations can be trusted in evaluating the performance of the system. It is evident from the figure that observations that were done in December, November, October and to some extent September lacks robustness. The scatter plot also indicates that the validity of the efficiency calculations done in August can be questioned. The observations these periods are characterized by low voltages and possible discrepancies between the weather condition at Bergen and Skaftå.

The efficiency converges to a point below the rated efficiency for the modules of 16.4% for the months with high irradiance. The stability of the curve at higher irradiance is also in line with the efficiency curve of the inverter which is more stable if it operates close to its rated power output.

To combat the outliers from differences in cloudiness, a box plot is created. This illustrates most observations while at the same time presents the density of outliers in each month.

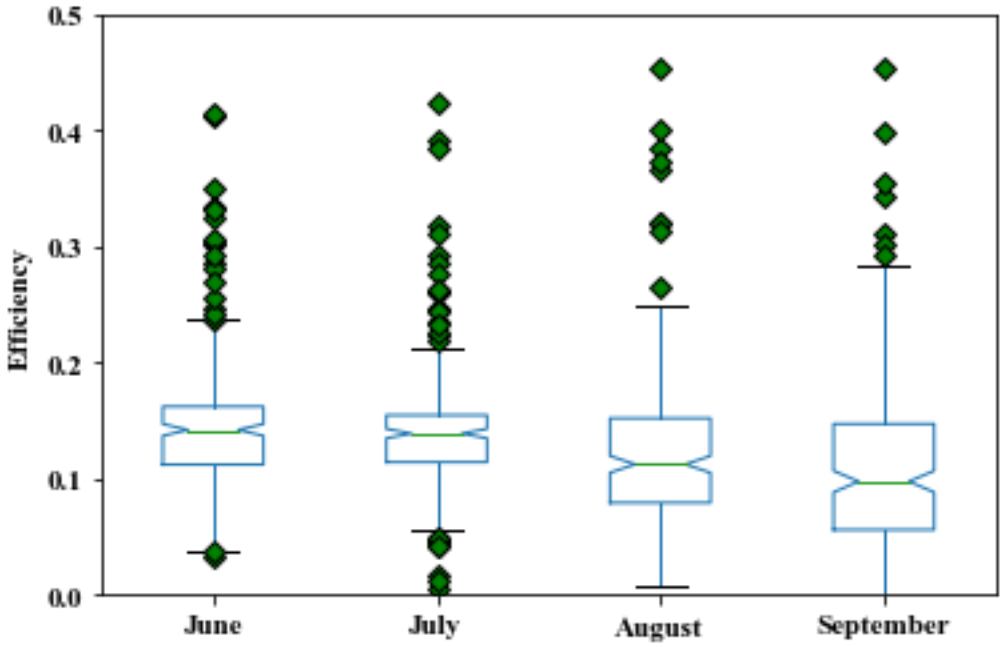

Figure 39: Boxplot of the distribution of efficiencies for the months with the most insolation.

The boxplot presents the distribution of efficiencies in each month. The green line is the median of observations, and the end of the boxplots represents the median of the upper half (Q_3) and the lower half portion (Q_1) of the observations. The wings at each end are given as $Q_3 \pm (Q_3 - Q_1) \times 1.5$. Observations outside of this range are considered outliers. The months of October, November, and December are omitted in the box plot, due to low irradiation and large spread among observations.

The notches in the box plots are created to illustrate the 95 percent confidence intervals of observations. This indicates that the median of observations for June and July does not, within a 95 percent confidence interval, differ.

5.1.2 Daily performance evaluation

To increase the robustness of the observations on efficiency and PR, the metrics can be evaluated on daily irradiation and registered energy generated at the floating PV-plant. The daily observations of efficiency and performance ratio are given in Figure 40.

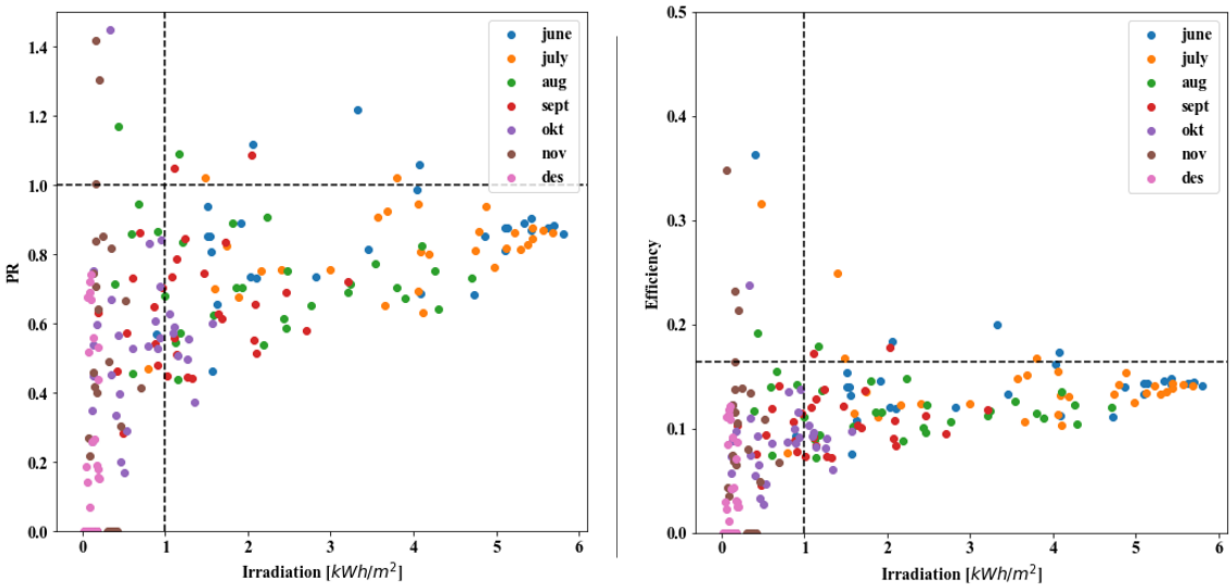

Figure 40: Left: Daily PR-values plotted against irradiation. Right: Daily efficiency plotted against irradiation. The black dotted horizontal line is the rated efficiency of the modules and PR equal to one.

Figure 40 displays a scatterplot with a less random distribution of observations than seen on instantaneous observations. This allows for more trustworthy observations.

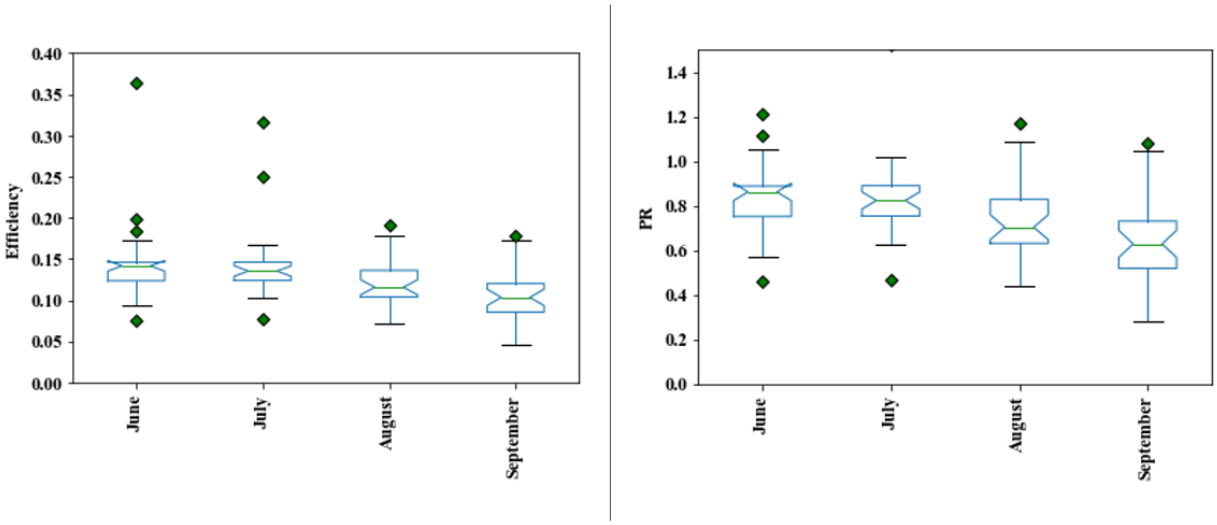

Figure 41: Box plot for efficiency (left) and PR (right). This is calculated with daily observations.

As explained for the scatter plot, an assessment of daily performance gives observations with a narrower distribution. This is evident in the box plots in Figure 41, with a smaller box length and fewer outliers. Furthermore, June and July have median scores on PR and efficiency close to 15 percent.

5.1.3 Monthly performance evaluation

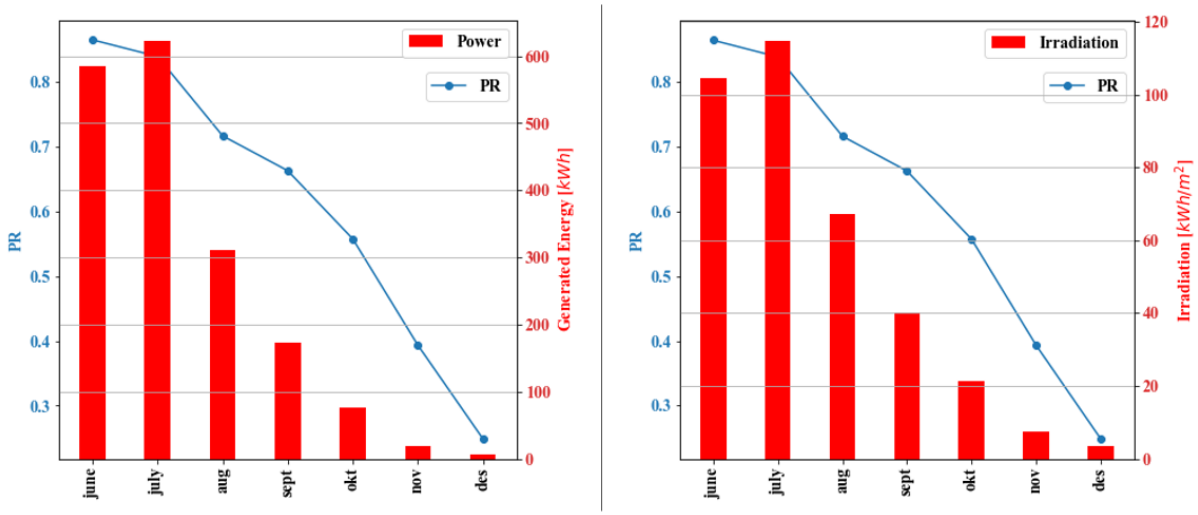

Figure 42: Monthly observations of efficiency (left) and PR (right) plotted with global horizontal insolation.

The values in Figure 42 are given in Table 2. The efficiency and PR are evaluated based on total accumulated energy delivered by the system and accumulated energy received by the system.

Table 2: List of values that are graphed in the figure above.

	EFFICIENCY	**PR**	**IRRADIATION** $[kWh/m^2]$
JUNE	0.142	0.86	104.50
JULY	0.138	0.84	114.70
AUGUST	0.117	0.72	67.21
SEPTEMBER	0.109	0.66	40.19
OCTOBER	0.091	0.56	21.34
NOVEMBER	0.065	0.393	7.50
DECEMBER	0.041	0.249	3.41

The PR for June on 86.0% and 84.2% for July indicates that the system does perform well, given that the metrics are system based. The PR includes all the losses present in the system and indicates that 86% of the installed capacity is utilized for June.

As displayed, the performance of the system is reduced with a reduction in irradiance. This is in line with the efficiency curve of the modules and the inverter. At low irradiance will the inverter also operate outside the MPPT interval, which will affect the performance.

Moreover, the discrepancies between the weather conditions at Bergen and Skaftå can affect the result for the entire period. The measurement of irradiance is, as mentioned, approximately seventeen kilometers away from the floating PV-system. The area is also very diverse, with a lot of valleys and steep mountains. As a result, local weather conditions and cloudiness can be different.

5.2 Initial analysis of the strings

To assess the change between the strings after the set-up has been manipulated, it is important to know the initial performance of each string and possible differences between them.

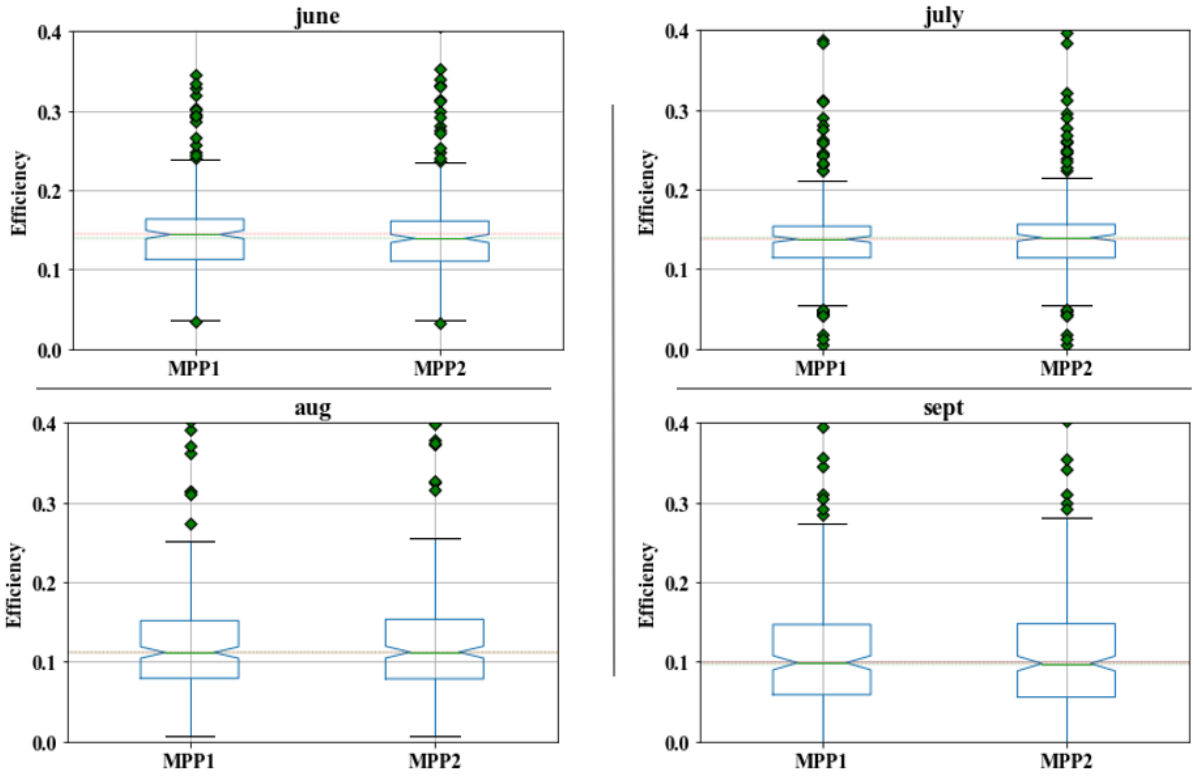

Figure 43: Box plot of the distribution of efficiencies for the four months with the most insolation. The faded red and green lines are the median of the distributions.

Figure 43 displays the efficiency distribution and the median for each string, in the given months. The notches are, as mentioned, the values in the 95 percent confidence interval of the median efficiency. As displayed with the faded lines, one cannot within a 95%-confidence interval say that the strings differ from each other.

The calculated monthly values for efficiency and PR for each string is presented in Table 3 with the difference in percentage.

Table 3: Overview of the calculated performance for both strings and the difference in percentage. The data is analyzed from 08:00-14:30 uniformly for every month.

	EFFICIENCY		**PR**			**ENERGY [KWH]**	
	String1	String2	String1	String2	Differences [%]	MPP1	MPP2
JUNE	0.143	0.140	0.873	0.856	1.99	258.57	257.13
JULY	0.137	0.138	0.835	0.842	-0.850	273.78	278.83
AUGUST	0.117	0.117	0.713	0.714	-0.663	138.41	140.72
SEPTEMBER	0.108	0.109	0.663	0.662	0.152	80.52	80.18
OCTOBER	0.090	0.092	0.551	0.563	-2.06	47.04	46.91
NOVEMBER	0.065	0.064	0.395	0.391	1.000	9.98	9.85
DECEMBER	0.041	0.041	0.249	0.248	0.228	2.64	2.63

The cumulative production from string 1 is 810.96 kWh and 816.26 kWh from string 2. String 2 has produced 0.65 % more than string 1 in the period analyzed. Despite a difference in cumulative production, it is problematic to assume a difference between the strings. Fronius reports of a $\pm$ 5% uncertainty in the power measurements. The uncertainty renders it challenging to attribute the difference in the strings to differences in performance and not just measurement errors.

The difference can be clarified by IV-measurements directly on the strings. This was attempted on three different occasions. At the first two dates, the irradiance was too low to yield accurate results. The third attempt was done 24.04.2019. The results from the measurement are given in the table below.

Table 4: Results from IV-measurements done on both strings.

MEASUREMENT	TIME	IRRADIANCE [W/m^2]	MODULE TEMPERATURE [C]	STRING	P_{STC}
1	10:34	464	13.1	1	3070
2	10:37	458	14.7	1	3200
3	10:38	465	14.7	1	3177
4	10:39	466	14.7	1	3165
		AVERAGE			3153.00
5	10:45	459	21.5	2	3160
6	10:46	469	21.5	2	3100
7	10:47	469	21.5	2	3117
8	10:48	469	21.5	2	3124
		AVERAGE			3125.25

This gives a difference of 0.88 % between the strings. These measures were done under an irradiance which was deemed too low by the apparatus and therefore included some uncertainty. The measures are also done after the modules on one of the strings were lifted.

As seen throughout this chapter will the analysis show that there is a small difference between the strings. String 1 seems to produce 0.5% - 0.9 % more electricity than string 2, and it is likely due to a difference in the actual capacity of the modules in the two strings. However, the results are very uncertain, and the difference is small, but it could contribute both ways when the strings are compared.

5.3 Results after modifying the system set up

5.3.1 Power production and Irradiance

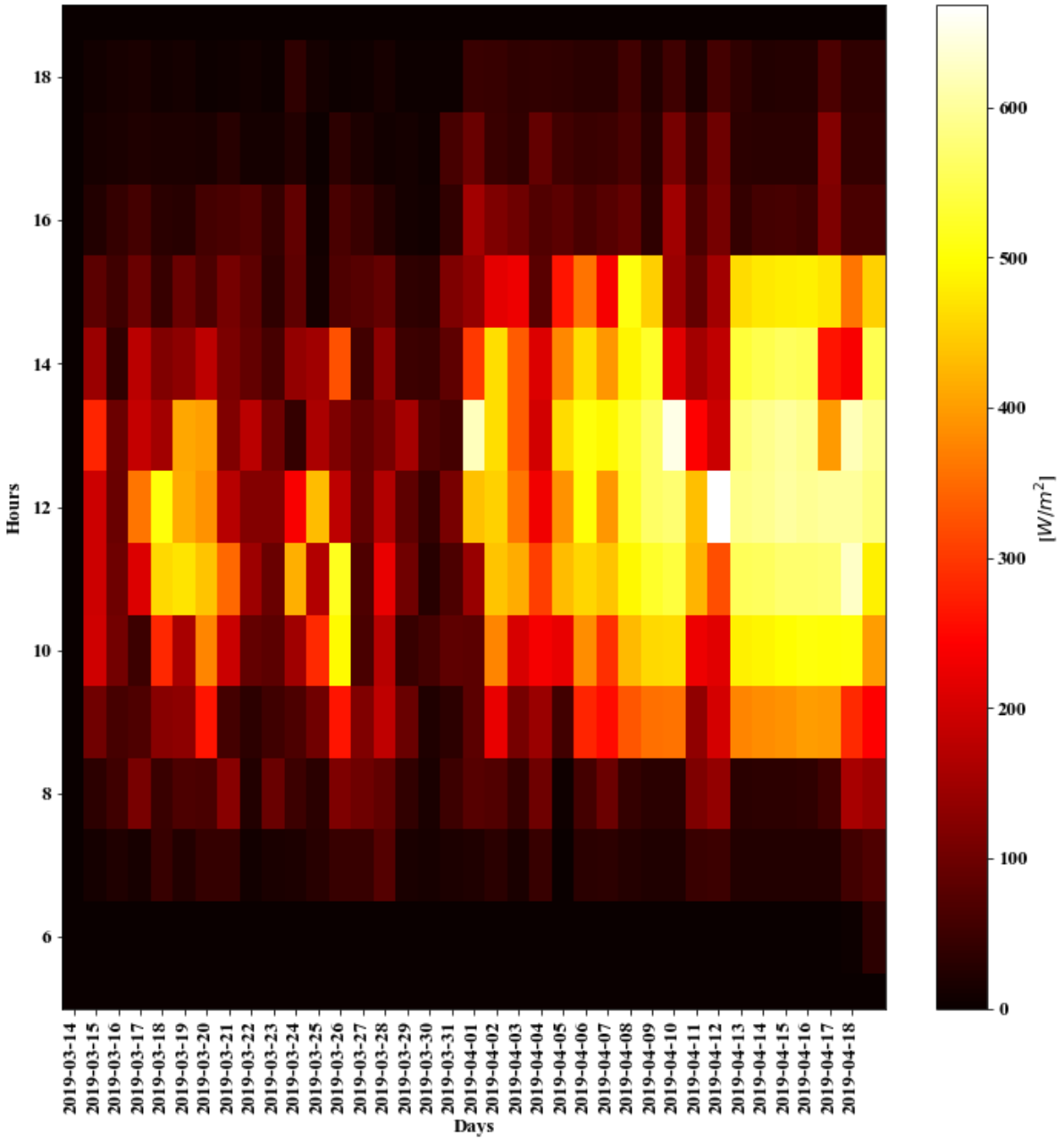

Figure 44: Heat map of irradiance measured by the on-site pyranometer. Data is sampled from 0600 to 1800.

Figure 44 presents the amount of irradiance received at the reference cell at the site. It is evident that the last days in the period had high irradiance, compared to the earlier days. It is also evident that at the there is an abrupt decline in irradiance just before 1530, due to shading.

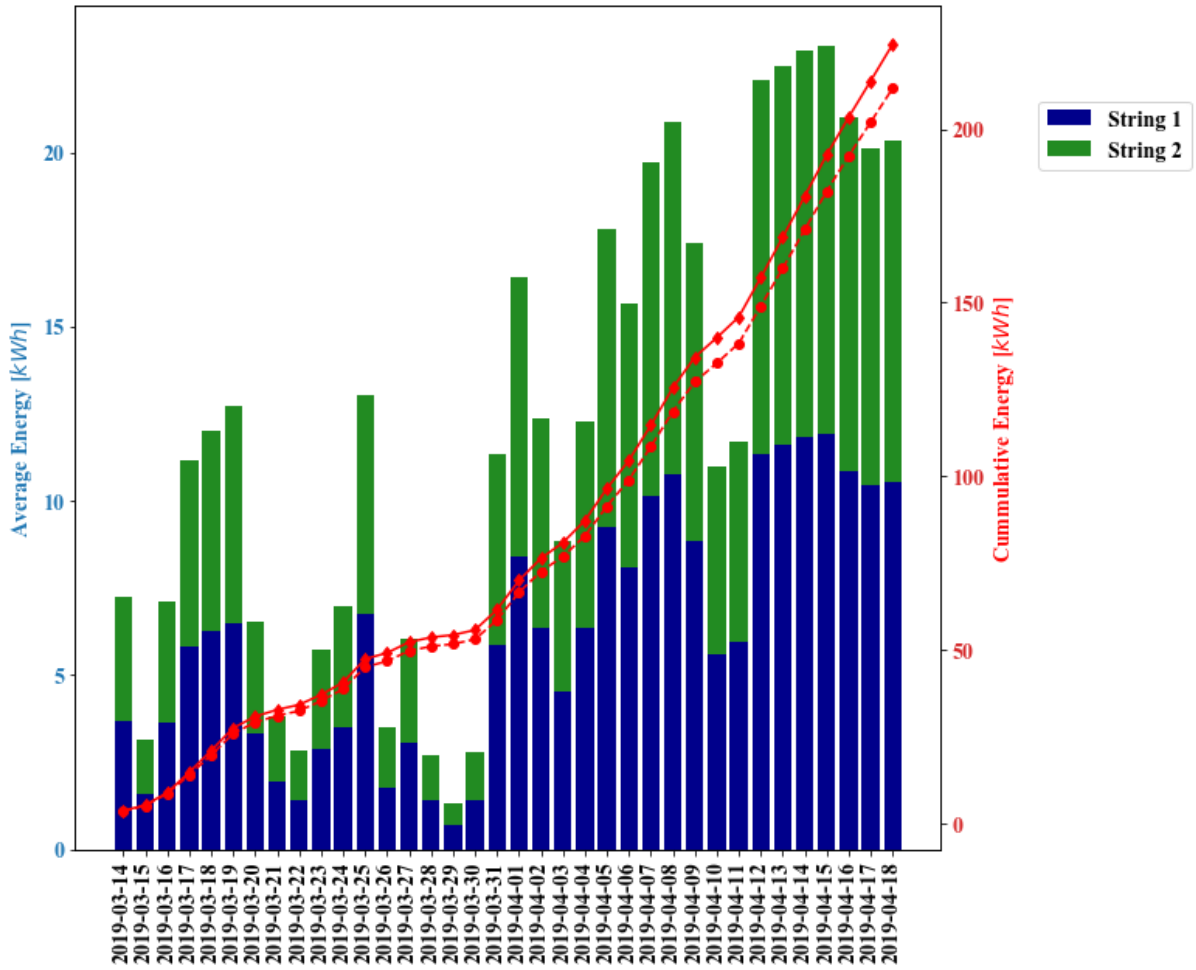

Figure 45: Average energy plotted as bars for each string and cumulative energy in the period. String 1 is in direct contact with the canvas. String 2 has an air gap of 32 mm.

Figure 45 displays the energy produced from each string and the accumulated energy throughout the period. Throughout the period string 1 has produced 11.09 kWh more than string 2, which has an air gap between the module and canvas. This is a difference of 5.24%. This is approximately one month of data, with relatively low irradiance. The effect of the cooling is expected to increase with higher module temperature resulting from higher irradiance and ambient temperature. Still, a difference of 5.24% percent in accumulated energy is already significant and can make a substantial difference for large-scale power plants assessed over a year.

From Figure 46 where a straight line is fitted to the data points of string production against irradiance, the straight line predicts an increasing relative difference between string production with increasing irradiance. The regression models shown in Figure 46 has slopes $\beta_1 = 3.4$ and $\beta_2 = 3.2$ and regression scores of $R_1^2 = 0.994$ and $R_2^2 = 0.995$ when scored on normalized datapoints.

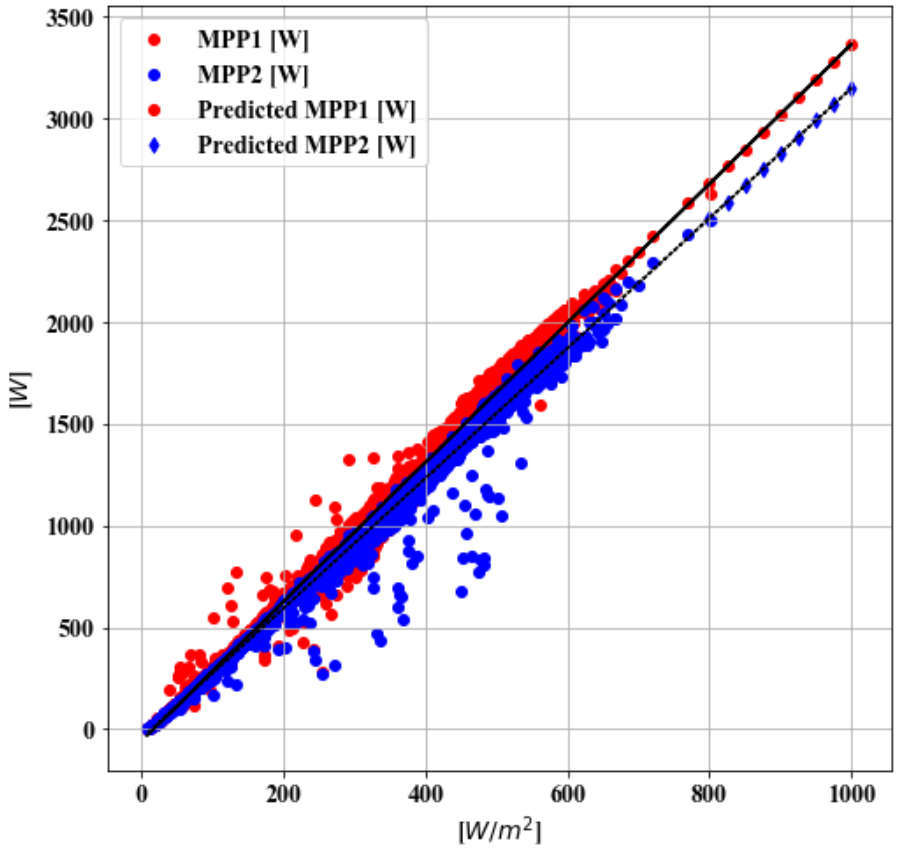

Figure 46: Power production from string 1 (red) and 2 (blue) plotted against irradiance, with predicted values for irradiance in the range of 750-1250 W/m^2.

The extrapolated power production from each string is provided for 800 W/m^2 and 1000 W/m^2 in Table 5. Keep in mind that the theoretical maximum of the string is 3240 W.

Table 5: Results for higher irradiance extrapolated from the OLS model.

IRRADIANCE $[W/m^2]$	**MPP1** $[W]$	**MPP2** $[W]$	**DIFFERENCE** $[W]$	**DIFFERENCE** $[\%]$
800	2680.05	2510.65	169.4	5.8%
1000	3346.50	3164.04	182.46	6.6%

The results from Table 5 indicates that the benefits of thermal contact with water will be larger if the floating PV-plant is in a place where irradiance is higher.

5.3.2 Performance metrics

5.3.2.1 Instantaneous scores

Figure 47 shows the system efficiency with a resolution of 5 min. For each data point, the corresponding measured module temperature is visualized with a color bar. The air-cooled string experience higher module temperatures than the water-cooled string. This can be seen

by many markers with brighter colors. The color bar for both plots is equal, with the same color interval. This allows for direct comparisons between the observations. The plotted efficiencies are system efficiencies and include the losses in the entire system. The main reason why the system efficiency is, in fact, comparable to the rated module efficiency is the temperature of the modules which is generally below the STC condition of 25 degrees.

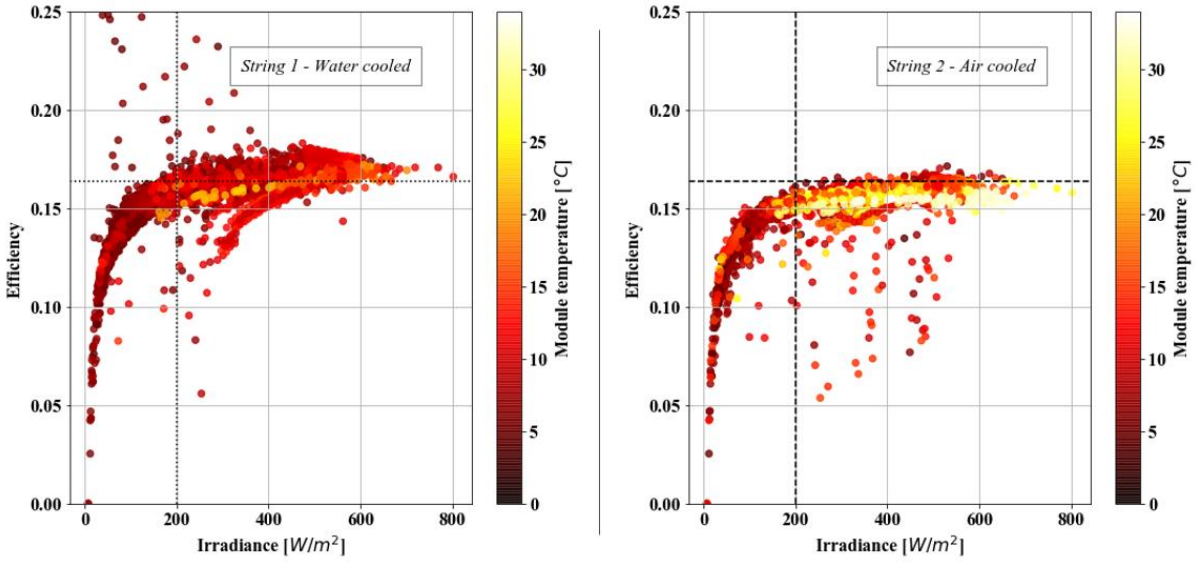

Figure 47: Scatter plot of instantaneous efficiencies against irradiation color-coded by module temperature. The horizontal dotted line is the rated efficiency of the modules and the vertical dotted line is the 200 W/m^2 limit to indicate the start of stable measurements.

The efficiencies plotted for both string 1 and string 2 shows few outliers after the 200 W/m^2 mark, which can be confirmed by the box plot in Figure 48. It is evident that the observations done under low irradiation creates some outliers, but a narrow box with tight fins reflects the robustness of the observations. Nonetheless, the median is below the rated efficiency for both strings, but substantially higher for the water-cooled string, string 1.

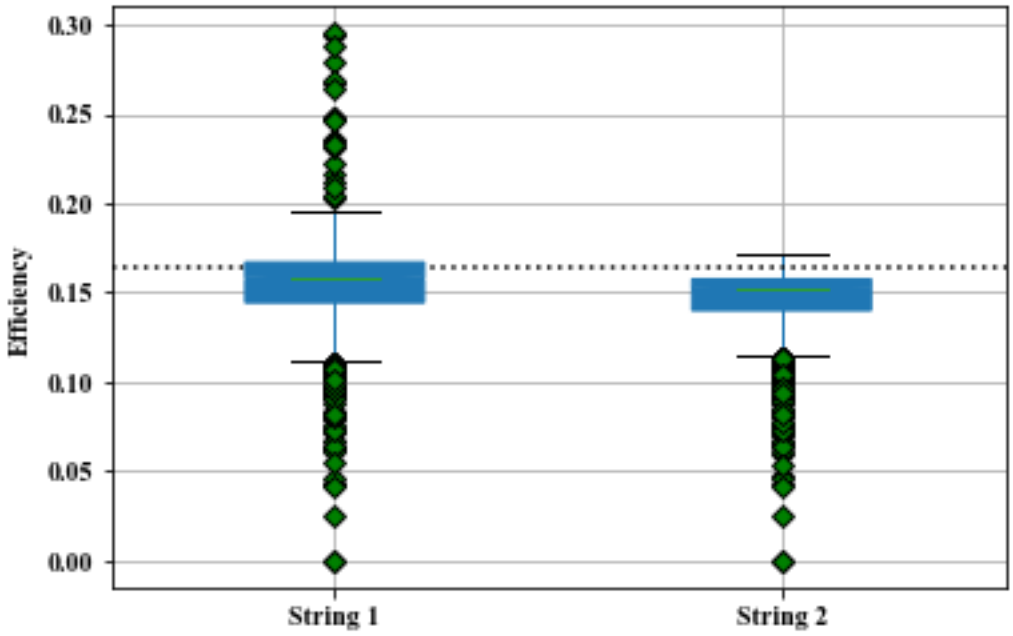

Figure 48: Box plot of efficiency of each string. Green markers are given as outliers. The green line in the middle of the box plot is the median observation.

If the efficiencies are evaluated at different intervals of irradiance, it is possible to evaluate and compare the strings under specific intervals of irradiance.

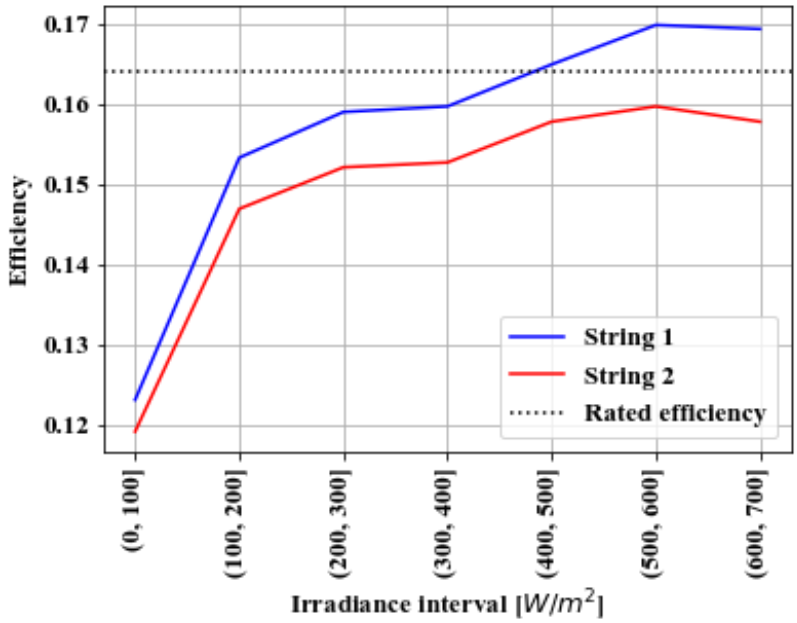

Figure 49: Efficiency for both strings plotted as mean in specific intervals of irradiance of 100 W/m2.

As evident, string 1 will perform better than string 2 with an increasing relative difference in efficiency.

5.3.2.2 Daily PR

To reduce the noise in the analysis it is possible to evaluate the strings based on daily generated energy for each string, and for the whole period, as done previously.

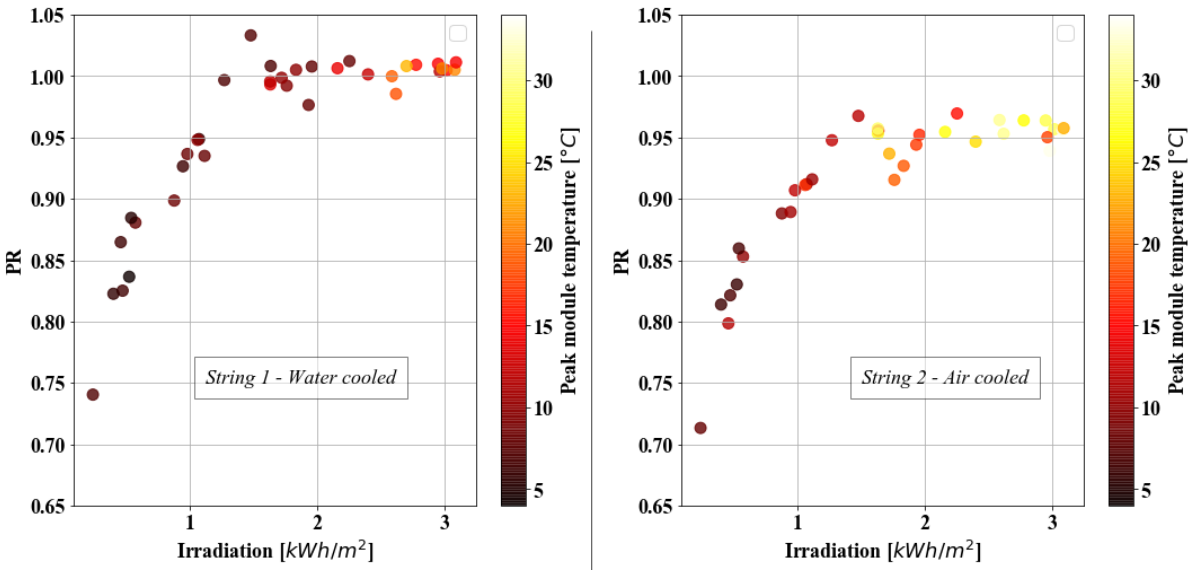

Figure 50: Performance ratio calculated for each day, along with irradiation and peak back-surface module temperature that day.

The PR stabilizes around 0.95 for the air-cooled string and around 1.00 for the water-cooled string. The observations are color-coded after the peak temperature of the day. It is evident that the water-cooled string is more robust against large temperature increases during the day than the air-cooled string. The air-cooled string experiences peak temperature around thirty degrees Celsius. The efficiencies also take the form of the efficiency curves of solar cells. This is depicted with low efficiencies under low irradiance, and a stabilization of the curve after about 200 W/m^2.

The median, mean and standard deviation of the plotted measures are presented in the table below.

Table 6: Median, the mean and standard deviation for both strings on measures of PR and efficiency.

	STRING 1: WATER-COOLED		**STRING 2: AIR-COOLED**	
	Efficiency (η)	PR	Efficiency (η)	PR
MEDIAN	0.163	0.996	0.155	0.945
MEAN	0.157	0.959	0.150	0.916
STANDARD DEVIATION	0.011	0.070	0.01	0.059

The results are also provided in the box plot below, with an indication of the distribution and outliers. When daily observations are plotted a lot of the outliers connected to low irradiation will disappear, this is clear from the box plots in Figure 51.

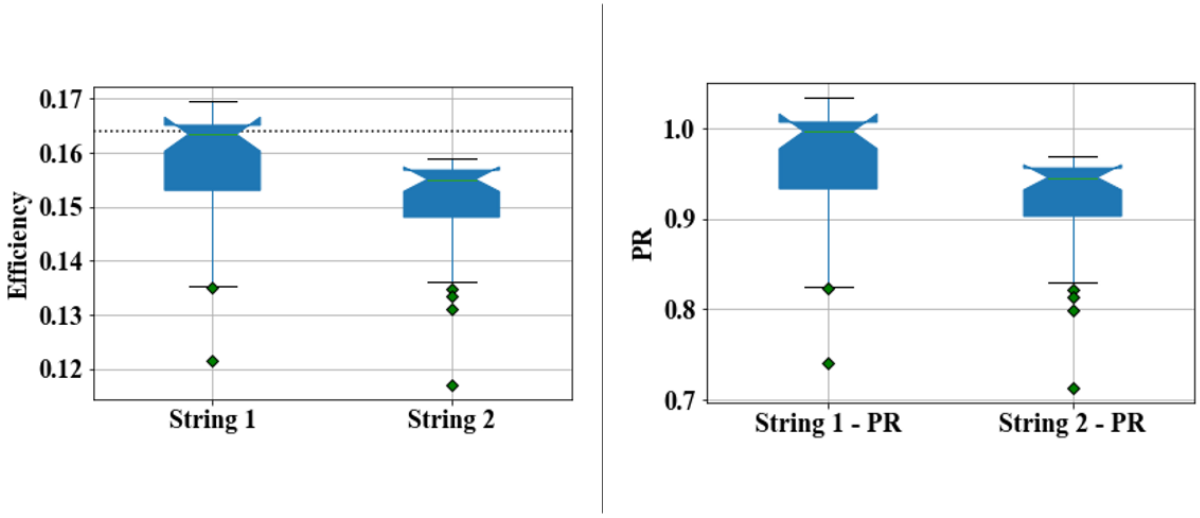

Figure 51: Box plot of efficiency and PR for with daily observations.

It is evident from previous figures that the system performs better at higher radiation. This is also evident in Figure 52 where a drop in irradiation is accompanied by a drop in performance of both strings. There are measurements of PR that is to some extent out of the ordinary, with large PR-values under mediocre irradiation. For example, is March 31st the day with the highest registered PR-value. The box plots in Figure 51 also shows that the median in the upper part of the observations falls within the 95% confidence interval. This means that there are larger differences in the observations in the lower quartile than the upper. Hence, fewer outliers above the median.

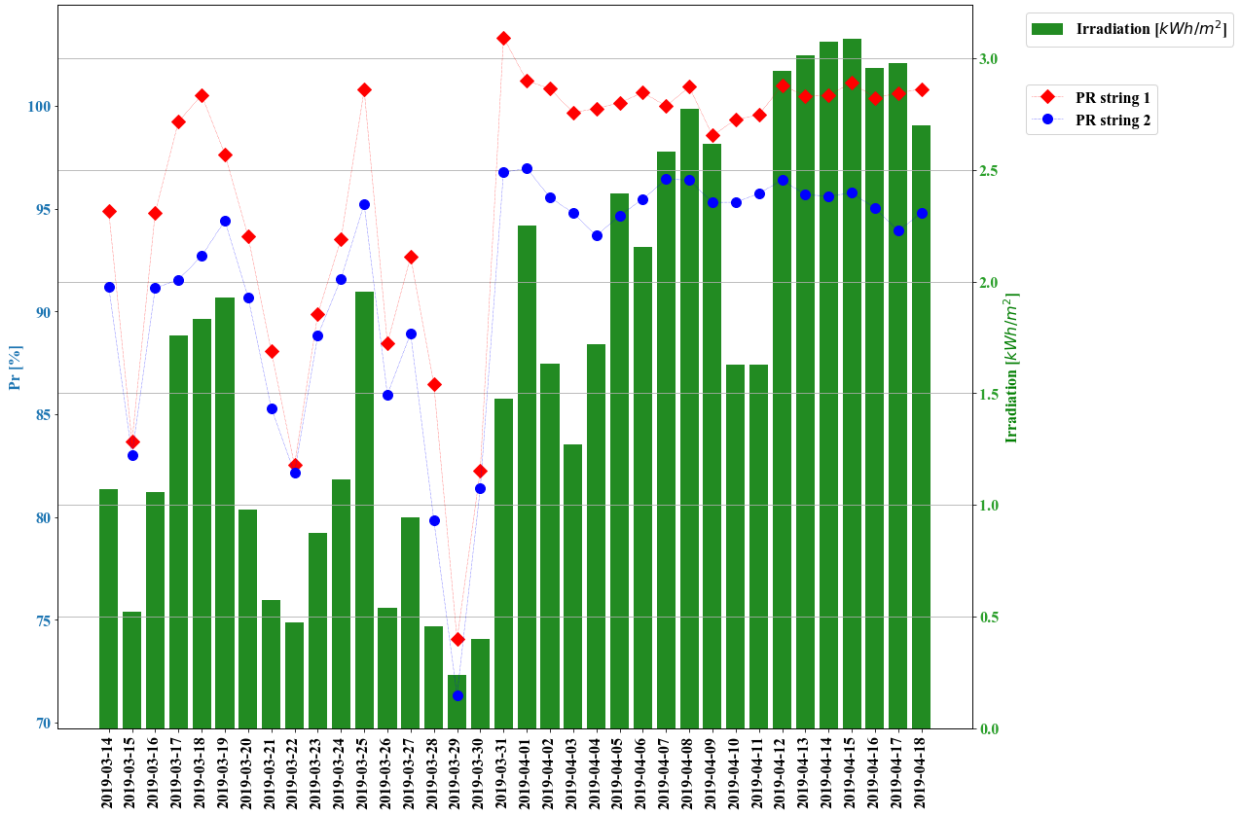

Figure 52: Performance ratio displayed with irradiation for the same day and the peak module temperature.

The performance of the system over the entire period is presented in the table below.

Table 7: Performance over the entire period.

	EFFICIENCY (η)	**PR**	**ENERGY [KWH]**
STRING 1	0.162	0.989	217.32
STRING 2	0.154	0.938	206.23
DIFFERENCE [%]	5.24	5.24	5.24

This is very high PR, for both strings, even in a Nordic context, indicating that the net system losses are small and that the cooling effect is favorable. PR values for new systems typically range from 0.6-0.9 [50, 51], depending on the climatic conditions among other things.

String 1, which is water cooled, does consistently outperform string 2. Aggregated over the entire period will string 1 perform 5.24% better than string 2. String 1 will also outperform string 2 consistently throughout the day. As can be seen in Figure 53, where from approximately 08:00 string 1 performs better.

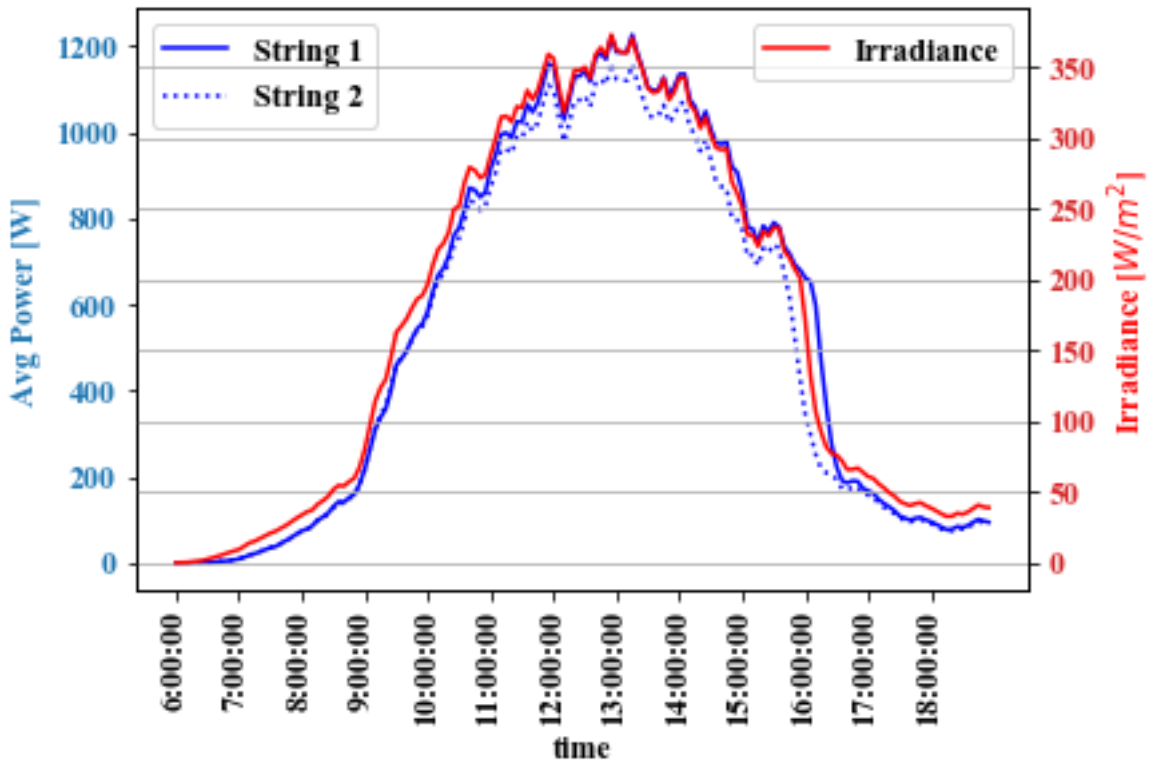

Figure 53: Average power production from each string every fifth minute the entire period, plotted with a line plot for irradiance. The results are valid for up until 13:30, where the plant starts being shaded.

The analysis has so far included data points in which irradiance is below 200 W/m^2. Based on the assumption that the relative difference increase with increasing irradiance, will we expect a larger difference when shading and irradiance below 200 W/m^2 is removed.

When removing these data points the difference between string 1 and string 2 increase to 5.48%. This is an increase of 4.47% from the difference of 5.24% when data with low irradiance was included.

5.3.3 Differences in temperature

The average temperature every fifth minute for the entire period is plotted below, Figure 54.

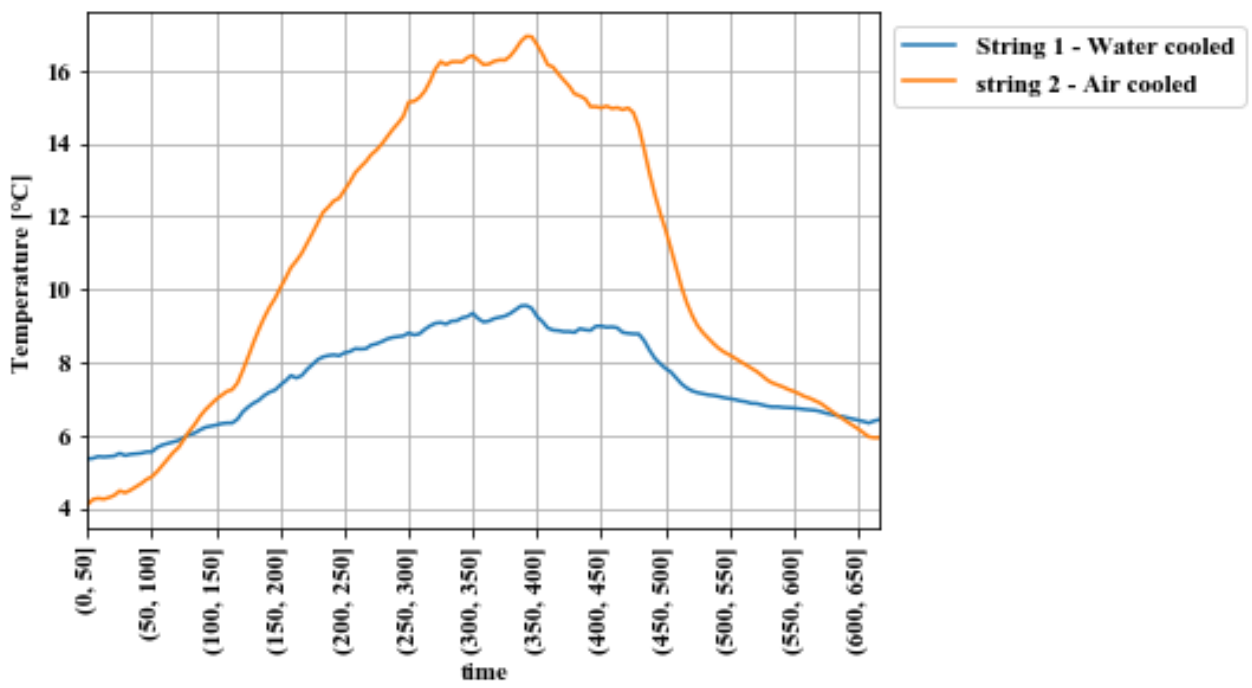

Figure 54: Average back-surface module temperature on each string.

The temperatures are, as expected, larger in the middle of the day. This is due to the higher irradiance. It is also evident that the temperature difference is larger in the middle of the day, under high irradiance. The temperature of the water-cooled module is largely restricted by the water temperature and fluctuates less than the module temperature of the air-cooled string, string 2. The water temperature is stable during the period and only fluctuates between a maximum of nine degrees and a minimum of 5 degrees.

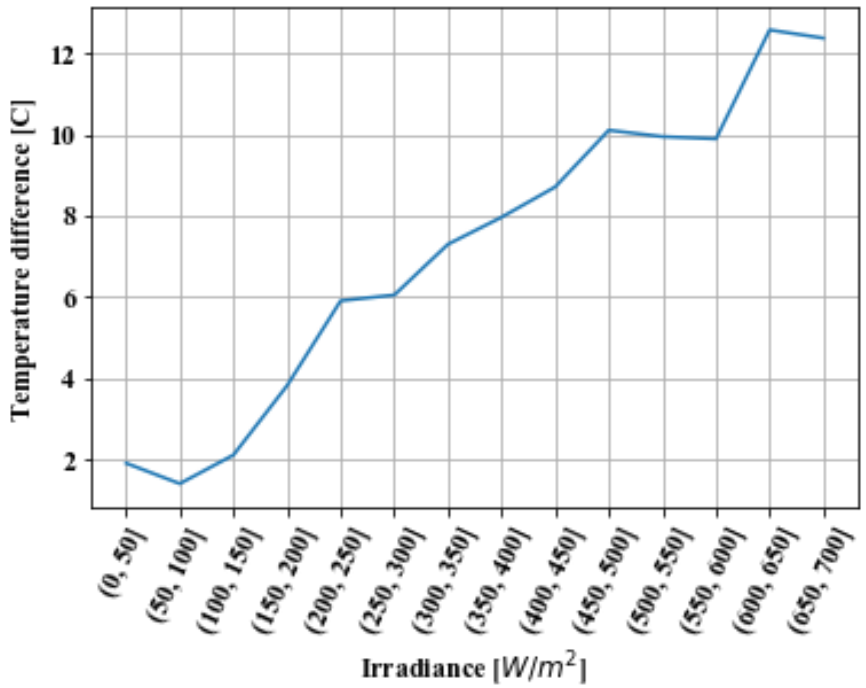

Figure 55: Mean absolute temperature difference in 50 W/m2 intervals.

Figure 55 shows that there is a substantial increase in the difference in temperature between the modules with increasing irradiance. Using the correlation between temperature and performance from the datasheet of the modules, a temperature difference of 2.5 degrees should result in an efficiency difference of approximately 5.13 %.

IR-pictures were also taken, to image the effects of lifting the modules. The IR-pictures were taken with a Mavic Enterprise Dual FLIR Camera on Wednesday 17th April, under good conditions with total plant power production at approximately 4.6 kW.

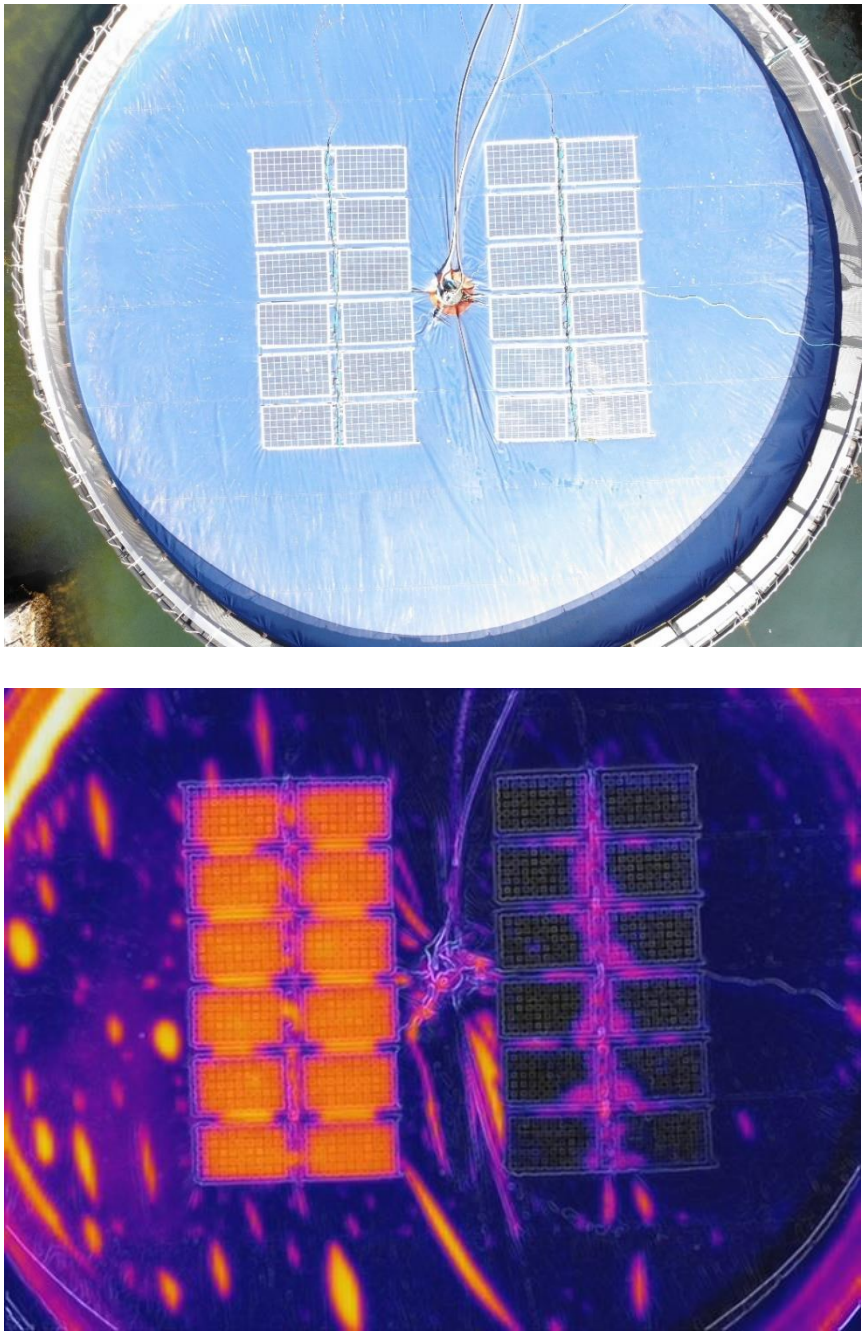

Figure 56: IR-picture of the system. The string with an air gap between the modules and the canvas is depicted to the left. The modules which are in contact with the canvas are to the right. The IR-picture does not include a temperature measurement and is meant to display the effect of thermal contact with water. The pictures are taken by representatives at Ocean Sun and displayed with permission.

Figure 56 graphically illustrates the temperature difference between the modules. It is possible to see hot spots where the cables and junction boxes are, but no other indications of faulty modules. The figure also illustrates how the water-cooled string largely adapts to the canvas/water temperature, while the air-cooled string takes a higher module temperature.

Other studies report an increase in efficiency on floating PV reports of a 2% to 14% increase depending on the type of technology that is used [43]. It is also reported that the observed temperature decreases are in the range of 3.5 $°C$ to 8 $°C$. Compared to Ocean sun's technology is it a larger decrease in temperature and a competitive increase in efficiency found in this thesis. Bear in mind that the data used in this thesis does not include irradiances close to STC and operation under high ambient temperatures. The results indicate a larger relative difference, especially at higher irradiance.

5.4 Models for simulating module temperatures

5.4.1 Simple fluid dynamic model for uniform temperature

The same type of model has previously been used on land-based PV-plants and showed promising results after few iterations [7]. To test the simple fluid dynamic model, it was used to model the module temperature for each day from 13.03.2019 to 18.04.2019.

The iterated values for module temperature were then compared against the measured back-surface module temperatures. The mean absolute error metric (MAE) is used to assess the model's validity, and standard deviation of the mean absolute error scores is presented as an indication of the reliability and robustness of the method. All simulations are done with a timestep of 100 and at different velocities for water. The results are presented in the table below.

Table 8: MAE from the simple temperature model with uniform temperature across the whole mass.

VELOCITY OF WATER $[m/s]$	**MAE $[°C]$**	**STANDARD DEVIATION OF MAE $[°C]$**
0	2.13	0.59
0.001	2.13	0.59
0.1	1.64	1.15
1	1.78	1.32
4	1.85	1.39
6	1.85	1.39
8	1.85	1.39

The table above indicates that simulations with a velocity of 0.1 m/s provide the best approach to model the module temperature in the given period. The scores are, however, not very exact. There are a significant mean absolute error and a large standard deviation of these errors for most of the velocities. For 0 and 0.001 m/s, there is some consistency in terms of faulty estimations.

The velocity of the water will greatly impact the calculated module temperatures. This can be seen both in the table for consistent MAE and in Figure 57, where velocities above 0.1 m/s make the module temperature conform to the water temperature.

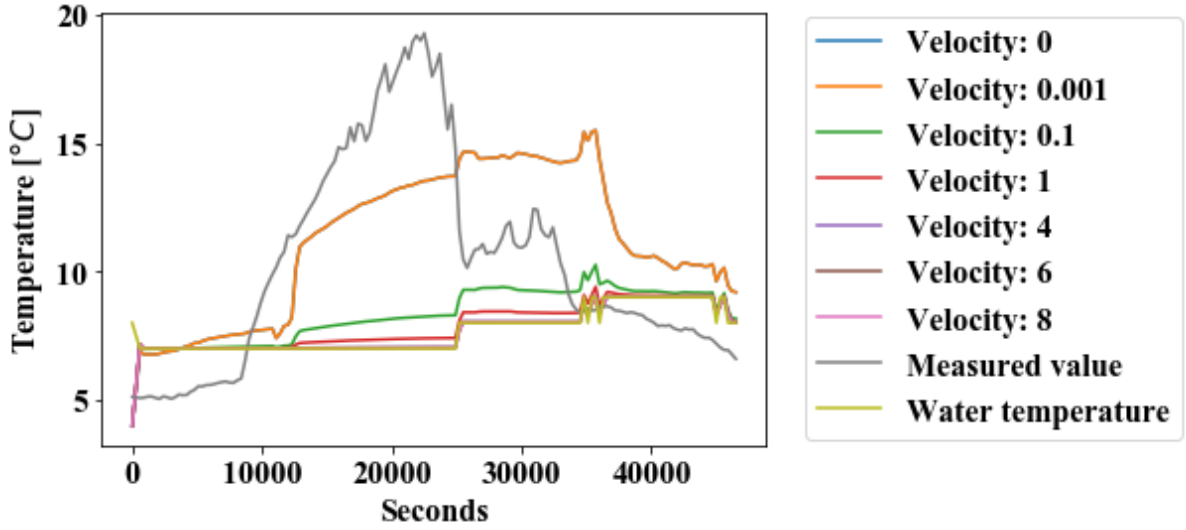

Figure 57: A simulation for different velocities of water for a random day. The yellowish line is water temperature. The lines labeled "Velocity: x " is the results for a simulation with that specific velocity of the water. The "Measured value" line is the true back-surface temperature.

It is evident that the model based on uniform temperature throughout the entire module is a too simple representation of reality. Naturally, the water will be the strongest driver for module temperature, which will give a large bias under conditions with high irradiance. It will, however, give a decent score for days when the irradiance is low. Whereas the model provided a decent estimation to module temperature for on-land systems, will it on floating PV-systems be too simple.

5.4.2 Simple fluid-dynamic model for layered geometry

From the simple fluid-dynamic model explained in 4.5.2 are simulations done for different air gaps, with different velocities for all the days used in the analysis. The timestep is 100 seconds. The results from the simulation are provided in the table below.

Table 9: Average MAE ± standard deviation for each simulation. The velocity is the velocity of the water, which dictates the convection coefficient.

VELOCITY $[m/s]$ \ **AIR GAP $[m]$**	**0**	**0.0001**	**0.001**	**0.01**
0	2.11 ± 065	2.45 ± 0.78	5.74 ± 2.16	17.87 ± 8.21
0.001	2.11 ± 0.65	2.45 ± 0.78	5.74 ± 2.16	17.87 ± 8.21
0.1	1.54 ± 0.91	1.61 ± 0.65	4.71 ± 1.68	17.70 ± 8.12
1	1.59 ± 1.05	1.56 ± 0.75	4.54 ± 1.61	17.67 ± 8.11
4	1.63 ± 1.12	1.54 ± 0.81	4.47 ± 1.58	17.66 ± 8.10
6	$1.63 + 1.12$	1.54 ± 0.81	4.47 ± 1.57	17.66 ± 8.10
8	1.63 ± 1.12	1.54 ± 0.81	4.47 ± 1.57	17.66 ± 8.10

The model will perform better with a low air gap and at higher velocities for water, with respect to actual measures of back-surface module temperature. This means to reduce the total heat resistance in the lower part of the module, and at the same time increase, the cooling effect from the water makes a better representation of reality. The most stable simulations are done for a velocity of 1 m/s at an air gap of 1 mm, whereas the most accurate representation is at no air gap with a velocity of 0.1 m/s. Higher air gaps than 1 mm will increase the thermal resistance in the module too much and result in high mean absolute errors.

When the system is modulated as a geometry with different layers, the sensitivity to the velocity of the water will be reduced. This is evident in the figures below, where simulations are done for two different air gaps and different velocities.

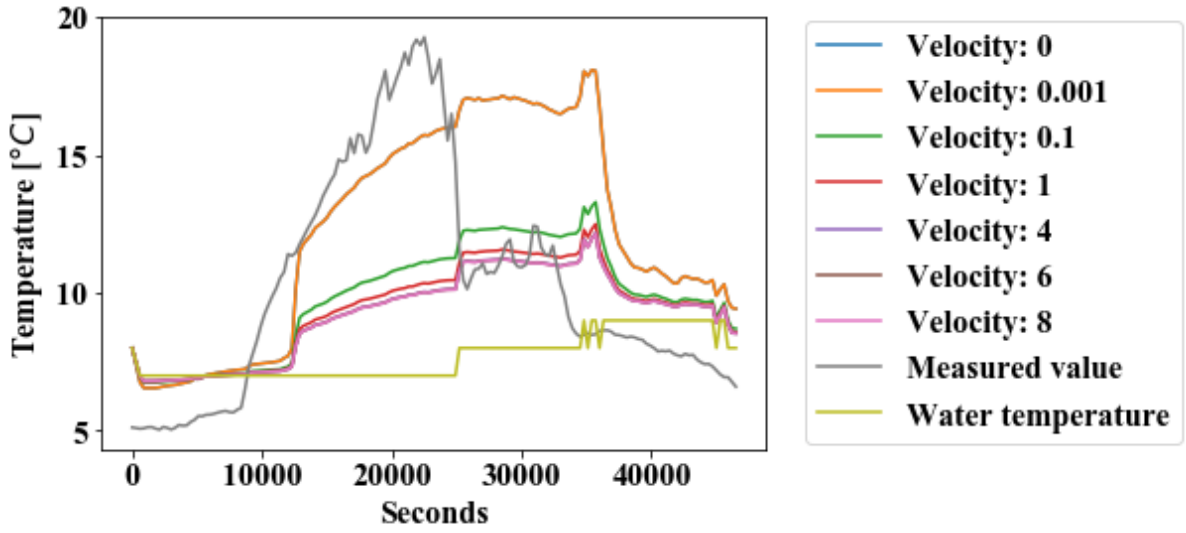

Figure 58: The figure displays the module temperature throughout a day for different simulations of water velocity. All these simulations are done with an air gap of 0.1 mm.

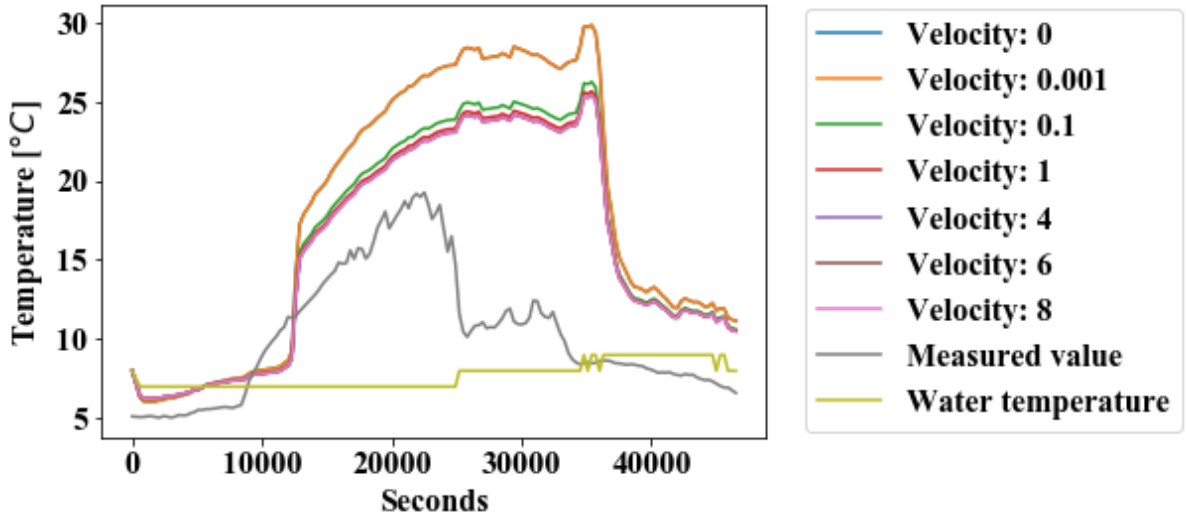

Figure 59: Simulations for module temperature with different velocities of water. All simulations are done with an air gap of 1 mm.

Compared to the model based on a single mass with uniform temperature will this model give a more accurate representation of reality. When the air gap increases will the model overshoot in its calculation of the module temperature. This is because of the reduced influence of the water temperature.

5.4.3 Regression model

While trying to accurately predict the module temperature at increasing irradiation and temperatures multiple regression models were tested. Ridge regression retains good score,

while at the same time offer transparency when it comes to key drivers in the model. The results from the regression model are provided in the table below.

Table 10: Average mean absolute errors from the ridge regression with standard deviation.

STRING	**AVERAGE MAE** [℃]	**STANDARD DEVIATION OF MAE [**℃]
STRING 1 – WATER COOLED	1.30	0.81
STRING 2 – AIR COOLED	3.04	1.96

The regression model outperforms both simple fluid-dynamic models while attaining a low deviation in faults. This indicates that the model will robustly estimate the module temperature without large differences in error. This gives the model more reliability and trustworthiness. T

As expected is the irradiance an important feature in module temperature. The coefficient indicates that a 4.21 percent increase in irradiation results in a 1.00 percent increase in module temperature. The slope for water temperature is larger for string 1 than string 2, and the opposite for air temperature. This is to be expected. The wind speed will have the greatest impact on the air-cooled string, string 2.

Table 11: Coefficient from the regression. These are created using scaled data.

STRINGS	**IRRADIANCE**	**WATER TEMPERATURE**	**AIR TEMPERATURE**	**WIND SPEED**
STRING 1 – WATER COOLED	1.83	1.91	0.086	-0.37
STRING 2 – AIR COOLED	5.22	2.57	0.795	-1.13

The results from the trained regression model are used to extrapolate values for module back-surface temperature under conditions with higher temperatures and irradiance. This is done

by specifying values for all the explanatory variables. Seven different cases are run. The values used in each case is loosely based on values for average temperatures and irradiation in Singapore [43]. The values are provided in Table 12:

Table 12: Values used for extrapolating the results for cases with higher ambient temperatures and higher irradiance.

CASE	IRRADIANCE	WATER TEMPERATURE	AIR TEMPERATURE	WIND SPEED
1	1000	25	26	2
2	1000	26	27	2
3	1000	27	28	2
4	1000	28	29	2
5	1000	29	30	2
6	1000	30	31	2
7	1000	31	32	2

The results for each case are provided below.

Table 13: Results for the regression run on the cases provided in table 11.

CASE	STRING 1 - TEMPERATURE	STRING 2 - TEMPERATURE
1	44.52	76.16
2	46.13	78.56
3	47.74	80.97
4	49.35	83.34
5	50.96	85.80
6	52.57	88.21
7	54.18	90.62

The temperatures predicted by the ridge regression model is very high for both strings. The results show a high difference in temperature for all cases, even though the temperature difference between water and air is low. The model does carry some bias because the model is used to predict a target variable on a sample range in which it has not been trained on. The

string temperature of the air-cooled string is abnormally high, which indicates that the generalizability of the model is poor.

5.4.4 Comparison of the models

Three random days were picked out to compare the results from the different models. The uniform temperature model in red is the model described in chapter 4.5.1 and the layered model in green is the model described in chapter 4.5.2. The irradiance for each day used in the simulations is provided in the table below. For the uniform temperature model was the velocity of the water 4 m/s. This corresponds with the models who offered a trade-off between low MAE and low standard deviation. For the layered model, the air gap was set to 0.1 mm and the velocity of the water to 0.1 m/s.

Table 14: Irradiance for specific days used in the simulation of the back-surface module temperature.

DATE	**IRRADIATION [kWh/m^2]**
19-03-2019	2.16
05-04-2019	3.10
14-04-2019	3.83

From the figures, it is evident that the models underestimate the temperature under high irradiance and does better at low irradiance.

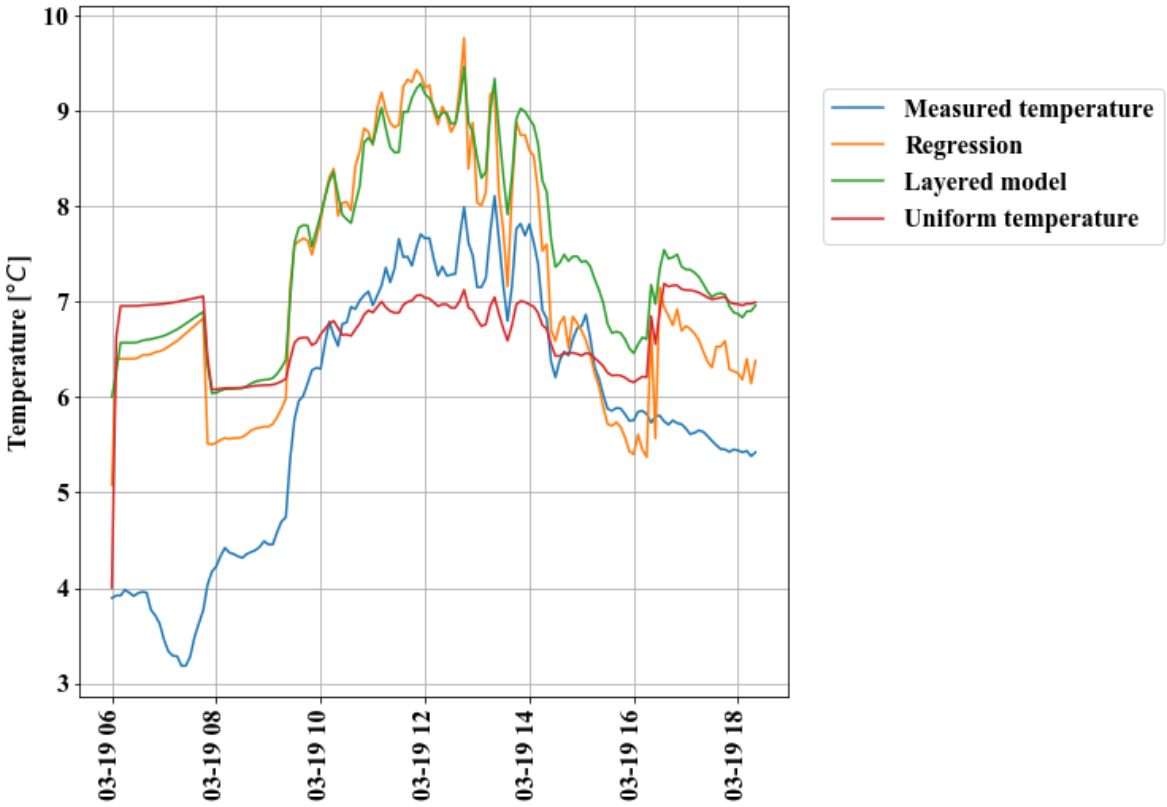

Figure 60: Results from the different models tested on a randomly chosen day. Here it's the 19. March.

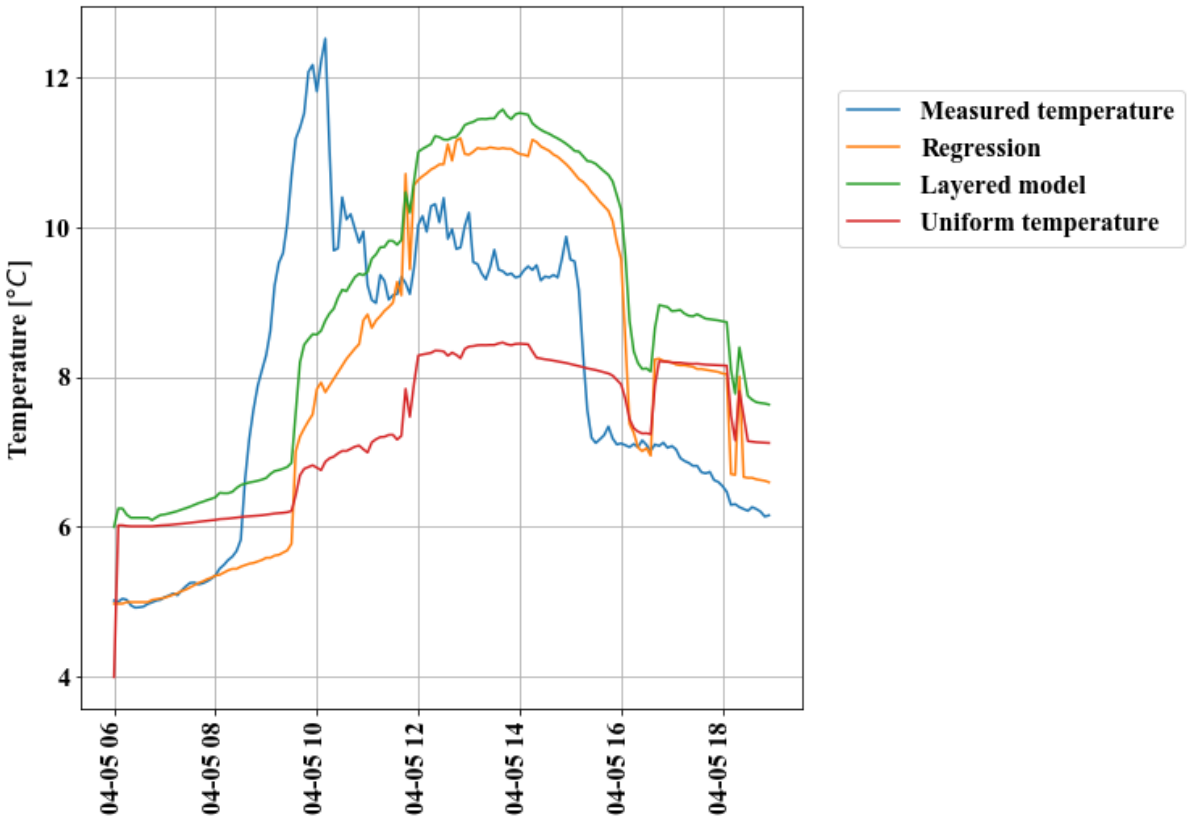

Figure 61: Results from simulations on 05. April.

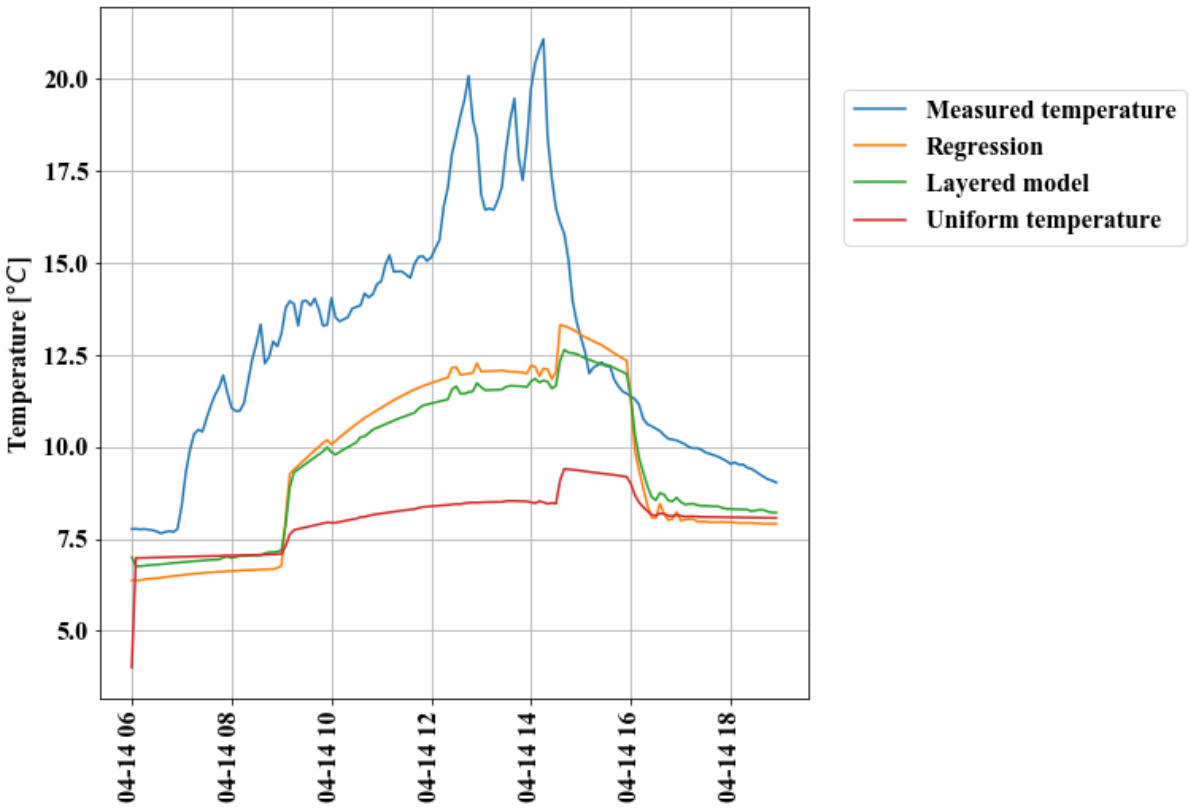

Figure 62: Results from simulations on the 14. April.

The results from the different models make it clear that the fluid-dynamic models are too simple to fathom the complex reality completely. They fail to adapt robustly to abrupt changes in irradiance which follow a partly clouded sky. They are also very sensitive to specific features, like the water flow. The main problem of the fluid-dynamic models is that they are steady-state models, with time-dependent thermic boundary conditions. This means that when the temperature changes at the boundaries it will change instantaneously in the whole module. The thermal lag which a transient model include is not preserved in these models.

To be able to accurately modulate the module temperature, a finite difference element approach should be tested. This will probably yield more accurate results in modulating the module temperature and investigate the difference in the air gap between the canvas and the module.

The ridge regression model suffers from low generalizability. It is probable that the model would perform better if more data were available. The model performs decently on data in which it has been trained on but is biased in predicting module temperatures outside of the provided interval of irradiance and temperatures. This is evident when the model was used to predict module temperatures for the two strings in a different climate.

5.5 Comparison between a tilted and floating horizontal system

The data used to calculate the in-plane irradiance is from 13.03.2019-18.04.2019. In Figure 63 the irradiance on a plane of array (POA) is depicted as averages throughout the day. It illustrates that all angles of tilt will give a higher irradiance than zero degrees.

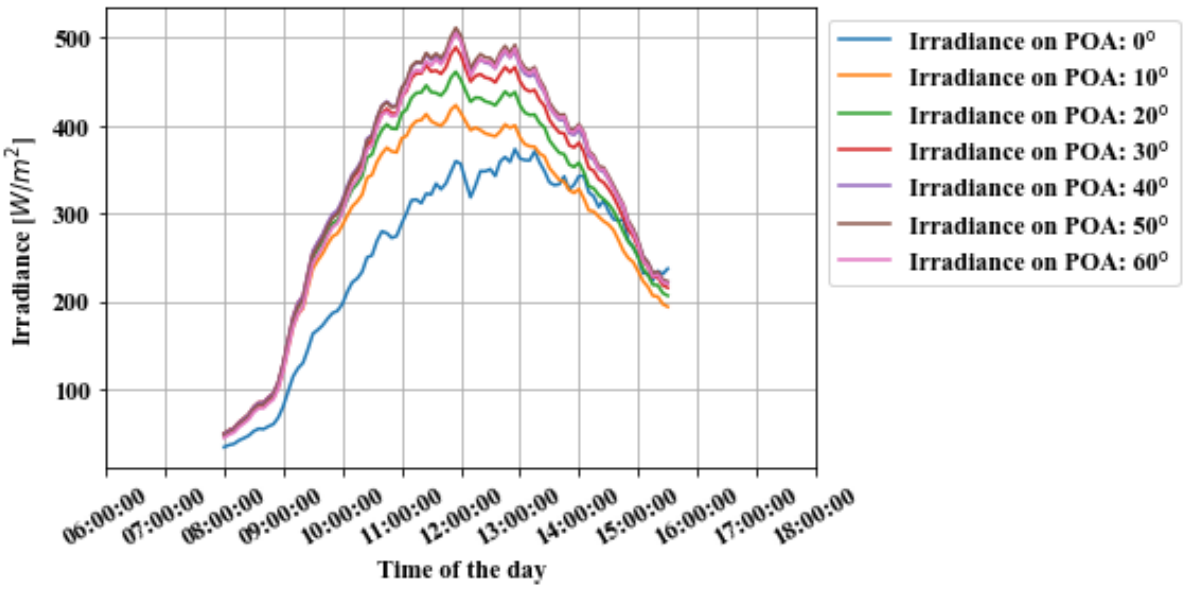

Figure 63: Average irradiance for each tilted case. The values are averaging every fifth minute taken from every day in the data.

Figure 63 depicts the 'break-even' efficiencies for different tilt profiles under intervals of global horizontal irradiance. When the demanded efficiency of the tilted string becomes more than the floating PV (zero tilt) efficiency, the tilt profile performs worse than a floating PV-system. This is true for both ten-, twenty- and thirty-degrees tilt. It is necessary to keep in mind that the analysis is done in a period of the year and a location that favors larger tilts. The validity of the Erbs and isotropic model for correct estimates of the POA irradiance must also be considered. Some findings show that the isotropic model gives a low POA irradiance compared to other models [52].

The values can also not be assumed to be true for irradiations above those experienced during the timeframe at Skaftå. Floating PV-systems will presumably have a larger advantage under conditions with high irradiance and high temperatures, as suggested by findings in the previous chapters. This can create an environment where the differences in the efficiencies between a horizontal floating PV-system and tilted system are larger, and the 'break-even' efficiency is harder to reach if not out of a realistic range.

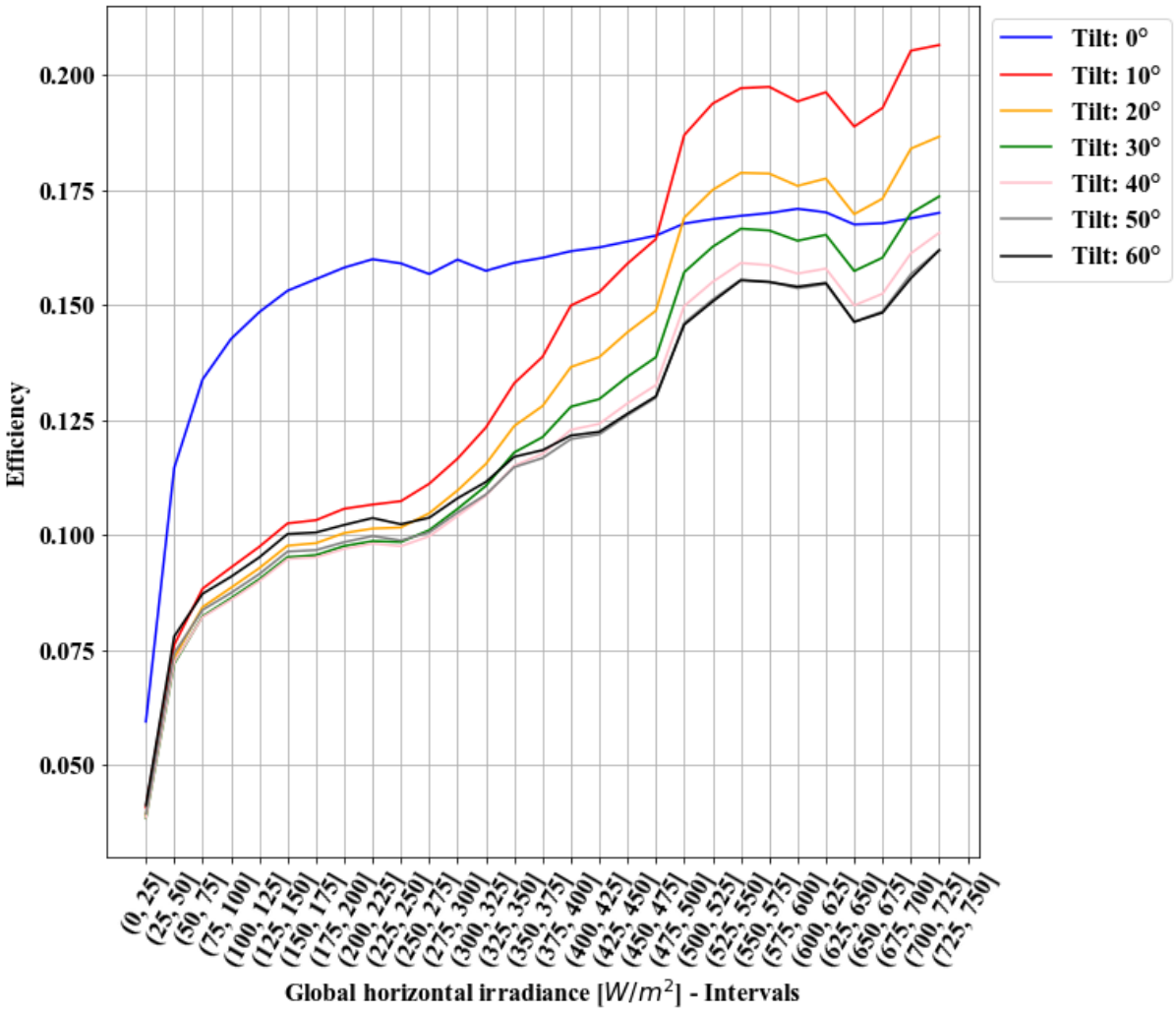

Figure 64: Efficiencies plotted against average irradiance of 25 W/m2 intervals. The efficiency for the tilted modules is set so that they give the same output as the FPV-system.

The results from Figure 64 indicate that for lower irradiance could tilted systems outperform the floating PV system. This is however not true when the irradiance increase. The tilted system must operate at efficiencies above 15% to be able to outperform the floating PV, and it seems that it will need to operate at efficiencies above the floating PV efficiency at even higher irradiance.

Conclusions

In the period of 01.06.2018 to 31.12.2018 is the system found to have a peak PR at 86 % in June, when analyzed on irradiance measured in Bergen. The results are believed to be somewhat uncertain due to the uncertainty of local weather conditions for Bergen and Skaftå. The analysis in this time frame also indicates that there is a small difference in the panels before the modules on one of the strings are lifted, but the uncertainties involved in the measurements renders it challenging to make a definitive statement.

There is also observed a substantial difference between the strings when one of the strings is lifted using 32 mm PP-pipes, and the other is kept in thermal contact with the canvas. There is a difference of 5.24% between the strings, calculated by efficiency and accumulated energy. The relative difference between the strings is found to increase with increasing irradiance. Extrapolated results from linear regression indicate that the difference could be about 6.6% at 1000 W/m^2. When data points logged at irradiance under 200 W/m^2 are removed, the difference increase with 4.47% to 5.48%.

There is observed a difference in temperature with higher irradiance. Evaluation of mean temperature difference at different irradiance intervals gives a back-surface module temperature difference of up to 12.5 degrees with irradiance between 600 and 650 W/m^2.

The steady-state models with time-dependent thermal boundary layers are too simple to completely fathom the reality. They assume an immediate change in temperature of the cell when the boundary condition changes. This is a simplification of the reality which will have a thermal lag. The ridge regression model used provided a somewhat more precise and robust model, but still below a satisfactory and trustworthy level based on the data at hand. To be able to mimic the cell temperature more complex transient models should be tried.

Lastly, the floating PV system was evaluated against different tilts under the same conditions as Skaftå provides. The analysis was only done for 35 days, which favored tilt for lower irradiance. At higher irradiance (675-750 W/m^2) will subsequently only $50°$ and $60°$ tilts perform better than floating PV, and the systems then need to operate at efficiencies close to 16%. The floating PV system is expected to perform better, relatively, compared to an air-cooled system irradiance close to STC. As a result, it is expected that tilted systems will have to increase their performance to above realistic levels to compete with floating PV.

Further work

- Expand the analysis with a longer period. It is of especially high interest to analyze the system under higher irradiance and higher temperatures, both water, and air.

- Create transient models using the finite difference method to model the cell temperature and to estimate the effect of different width on the air gap. This could be made in 2-D to assess local air gaps and not uniform air gaps. The figures for convection presented in 4.5.2.1 can be used to assess the convection coefficients.

- Compare a floating PV system against tilted systems and explore the difference at different locations and different times of the year.

- Evaluate the degradation of the floating PV system, corrosion from water and soiling from salt.

- Evaluate the hybridization possibilities with hydropower.

- Evaluate the costs of floating PV compared to land-based systems.

References

1. Cengel, Y.A. and A.J. Ghajar, *Heat and Mass Transfer*. fifth edition ed. 2015: McGraw-Hill Education.
2. International Energy Agency, *Global Energy & CO2 Status Report*. 2019.
3. REN21, *Renewable's 2018 Global Status Report*. 2018. p. 90-100.
4. Kumar, N.M., J. Kanchikere, and P. Mallikarjun, *Floatovoltaics: Towards Improed Energy Efficiency, Land and Water Management.* International Journal of Civil Engineering and Technology, 2018. **9**(7): p. 7.
5. Sahu, A., N. Yadav, and K. Sudhakar, *Floating photvoltaic power plant: A review.* Renewable and Sustainable Energy Reviews, 2016: p. 815-8124.
6. John Twidell & Tony Weir, *Renewable Energy Resources*. 2 ed. 2006: Taylor and Francis.
7. Smets, A., et al., *Solar Energy: The physics and engineering of photovoltaic conversion, technologies and systems*. 1 ed. 2016.
8. Smets, A., et al., *Solar Energy: The physics and Engineering of Photovoltaic Conversion Technologies And Systems*

2016: UIT Cambridge Ltd.

9. Smets, A., et al., *Solar Energy: The physics and Engineering of Photovoltaic Conversion Technologies And Systems*. 2016: UIT Cambridge Ltd.
10. Bowden, C.H.S. [cited 2019 29.01.2019]; PVeducation.org]. Available from: https://pveducation.org/pvcdrom/solar-cell-operation/the-photovoltaic-effect 24.01.2019.
11. Honsberg, C. and S. Bowden. *Double Diode Model*. 13.05.2019]; Available from: https://www.pveducation.org/pvcdrom/characterisation/double-diode-model.
12. Honsberg, C. and S. Bowden. *Solar Radiation on a Tilted Surface*. 22.04.2019]; Available from: https://www.pveducation.org/pvcdrom/properties-of-sunlight/solar-radiation-on-a-tilted-surface.
13. Loutzenhiser, P.G., et al., *Empirical validation of models to compute solar irradiance on inclined surfaces for building energy simulation.* 2006.
14. Holmgren, W.F., C.W. Hansen, and M.A. Mikofski, *pvlib python: a package for modeling solar energy systems* The Journal of Open Source Software, 2018.
15. Holmgren, W.F., C.W. Hansen, and M.A. Mikofski, *pvlib python: a package for modeling solar energy systems.* The Journal of Open Source Software, 2018.
16. Sandia National Laboratories. 05.05.2019]; Available from: https://pvpmc.sandia.gov/modeling-steps/1-weather-design-inputs/plane-of-array-poa-irradiance/calculating-poa-irradiance/angle-of-incidence/.
17. Honsberg, C. and S. Bowden. *Effect of temperature*. 2019 [cited 2019 22.02]; Available from: https://pveducation.org/pvcdrom/solar-cell-operation/effect-of-temperature.
18. Amelia, A.R., et al., *Investigation of the Effect Temperature on Photovoltaic (PV) Panel Output Performance.* International Journal on Advanced Science, Engineering and Information Technologi. **6**(5): p. 682-687.
19. Skoplaki, E. and J.A. Palyvos, *On the temperature dependence of photovoltaic module electrical performance: A review of efficiency/power correlations.* . Solar Energy 2009. **83**(5): p. 10.

20. King, D.L., W.E. Boyson, and J.A. Kratochvill, *Photovoltaic Array Performance model*. 2004, Sandia National Laboratories.
21. Vollmer, M. and K.P. Möllmann, *Infrared Thermal Imaging: Fundamentals, Research and Applicatons*. 2010: Wiley-VCH.
22. *Performance ratio: Quality factor for the PV plant*. 11.05.2019, SMA Solar Tecnology AG.
23. DOE OFFICE OF INDIAN ENERGY. 03.04.2019]; Available from: https://www.energy.gov/sites/prod/files/2015/08/f25/LCOE.pdf.
24. Afework, B., et al. *Levelized cost of energy*. 2018 11.05.2019]; Available from: https://energyeducation.ca/encyclopedia/Levelized_cost_of_energy.
25. World Bank Group, ESMAP, and SERIS, *Where Sun Meets Water: Floating Solar Market Report*. 2018.
26. Liu, L., et al., *Power Generation Efficiency and Prospects of Floating Photovoltaic Systems*, in *The 8th International Conference on Applied Energy*. 2017, Elsevier Ltd.
27. Majid, Z.A.A., et al., *Study on Performance of 80 Watt Floating Photovoltaic Panel.* ResearchGate, 2014.
28. Nandong, J. and M.S.A. Bakar, *Technoeconomic Analysis of Floating Solar Field for 1 GWh of Electricity Generation*. 2018.
29. sun, O. 20.04.2019]; Available from: https://oceansun.no/products/.
30. Google Maps. *Google Maps*. 07.05.2019]; Available from: https://www.google.com/maps/place/Skaft%C3%A5,+5285+Bruvik/@60.4565849,5.6189629,17z/data=!3m1!4b1!4m5!3m4!1s0x463c54a9e7137371:0xce5131ec8c46850f!8m2!3d60.4565849!4d5.6211516.
31. Fronius International GmBH. Available from: https://www.fronius.com/en/photovoltaics/products/all-products/inverters/fronius-primo/fronius-primo-6-0-1.
32. Norwegian Meteorological Institute Weather and Climate Database.
33. Fronius, I.G. *Fronius Sensor Box*. 10.05.2019]; Available from: https://www.fronius.com/en/photovoltaics/products/home/system-monitoring/hardware/fronius-sensor-card-box/fronius-sensor-box.
34. Fronius. *Ambient temperature sensor*. 01.05.2019]; Available from: https://www.fronius.com/en/photovoltaics/products/home/system-monitoring/hardware/sensors/ambient-temperature-sensor.
35. Fronius International GmBH. *Irradiation sensor*. 10.05.2019]; Available from: https://www.fronius.com/en/photovoltaics/products/all-products/system-monitoring/hardware/sensors/irradiation-sensor.
36. Fronius International GMBH. 10.05.2019]; Technical data for Fronius Wind speed sensor]. Available from: https://www.fronius.com/en/photovoltaics/products/home/system-monitoring/hardware/sensors/wind-sensor.
37. Fuentes, M.K., *A Simplified Thermal Model for Flat-Plate Photovoltaic Arrays*. 1987, Sandia National Laboratories.
38. Johnsen, G.H., T.T. Furset, and B. Tveranger, *Sørfjorden og Veafjorden: En hydromorfologisk beskrivelse*. 2017, Rådgivende Biologer AS.
39. H.Sharqawy, M., et al., *Thermophysical properties of seawater: A review of existing correlations and data.* Desalination and Water Treatment. **16**: p. 354-380.
40. Nayar, K.G., M.H. Sharqawy, and J.H.L. V. 2016.
41. K.G. Nayar, et al., *Thermophysical properties of seawater: A review and new correlations that include pressure dependence.* Desalination and Water Treatment. **16**: p. 354-380.

42. Incropera, F.P., et al., *Fundamentals of Heat and Mass Transfer*. 6th ed. 2007.
43. Lereng, I.H., *Study on the Cooling Effect for Floating PV Modules in Thermal Contact with Water and the Potential for Modelling Floating PV*. 2018, Norwegian University of Life Sciences.
44. Kamuyu, W.C.L., et al., *Prediction Model of Photovoltaic Module Temperature for Power Performance of Floating PV*. 2018.
45. Lay, D.C., S.R. Lay, and J.J. McDonald, *Linear Algebra and its Applications*. Fifth edition ed. 2016: Pearson Education Limited.
46. Hastie, T., R. Tibshirani, and J. Friedman, *The Elements of Statistical Learning: Data Mining, Inference, and Prediction*. Second ed.: Springer.
47. Raschka, S. and V. Mirjalili, *Python Machine Learning*. Second ed. 2017, Packt Publishing.
48. Pedregosa, F., et al. *GridseachCV*. 11.05.2019]; Available from: https://scikit-learn.org/stable/modules/generated/sklearn.model_selection.GridSearchCV.html.
49. Pedregosa, F., et al., *Scikit-learn: Machine Learning in Python* Journal of Machine Learning Research, 2011. **12**: p. 2825-2830.
50. Reich, N.H., et al., *Performance ratio revisited: is PR > 90% realistic?*, in *EU PVSEC*. 2011: Hamburg, Germany.
51. Dierauf, T., et al., *Weather-Corrected Performance Ratio*. National Renewable Energy Laboratory.
52. Lave, M., et al., *Evaluation of Global Horizontal Irradiance to Plane of Array Irradiance Models at Locations across the United States*. 2014.

6 Appendix

Appendix A – Data Sheets

Appendix B – Tables

Mono Multi Solutions

DUOMAX MODULE

TSM-PEG5.40

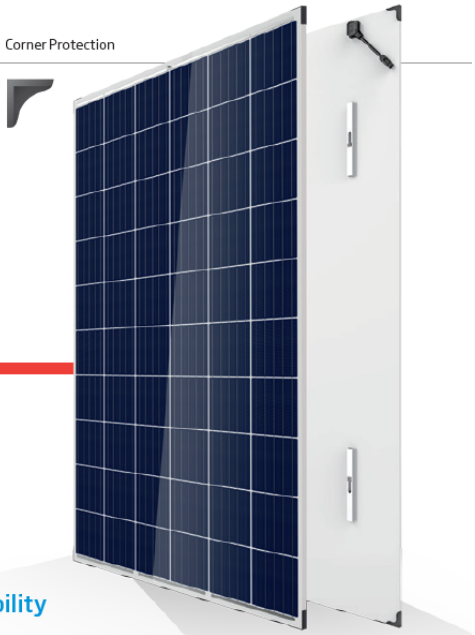

60 CELL
MULTICRYSTALLINE MODULE

270-285W
POWER OUTPUT RANGE

17.3%
MAXIMUM EFFICIENCY

0/+5W
POSITIVE POWER TOLERANCE

Founded in 1997, Trina Solar is the world's leading comprehensive solutions provider for solar energy. We believe close cooperation with our partners is critical to success. Trina Solar now distributes its PV products to over 60 countries all over the world. Trina Solar is able to provide exceptional service to each customer in each market and supplement our innovative, reliable products with the backing of Trina Solar as a strong, bankable partner. We are committed to building strategic, mutually beneficial collaboration with installers, developers, distributors and other partners.

Comprehensive Product And System Certificates

IEC61215/IEC61730/UL1703/IEC61701/IEC62716
ISO 9001: Quality Management System
ISO 14001: Environmental Management System
ISO14064: Greenhouse Gas Emissions Verification
OHSAS18001: Occupational Health and Safety Management System

Trinasolar

Improved durability
- Anti PID
- Reduced soiling due to natural cleaning
- Increased module robustness to minimize micro-cracks

Enhanced safety
- Fire class A certified by TUV Rheinland according to fire test IEC 61730-2 / MST 23
- Certified for fire type 13 (UL 1703)

Increased value
- 1,500 V system voltage reduces BOS costs by increased string length
- 30 year linear warranty
- 0.5% annual degradation

Highly reliable due to stringent quality control
- Over 30 in-house tests (UV, TC, HF, and many more)
- In-house testing goes well beyond certification requirements
- All modules have to pass electroluminescence (EL) inspection
- PID resistant
- 1000 V UL/1500 V IEC certified

Certified to withstand challenging environmental conditions
- Module coating resistant to sand, acid, and alkali
- 2400 Pa wind load
- 5400 Pa snow load
- 35 mm hail stones at 97 km/h

Trina Solar's DUOMAX Linear Performance Warranty

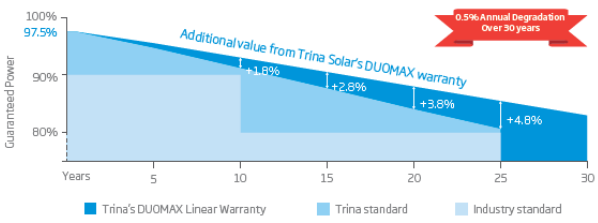

DUOMAX

TSM-PEG5.40

DIMENSIONS OF PV MODULE
TSM-PEG5.40
(unit: mm)

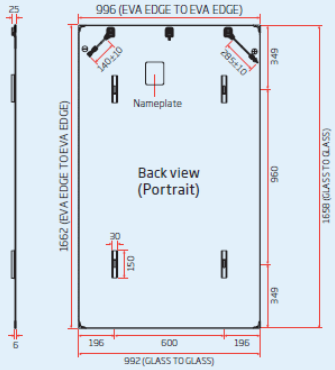

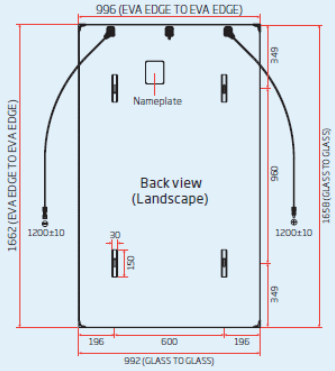

I-V CURVES OF PV MODULE (280W)

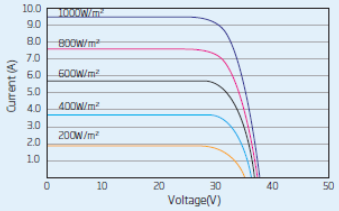

P-V CURVES OF PV MODULE (280W)

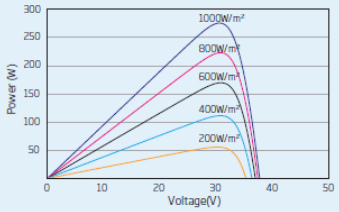

ELECTRICAL DATA @ STC	TSM-270	TSM-275	TSM-280	TSM-285
Peak Power Watts-P_{MAX} (Wp)*	270	275	280	285
Power Output Tolerance-P_{MAX} (W)	0/+5	0/+5	0/+5	0/+5
Maximum Power Voltage-V_{MPP} (V)	31.1	31.3	31.6	32.0
Maximum Power Current-I_{MPP} (A)	8.69	8.78	8.87	8.91
Open Circuit Voltage-V_{OC} (V)	38.0	38.2	38.4	38.6
Short Circuit Current-I_{SC} (A)	9.28	9.31	9.32	9.36
Module Efficiency η_m (%)	16.4	16.7	17.0	17.3

STC: Irradiance 1000 W/m², Cell Temperature 25 °C, Air Mass AM1.5
* Measuring tolerance: ±3%

ELECTRICAL DATA @ NOCT	TSM-270	TSM-275	TSM-280	TSM-285
Maximum Power-P_{MAX} (Wp)	200	204	208	211
Maximum Power Voltage-U_{MPP} (V)	28.8	29.0	29.2	29.6
Maximum Power Current-I_{MPP} (A)	6.97	7.04	7.11	7.14
Open Circuit Voltage-U_{OC} (V)	35.2	35.4	35.6	35.8
Short Circuit Current-I_{SC} (A)	7.49	7.52	7.52	7.56

NOCT: Irradiance at 800 W/m², Ambient Temperature 20 °C, Wind Speed 1 m/s.

MECHANICAL DATA

Solar Cells	Multicrystalline 156.75 × 156.75 mm
Cell Orientation	60 cells (6 x 10)
Module Dimensions	1658 × 992 × 6 mm 1662 × 996 × 6 mm with edge banding 1664 × 998 × 7.6 mm with corner protector (Std)*
Weight	23.0 kg
Front Glass	2.5 mm, high transparency, AR coated and heat strengthened glass
EVA	White
Back Glass	2.5 mm, heat strengthened glass
Frame	Frameless
J-Box	IP 67 rated or IP 68 rated
Cables	Photovoltaic Technology Cable 4.0 mm² Portrait: 140/285 mm, Landscape: 1200/1200 mm
Connector	MC4 EVO2/UTX/TS4

* Do not combine with slide-in solutions.

TEMPERATURE RATINGS

Nominal Operating Cell Temperature (NOCT)	44°C (±2K)
Temperature Coefficient of P_{MAX}	- 0.41%/K
Temperature Coefficient of V_{OC}	- 0.32%/K
Temperature Coefficient of I_{SC}	0.05%/K

WARRANTY

10 year Product Workmanship Warranty
30 year Linear Performance Warranty

(Please refer to product warranty for details)

PACKAGING CONFIGURATION

Modules per box:	33 pieces
Modules per 40' container:	858 pieces

MAXIMUM RATINGS

Operational Temperature	-40 to +85°C
Maximum System Voltage	1500 V DC (IEC) 1000 V DC (UL)
Max Series Fuse Rating**	15 A
Mechanical Load*	5400 Pa
Wind Load*	2400 Pa

* Max. mechanical loading values depend on the mounting method applied and only clamps approved by Trina Solar should be used.
** DO NOT connect fuse in combiner box with two or more strings in parallel connection.

MORE OPTIONS

Compact AR (Antireflective) coating
POE (Polyolefin Elastomer) foil
2.0 mm Glass: 19.7 kg

TSM_EN_2017_B

Trinasolar

CAUTION: READ SAFETY AND INSTALLATION INSTRUCTIONS BEFORE USING THE PRODUCT.

www.trinasolar.com

Fronius inverter

/ Perfect Welding / Solar Energy / Perfect Charging

FRONIUS PRIMO

The communicative inverter for optimised energy management.

SnapINverter Technology | Integrated data communication | SuperFlex Design | Dynamic Peak Manager | Smart Grid Ready | Zero feed-in

The Fronius Primo in power categories from 3.0 to 8.2 kW perfectly completes the SnapINverter generation. This single-phase, transformerless device is the ideal inverter for private households.

Its innovative SuperFlex Design provides maximum flexibility in system design, while the SnapINverter mounting system makes installation and maintenance easier than ever before. The communication package included as standard, with WLAN, energy management, several interfaces and much more besides, makes the Fronius Primo a communicative inverter for owner-occupiers.

TECHNICAL DATA FRONIUS PRIMO (3.0-1, 3.5-1, 3.6-1, 4.0-1, 4.6-1)

INPUT DATA	PRIMO 3.0-1	PRIMO 3.5-1	PRIMO 3.6-1	PRIMO 4.0-1	PRIMO 4.6-1
Number of MPP trackers	2				
Max. input current ($I_{dc\ max\ 1}$ / $I_{dc\ max\ 2}$)	12.0 A / 12.0 A				
Max. array short circuit current (MPP_1/MPP_2)	18.0 A / 18.0 A				
DC input voltage range ($U_{dc\ min}$ - $U_{dc\ max}$)	80 - 1000 V				
Feed-in start voltage ($U_{dc\ start}$)	80 V				
Usable MPP voltage range	80 - 800 V				
Number of DC connections	2 + 2				
Max. PV generator output ($P_{dc\ max}$)	4.5 kW_{peak}	5.3 kW_{peak}	5.5 kW_{peak}	6.0 kW_{peak}	6.9 kW_{peak}

OUTPUT DATA	PRIMO 3.0-1	PRIMO 3.5-1	PRIMO 3.6-1	PRIMO 4.0-1	PRIMO 4.6-1
AC nominal output ($P_{ac,r}$)	3,000 W	3,500 W	3,680 W	4,000 W	4,600 W
Max. output power	3,000 VA	3,500 VA	3,680 VA	4,000 VA	4,600 VA
AC output current ($I_{ac\ nom}$)	13.0 A	15.2 A	16.0 A	17.4 A	20.0 A
Grid connection (voltage range)	1 ~ NPE 220 V / 230 V (180 V - 270 V)				
Frequency (frequency range)	50 Hz / 60 Hz (45 - 65 Hz)				
Total harmonic distortion	< 5 %				
Power factor ($\cos \varphi_{ac,r}$)	0.85 - 1 ind. / cap.				

TECHNICAL DATA FRONIUS PRIMO (5.0-1, 5.0-1 AUS, 6.0-1, 8.2-1)

INPUT DATA	PRIMO 5.0-1	PRIMO 5.0-1 AUS	PRIMO 6.0-1	PRIMO 8.2-1
Number of MPP trackers	2			
Max. input current ($I_{dc\ max\ 1}$ / $I_{dc\ max\ 2}$)	12.0 A / 12.0 A	18.0 A / 18.0 A		
Max. array short circuit current (MPP_1/MPP_2)	18.0 A / 18.0 A	27.0 A / 27.0 A		
DC input voltage range ($U_{dc\ min}$ - $U_{dc\ max}$)	80 - 1,000 V			
Feed-in start voltage ($U_{dc\ start}$)	80 V			
Usable MPP voltage range	80 - 800 V			
Number of DC connections	2 + 2			
Max. PV generator output ($P_{dc\ max}$)	7.5 kW_{peak}	7.5 kW_{peak}	9.0 kW_{peak}	12.3 kW_{peak}

OUTPUT DATA	PRIMO 5.0-1	PRIMO 5.0-1 AUS	PRIMO 6.0-1	PRIMO 8.2-1
AC nominal output ($P_{ac,r}$)	5,000 W	4,600 W	6,000 W	8,200 W
Max. output power	5,000 VA	5,000 VA	6,000 VA	8,200 VA
AC output current ($I_{ac\ nom}$)	21.7 A	21.7 A	26.1 A	35.7 A
Grid connection (voltage range)	1 ~ NPE 220 V / 230 V (180 V - 270 V)			
Frequency (frequency range)	50 Hz / 60 Hz (45 - 65 Hz)			
Total harmonic distortion	< 5 %			
Power factor ($\cos \varphi_{ac,r}$)	0.85 - 1 ind. / cap.			

GENERAL DATA	PRIMO 5.0-1	PRIMO 5.0-1 AUS	PRIMO 6.0-1	PRIMO 8.2-1
Dimensions (height x width x depth)	645 x 431 x 204 mm			
Weight	21.5 kg			
Degree of protection	IP 65			
Protection class	1			
Overvoltage category (DC / AC) [1]	2 / 3			
Night time consumption	< 1 W			
Inverter design	Transformerless			
Cooling	Regulated air cooling			
Installation	Indoor and outdoor installation			
Ambient temperature range	-40 - +55 °C			
Permitted humidity	0 - 100 %			
Max. altitude	4,000 m			
DC connection technology	4x DC+ and 4x DC- screw terminals 2.5 - 16 mm^2			
AC connection technology	3-pole AC screw terminals 2.5 - 16 mm^2			
Certificates and compliance with standards	DIN V VDE 0126-1-1/A1, IEC 62109-1/-2, IEC 62116, IEC 61727, AS 4777-2, AS 4777-3, G83/2, G59/3, CEI 0-21, VDE AR N 4105 [2]			

[1] According to IEC 62109-1.
[2] Fronius Primo 5.0-1, Fronius Primo 6.0-1 and Fronius Primo 8.2-1 are not fully compliant with VDE AR N 4105.
Further information regarding the availability of the inverters in your country can be found at www.fronius.com.

EFFICIENCY	PRIMO 5.0-1	PRIMO 5.0-1 AUS	PRIMO 6.0-1	PRIMO 8.2-1
Max. efficiency	98.1 %	98.1 %	98.1 %	98.1 %
European efficiency (ηEU)	97.1 %	97.1 %	97.3 %	97.5 %
MPP adaptation efficiency	> 99.9 %			

PROTECTIVE DEVICES	PRIMO 5.0-1	PRIMO 5.0-1 AUS	PRIMO 6.0-1	PRIMO 8.2-1
DC insulation measurement	Yes			
Overload behaviour	Operating point shift. power limitation			
DC disconnector	Yes			
Reverse polarity protection	Yes			

INTERFACES	PRIMO 5.0-1	PRIMO 5.0-1 AUS	PRIMO 6.0-1	PRIMO 8.2-1
WLAN / Ethernet LAN	Fronius Solar.web, Modbus TCP SunSpec, Fronius Solar API (JSON)			
6 inputs and 4 digital in/out	Interface to ripple control receiver			
USB (A socket) [1]	Datalogging, inverter update via USB flash drive			
2x RS422 (RJ45 socket) [1]	Fronius Solar Net			
Signalling output [1]	Energy management (potential-free relay output)			
Datalogger and Webserver	Included			
External input [1]	S0-Meter Interface / Input for overvoltage protection			
RS485	Modbus RTU SunSpec or meter connection			

[1] Also available in the light version.
Further information and technical data can be found at www.fronius.com.

Thermosense **Datasheet**

PSA/PSB RTD (Pt100/Pt1000) Silicone Patch Sensor

Self adhesive silicone patch Platinum Resistance Thermometer sensors, commonly used for pipe or surface measurement. Available in two different sizes, but can easily be trimmed if a smaller footprint is required.

Supplied as a 4-wire configuration with a 2 metre PFA insulated stranded extension cable. Custom lengths can be supplied to suit the application.

Operating range -30°C to +200°C. The standard sensor (PSA) has a silicone cable support; the compact sensor (PSB) has a PTFE heatshrink cable support.

PSA patch dimensions: 40mm (L) x 15mm (W) x 6mm max depth.
PSB patch dimensions: 31mm (L) x 13mm (W) x 4mm max depth.

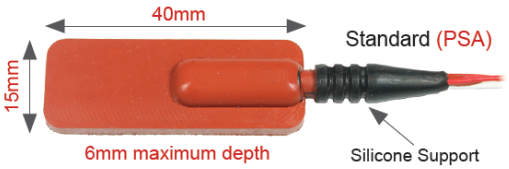

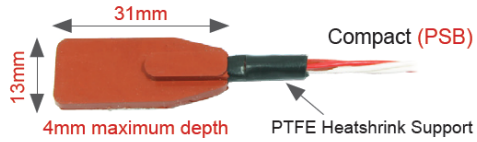

- Self adhesive
- Standard and compact versions available
- -30°C to +200°C operating range
- Commonly used for pipe or surface measurement

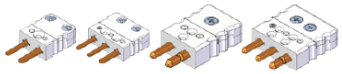
Optional connector (section 6)

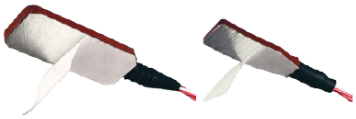
Self adhesive aluminium back plate

1	sensor type	code
	RTD (Pt100) Standard Silicone Patch Sensor	PSA
	RTD (Pt1000) Standard Silicone Patch Sensor	PSAK
	RTD (Pt100) Compact Silicone Patch Sensor	PSB
	RTD (Pt1000) Compact Silicone Patch Sensor	PSBK

2	wiring configuration	code
	2-wire	2
	3-wire	3
	4-wire (Simplex only)	4

3	grade of element	accuracy at 0°C	accuracy at 100°C	code
	B	± 0.30°C	± 0.80°C	B
	A	± 0.15°C	± 0.35°C	A

4	cable length (mm)	code
	As required to suit your application (standard length = 2000mm)	e.g. 2000

5	extension cable	code
	PFA Insulated, Twisted Cores, 7/0.2mm Ø conductors (+260°C), 2-wire	PT3220
	PFA Insulated, Twisted Cores, 7/0.2mm Ø conductors (+260°C), 3-wire	PT3320
	PFA Insulated, Twisted Cores, 7/0.2mm Ø conductors (+260°C), 4-wire	PT3420
	PFA Insulated, Twisted Cores, 7/0.2mm Ø conductors, PFA Sheathed (+260°C), 2-wire (page 52)	PT4220
	PFA Insulated, Twisted Cores, 7/0.2mm Ø conductors, PFA Sheathed (+260°C), 3-wire (page 52)	PT4320
	PFA Insulated, Twisted Cores, 7/0.2mm Ø conductors, PFA Sheathed (+260°C), 4-wire (page 52)	PT4420

See page 52 for our full range of RTD cable.

6	optional RTD connector (supplied attached to cable)	code
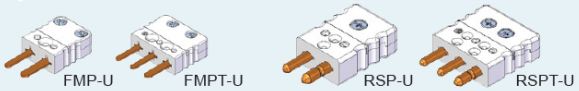 FMP-U FMPT-U RSP-U RSPT-U	Miniature RTD Plug	FMPU
	Miniature 3-Pin RTD Plug	FMPTU
	Standard RTD Plug	RSPU
	Standard 3-Pin RTD Plug	RSPTU

See pages 53-58 for our full range of RTD connectors.

Thermocouple version page 25

order code (example)	1	2	3	4	5	6
	PSA	- 2	- B	- 2000	- PT3220	- FMPU

QUADRTD – temperature logger

General Specifications

Description	QuadRTDTempV2	OctRTDTempV2
Temperature Sensor	External: 2, 3 or 4-wire 100 Ω platinum RTD	
Temperature Range	-200 °C to +850 °C (-328 °F to +1562 °F)	
Temperature Resolution	0.001 °C (0.0018 °F)	
Calibrated Accuracy	±0.04 °C (±0.072 °F)	
Memory (all 4 or 8 channels enabled)	87,296/channel	21,284/channel
Reading Rate	4 Hz up to 1 reading every 24 hours	
Channels	4	8
LED Indicator	**Primary LED (Green)** Blink (15 seconds) = Logging Blink (5 seconds) = Delay Start On key-press **Secondary LED (Red)** Blinks (5 Seconds) = Battery or Memory Low	
Specified Accuracy Range	-200 °C to +200 °C (-328 °F to 392 °F)	
Required Interface Package	IFC200	
Baud Rate	115,200	
Battery Type	9V lithium or alkaline battery included, **user replaceable**	
Typical Battery Life	1 year	
Operating Environment	-20 °C to +60 °C (-4 °F to +140 °F), 0 %RH to 95 %RH (non–condensing)	
Material	Anodized aluminum	
Weight	15 oz (420 g)	17 oz (490 g)
Dimensions	2.7 in x 7.2 in x 1.0 in (69 mm x 184 mm x 26 mm)	2.7 in x 7.2 in x 1.3 in (69 mm x 184 mm x 32 mm)

TRI-KA: IV-measurements

CONTROL AND MEASURING INSTRUMENTS Characteristics Analyser

Art. No.	0802201

Model	TRI-KA complete set
Included in delivery	1 TRI-KA, 1 TRI-SEN, 1 rugged case with rubber foam padding, TRI-KA measurement cable sets (MC3, MC4, Huber+Suhner, Tyco, SunClix and without connectors), 1 TRI-SEN mounting, 1 SD card (PC user software with user guide), 1 USB SD/SDHC card reader, 2 power supply units (chargeable), operating instructions

Specifications

Model	TRI-KA	TRI-SEN
Measuring	I/U characteristic curve, short-circuit current, open-circuit voltage, MPP current, MPP voltage	Global irradiation, module temperature, angle of inclination
Calculated values	STC values (short-circuit current, open-circuit voltage, MPP current, MPP voltage), fill factor, MPP output, ideal characteristic curve of module manufacturer	-
Voltage measuring range	1.0 - 1000 V (< ±1 %) (Uoc > 5 V)	-
Current measuring range	0.1 - 15.0 A (< ±1 %)	-
Temperature measuring range	-	0 - 100 °C (±3 % in relation to a black body)
Irradiation measuring range	-	100 - 1200 W/m² (±5 %)
Measuring connection	Measuring cable	Non-contact measurement
Characteristic curve measuring duration	15 - 30 seconds	-
Save slots for measured curves	Depending on size of SD memory card (> 1000 measured curves with 1 GB)	-
Reference cells	-	1 x monocrystalline cell, 1 x polycrystalline cell
Display	3.2 inch colour LCD touch screen (240 x 320 pixels, RGB)	B/W LC display (2-line, 16 characters)
Power supply	Lithium polymer accumulator, run-time app. 8 hours	Lithium polymer accumulator, run-time app. 8 hours
Auto power-off	Adjustable (1 - 15 minutes)	-
Interface	2 measuring cables to PV string, wireless connection to TRI-SEN, SD/SDHC memory card for PC	Wireless connection to TRI-KA
Ambient temperature	0 to +50 °C	0 to +60 °C
Protection mode	IP20	IP20
Insulation	Protection class II	-
Measuring category	CAT II 1000 V, CAT III 600 V	-
Dimensions (L / W / H)	210 mm / 105 mm / 41 mm	160 mm / 82 mm / 41 mm
Weight	500 g	200 g
Warranty	2 years	2 years
Norms	EN 61010-1, EN 61010-2-030, EN 61010-031, CE mark	EN 61010-1, CE mark

Spare parts

Art. No.	Model	Belongs to Art. No.
0801101	TRI-KA measurement cable replacement set for MC3	0802201
0801102	TRI-KA measurement cable replacement set for MC4	0802201
0801103	TRI-KA measurement cable replacement set for Huber+Suhner	0802201
0801104	TRI-KA measurement cable replacement set for Tyco	0802201
0801110	TRI-KA measurement cable replacement set without connector	0802201
0802202	TRI-SEN mounting	0802201
0802203	TRI-KA measurement cable replacement set for SunClix	0802201
0802205	TRI-KA SD/SDHC card reader	0802201
0802206	TRI-KA SD/SDHC memory card	0802201
0802208	TRI-KA rugged case, empty	0802201
0802209	TRI-KA chargeable power supply unit	0802201

For measurements of (certain) thin-layer modules and special module technologies, please consult TRITEC.

System requirements user software: Microsoft® Windows XP / Vista / 7; Pentium processor with a minimum of 600 MHz or similar; minimum of 256 MB memory or more; VGA graphics card with at least 16 bit colour depth (High Color) and a resolution of 1024 x 768 pixels; free hard disc memory of at least 500 MB; keyboard; mouse; USB interface

B - Tables

Properties of air [1]

TABLE A–15

Properties of air at 1 atm pressure

Temp. T, °C	Density ρ, kg/m^3	Specific Heat c_p, J/kg·K	Thermal Conductivity k, W/m·K	Thermal Diffusivity α, m^2/s	Dynamic Viscosity μ, kg/m·s	Kinematic Viscosity ν, m^2/s	Prandtl Number Pr
−150	2.866	983	0.01171	4.158×10^{-6}	8.636×10^{-6}	3.013×10^{-6}	0.7246
−100	2.038	966	0.01582	8.036×10^{-6}	1.189×10^{-5}	5.837×10^{-6}	0.7263
−50	1.582	999	0.01979	1.252×10^{-5}	1.474×10^{-5}	9.319×10^{-6}	0.7440
−40	1.514	1002	0.02057	1.356×10^{-5}	1.527×10^{-5}	1.008×10^{-5}	0.7436
−30	1.451	1004	0.02134	1.465×10^{-5}	1.579×10^{-5}	1.087×10^{-5}	0.7425
−20	1.394	1005	0.02211	1.578×10^{-5}	1.630×10^{-5}	1.169×10^{-5}	0.7408
−10	1.341	1006	0.02288	1.696×10^{-5}	1.680×10^{-5}	1.252×10^{-5}	0.7387
0	1.292	1006	0.02364	1.818×10^{-5}	1.729×10^{-5}	1.338×10^{-5}	0.7362
5	1.269	1006	0.02401	1.880×10^{-5}	1.754×10^{-5}	1.382×10^{-5}	0.7350
10	1.246	1006	0.02439	1.944×10^{-5}	1.778×10^{-5}	1.426×10^{-5}	0.7336
15	1.225	1007	0.02476	2.009×10^{-5}	1.802×10^{-5}	1.470×10^{-5}	0.7323
20	1.204	1007	0.02514	2.074×10^{-5}	1.825×10^{-5}	1.516×10^{-5}	0.7309
25	1.184	1007	0.02551	2.141×10^{-5}	1.849×10^{-5}	1.562×10^{-5}	0.7296
30	1.164	1007	0.02588	2.208×10^{-5}	1.872×10^{-5}	1.608×10^{-5}	0.7282
35	1.145	1007	0.02625	2.277×10^{-5}	1.895×10^{-5}	1.655×10^{-5}	0.7268
40	1.127	1007	0.02662	2.346×10^{-5}	1.918×10^{-5}	1.702×10^{-5}	0.7255
45	1.109	1007	0.02699	2.416×10^{-5}	1.941×10^{-5}	1.750×10^{-5}	0.7241
50	1.092	1007	0.02735	2.487×10^{-5}	1.963×10^{-5}	1.798×10^{-5}	0.7228
60	1.059	1007	0.02808	2.632×10^{-5}	2.008×10^{-5}	1.896×10^{-5}	0.7202
70	1.028	1007	0.02881	2.780×10^{-5}	2.052×10^{-5}	1.995×10^{-5}	0.7177
80	0.9994	1008	0.02953	2.931×10^{-5}	2.096×10^{-5}	2.097×10^{-5}	0.7154
90	0.9718	1008	0.03024	3.086×10^{-5}	2.139×10^{-5}	2.201×10^{-5}	0.7132
100	0.9458	1009	0.03095	3.243×10^{-5}	2.181×10^{-5}	2.306×10^{-5}	0.7111
120	0.8977	1011	0.03235	3.565×10^{-5}	2.264×10^{-5}	2.522×10^{-5}	0.7073
140	0.8542	1013	0.03374	3.898×10^{-5}	2.345×10^{-5}	2.745×10^{-5}	0.7041
160	0.8148	1016	0.03511	4.241×10^{-5}	2.420×10^{-5}	2.975×10^{-5}	0.7014
180	0.7788	1019	0.03646	4.593×10^{-5}	2.504×10^{-5}	3.212×10^{-5}	0.6992
200	0.7459	1023	0.03779	4.954×10^{-5}	2.577×10^{-5}	3.455×10^{-5}	0.6974
250	0.6746	1033	0.04104	5.890×10^{-5}	2.760×10^{-5}	4.091×10^{-5}	0.6946
300	0.6158	1044	0.04418	6.871×10^{-5}	2.934×10^{-5}	4.765×10^{-5}	0.6935
350	0.5664	1056	0.04721	7.892×10^{-5}	3.101×10^{-5}	5.475×10^{-5}	0.6937
400	0.5243	1069	0.05015	8.951×10^{-5}	3.261×10^{-5}	6.219×10^{-5}	0.6948
450	0.4880	1081	0.05298	1.004×10^{-4}	3.415×10^{-5}	6.997×10^{-5}	0.6965
500	0.4565	1093	0.05572	1.117×10^{-4}	3.563×10^{-5}	7.806×10^{-5}	0.6986
600	0.4042	1115	0.06093	1.352×10^{-4}	3.846×10^{-5}	9.515×10^{-5}	0.7037
700	0.3627	1135	0.06581	1.598×10^{-4}	4.111×10^{-5}	1.133×10^{-4}	0.7092
800	0.3289	1153	0.07037	1.855×10^{-4}	4.362×10^{-5}	1.326×10^{-4}	0.7149
900	0.3008	1169	0.07465	2.122×10^{-4}	4.600×10^{-5}	1.529×10^{-4}	0.7206
1000	0.2772	1184	0.07868	2.398×10^{-4}	4.826×10^{-5}	1.741×10^{-4}	0.7260
1500	0.1990	1234	0.09599	3.908×10^{-4}	5.817×10^{-5}	2.922×10^{-4}	0.7478
2000	0.1553	1264	0.11113	5.664×10^{-4}	6.630×10^{-5}	4.270×10^{-4}	0.7539

Note: For ideal gases, the properties c_p, k, μ, and Pr are independent of pressure. The properties ρ, ν, and α at a pressure P (in atm) other than 1 atm are determined by multiplying the values of ρ at the given temperature by P and by dividing ν and α by P.

Source: Data generated from the EES software developed by S. A. Klein and F. L. Alvarado. Original sources: Keenan, Chao, Keyes, Gas Tables, Wiley, 1984; and Thermophysical Properties of Matter. Vol. 3: Thermal Conductivity, Y. S. Touloukian, P. E. Liley, S. C. Saxena, Vol. 11: Viscosity, Y. S. Touloukian, S. C. Saxena, and P. Hestermans, IFI/Plenun, NY, 1970, ISBN 0-306067020-8.

IV-measurements

05.02.2019

MEASUREMENTS	TIME	IRRADIANCE $[W/m^2]$	STRING	$P_{STC}[W]$
1	15:39	27	1	3134
2	15:41	27	1	3153
3	15:42	27	1	3070
4	15:45	26	2	3052
5	15:46	26	2	3005

26.02.2019

MEASUREMENT	TIME	IRRADIANCE $[W/m^2]$	MODULE TEMPERATURE [C]	STRING	P_{STC} $[W]$
1	13:07	238	6.9	1	3003
2	13:08	219	6.9	1	3294
3	13:10	176	6.9	1	3560
4	13:14	172	12.3	2	3237
5	13:15	180	12.3	2	3345
6	13:16	177	12.3	2	3319

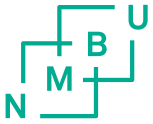

Norges miljø- og biovitenskapelige universitet
Noregs miljø- og biovitskapelege universitet
Norwegian University of Life Sciences

Postboks 5003
NO-1432 Ås
Norway